Partial product gas combustion for tar reduction

Partial product gas combustion for tar reduction

PROEFSCHRIFT

ter verkrijging van de graad van doctor aan de
Technische Universiteit Eindhoven, op gezag van de
Rector Magnificus, prof.dr.ir. C.J. van Duijn, voor een
commissie aangewezen door het College voor
Promoties in het openbaar te verdedigen
op maandag 22 januari 2007 om 16.00 uur

door

Theodoor Adriaan van der Hoeven

geboren te Eersel

Dit proefschrift is goedgekeurd door de promotoren:

prof.dr.ir. A.A. van Steenhoven
en
prof.dr. L.P.H. de Goey

Copromotor:
dr.ir. H.C. de Lange

This research was financially supported by SenterNovem.

Cover design by Jeroen Habraken.

Printed by the Eindhoven University Press.

A catalogue record is available from the Library Eindhoven University of Technology
ISBN-10: 90-386-2609-6
ISBN-13: 978-90-386-2609-3

To start is to finish!

Contents

Summary

Partial product gas combustion for tar reduction

To utilize the full potential of biomass gasification, tar reduction techniques have to be found. A relatively cheap tar reduction technique, especially suited for small-scale purposes, is after-treatment of product gas by partial combustion. Partial combustion of a tar containing synthetic gas mixture in a micro-scale swirl-burner, has previously been shown to reduce tar by either cracking or polymerization. Tar cracking showed to be stimulated by an increasing fuel hydrogen content and a decreasing oxidation level.

The goal of this thesis is two-fold. First, the tar reduction mechanisms, and in particular the influence of the fuel hydrogen content and the oxidation level on them, are to be understood in more detail. Second, the necessary preconditions for partial combustion of real product gas are to be determined.

To first goal is pursued by studying tar conversion mechanisms in literature and by chemical modeling. In literature it is found that both thermal and oxidative tar treatment can lead to tar conversion. Both conversion processes are initiated by free radicals. During thermal treatment a balance is found between tar conversion by cracking and polymerization, depending on a necessary hydrogen-shift from polymerization to cracking species. The balance can be directed towards cracking by the presence of ambient hydrogen or steam. During oxidative treatment, the oxidation level determines whether tar cracking or polymerization reactions prevail. Again, ambient hydrogen seems to lead to increased cracking reactions.

Based on the findings in literature, it is hypothesized that tar cracking by partial combustion happens by a two-step oxidation/conversion mechanism, in which free radicals formed in the oxidation reactions cause tar cracking during conversion reactions. To test the hypothesis, two computational models have been developed and used to study the chemical kinetics of free radicals and of aromatics during (partial) combustion of synthetic product gas. The first model is a two-step model with which the concentrations and residence times of free radicals during partial combustion are estimated as a function of the fuel hydrogen content and the oxidation level. It shows that increasing the fuel hydrogen content and the level of oxidation leads to higher free radical concentrations with increased residence times. This should

hypothetically lead to increased tar cracking. The second model is a one-step model with which the behaviour of aromatic species under oxidative environments is studied. The model indeed predicts a two-step chemical process with a clear oxidation regime and a clear conversion regime. During the oxidation regime, all product gas components (including tar) are converted into a wide variety of species next to a lot of small oxidation products. In the conversion regime, the variety of species created is converted into either cracking or polymerization products depending on the conditions. According to the model, tar cracking is increased by increasing the fuel hydrogen content and the level of oxidation.

Both literature as well as the chemical models show that an increasing fuel hydrogen content and an increasing level of oxidation should lead to increased tar cracking. The predicted influence of the fuel hydrogen content corresponds to that found in the tar conversion experiments. However, the predicted influence of the oxidation level does not correspond to the behaviour found in earlier experiments. This discrepancy is attributed to the air addition in the experimental swirl-burner, which creates local regions at a high level of oxidation while the average oxidation level is low.

In pursuing the second goal, a small-scale gasifier setup is constructed in which partial product gas combustion is to be tested. The gasifier setup consists of a 20 kW batch-operated updraft biomass gasifier to produce product gas, and a flare to combust all product gas leaving the partial combustive after-treatment. Both the gasifier and the flare are operated by newly designed automated control systems.

Before partial combustion is tested in an upscale swirl-burner in the gasifier setup, the micro-scale swirl-burner is tested for its working area. It shows that the micro-scale swirl-burner can only be used for partial combustion at low fuel powers or very high fuel hydrogen contents. Performing the same test in the upscale swirl-burner shows that the working area is a scalable property, since it is again restricted to low fuel powers. Therefore, partial combustion of real product gas in the gasifier setup has been tested at low fuel power. However, at low fuel powers the gasifier produces product gas with a very low quality (especially regarding the hydrogen content), due to which the partial combustion process could not be ignited. It is concluded that the present burner design is not suited for stable partial combustion.

Therefore, a new partial combustion burner is designed based on the two-step oxidation/conversion principle. Experiments on a micro-scale version of the new burner design, show that the burner has a significantly improved working area with respect to the fuel power. However, the partial combustion stability at low fuel hydrogen content is still limited, probably due to the flow velocities exceeding the maximum fuel combustion velocities. Therefore, an up-scaled partial combustion burner is constructed in which the flow velocities are lower than in the micro-scale version. The working area and tar reduction capabilities of the up-scaled partial combustion burner are still to be tested.

Samenvatting

Partiële product-gas verbranding voor teer-reductie

Om het potentieel van biomassa vergassing ten volle te benutten zullen er teer-reductie technieken moeten worden ontwikkeld. Een relatief goedkope teer-reductie techniek, speciaal geschikt voor toepassingen op kleine schaal, is nabehandeling van product-gas door middel van partiële verbranding. Partiële verbranding van een teer-houdend synthetisch product-gas in een kleine swirl-brander, heeft eerder aangetoond tot teer-reductie te leiden door middel van kraken danwel polymerisatie. Teer-kraken bleek te worden gestimuleerd door een stijgende waterstof concentratie in het gas en door een dalende oxidatie-graad.

Het doel van dit proefschrift is tweevoudig. Allereerst het beter begrijpen van de teer-reductie mechanismen in gang gezet door partiële verbranding, en de invloed van de waterstof concentratie en de oxidatie-graad op deze mechanismen. Verder, het vaststellen van de operationele voorwaarden nodig voor partiële verbranding van een echt product-gas.

Het eerste doel is nagestreefd door het bestuderen van teer-conversie mechanismen in literatuur, en door middel van chemische modellering. Uit de literatuur komt naar voren dat zowel thermische als oxidatieve teer-behandelingen kunnen leiden tot teer-conversie. Beide conversie-processen worden geïnitieerd door vrije radicalen. Tijdens thermische behandeling ontstaat er een balans tussen kraak- en polymerisatie-reacties, als gevolg van waterstof overdracht van polymerisatie-producten naar kraak-producten. De balans wordt verschoven richting kraken door een stijgende waterstof- en stoom-concentratie. Tijdens de oxidatieve behandeling bepaalt de oxidatie-graad de balans tussen kraken en polymeriseren. Ook hier leiden hogere waterstof-concentraties tot meer kraak-reacties. Op basis hiervan is de hypothese gesteld dat teer-kraken tijdens partiële verbranding gebeurt door vrije radicalen gevormd tijdens oxidatie reacties.

Om de hypothese te toetsen zijn twee computer-modellen gebruikt om de chemische kinetiek van vrije radicalen en aromaten tijdens (partiële) verbranding van gas te bestuderen. Een twee-staps model geeft aan dat zowel een stijgende waterstof concentratie als een stijgende oxidatie-graad leiden tot meer vrije radicalen met

een hogere verblijftijd. Hypothetisch zou dit tot meer teer-kraken moeten leiden. Het een-staps model voorspelt een twee-staps chemisch proces met duidelijk een oxidatie-regime en een conversie-regime. Tijdens het oxidatie-regime worden alle product-gas componenten (ook teer) omgezet in een grote variteit aan componenten en een hoop verbrandingsproducten. In het conversie-regime volgen kraken of polymerisatie, afhankelijk van de condities. Ook dit model wijst uit dat teer-kraken gestimuleerd wordt door een stijgende waterstof-concentratie en oxidatie-graad.

Zowel literatuur als de modellen geven aan dat een stijgende waterstof-concentratie en oxidatie-graad tot meer teer-kraken moeten leiden. De voorspelde invloed van waterstof komt inderdaad overeen met resultaten uit eerdere experimenten. Echter, de voorspelde invloed van de oxidatie-graad komt niet overeen met experimenten. Deze discrepantie wordt toegewezen aan de lucht injectie in de eerdere experimenten. Hierdoor ontstaat een inhomogeniteit door vorming van locale zones met hoge oxidatie-graad, terwijl de gemiddelde oxidatie-graad relatief laag blijft.

Met het oog op het tweede doel is er een experimentele vergasser-opstelling geconstrueerd waarin partiële verbranding getest kan worden op echt product-gas. De opstelling bevat een 20 kW batch tegenstroom biomassa-vergasser om product-gas te produceren, en een installatie om het product-gas na partiële verbranding af te fakkelen. Zowel de vergasser als de fakkel worden bediend via een nieuw ontworpen geautomatiseerd controle-systeem.

Voordat partiële verbranding is getest in de vergasser-opstelling in een opgeschaalde swirl-brander, is de kleine swirl-brander getest op zijn werk-gebied. Dit blijkt beperkt tot lage vermogens, of hoge waterstof-concentraties van het synthetisch gas. Ook van de opgeschaalde swirl-brander is het werk-gebied op synthetisch gas beperkt tot lage vermogens, waardoor het werkgebied een schaalbare eigenschap lijkt. Echter, partiële verbranding van echt product-gas in de opgeschaalde swirl-brander kon niet worden ontstoken bij lage vermogens, omdat de vergasser bij lage vermogens gas produceert met een erg slechte kwaliteit (vooral gezien de waterstof-concentratie). Er wordt geconcludeerd dat het swirl-brander ontwerp niet geschikt is voor stabiele partiële verbranding.

Er is een nieuwe partiële verbrander ontworpen gebaseerd op het twee-staps chemische oxidatie/conversie proces. Experimenten tonen dat het werkgebied van partiële verbranding in een kleine 'nieuwe-stijl' verbrander aanzienlijk vergroot is richting hogere vermogens. De stabiliteit van het proces bij lage waterstof-gehaltes blijft echter slecht, wat waarschijnlijk een consequentie is van de gassnelheden die de maximale verbrandingssnelheden overschrijden. Daarom is er een opgeschaalde 'nieuwe-stijl' verbrander gemaakt waarin de stromings snelheden lager zijn dan de maximale verbrandingssnelheden. Het werkgebied en de teer-reductie-capaciteit van de nieuwe opgeschaalde brander moeten nog worden getest.

Nomenclature

Roman symbols

A	area	m^2
$\bar{c}_p$	average heat capacity at constant pressure	kJ kg^{-1} K^{-1}
CD	discharge coefficient	-
D	diameter	m
H_i	combustion enthalpy	kJ mol^{-1}
h	convection coefficient	W m^{-2} K^{-1}
K	loss factor	-
k	k-value	-
k	conduction coefficient	W m^{-1} K^{-1}
k_w	constant	-
L	length	m
L	flammability limit of complex mixture	vol.%
MF	gas composition	mol mol^{-1}
MR_{st}	Molar ratio of gas over air at stoichiometry	-
$\dot{m}$	mass conversion rate	kg s^{-1}
$\dot{m}$	mass flow rate	kg s^{-1}
N	flammability limit of dissected mixture	vol.%
n	number of holes	-
P	power	W
p	pressure	bar
p_+	maximum overpressure	Pa
R	radius	m
Re	Reynolds number	-
S_L	laminar burning velocity	m s^{-1}
T	temperature	K
t	wall thickness	m
U_f	flame front propagation velocity	m s^{-1}
U_{st}	local stoichiometric axial flow velocity	m s^{-1}
u	velocity	m s^{-1}
$\bar{u}$	average velocity	m s^{-1}

u_{ref}	reference velocity	m s^{-1}
$\dot{V}$	volume flow	m^3 s^{-1}
Y_{max}	maximum penetration	m

Greek symbols

α	proportionality factor	-
α	tilt angle	$\circ$
α	thermal expansion coefficient	μm K m^{-1}
θ	swirl angle	$\circ$
λ	air-excess ratio	-
μ	dynamic viscosity	Pa s
ρ	density	kg m^{-3}
$\bar{\rho}$	average density	kg m^{-3}
σ_θ	creep strength in longitudinal direction	MPa
τ	nominal residence time	s
Ω	heat loss resistance	K W^{-1}

Abbreviations

FHC	Fuel Hydrogen Content	vol.%
FI	Flow Indicator	
FSV	Fast Shut-off Valve	
FT	Flow Transmitter	
GC	Gas Chromatograph	
IGBT	Insulated Gate Bipolar Transistor	
IR	Infrared	
LHV	Lower Heating Value	MJ Nm^{-3}
MFC	Mass Flow Controller	
PI	Pressure Indicator	
PRV	Pressure Relief Valve	
PSR	Perfectly Stirred Reactor	
PT	Pressure Transmitter	
PV	Proportional Valve	
RCM	Rapid Compression Machine	
SPA	Solid Phase Adsorption	
TCD	Thermal Conductivity Detector	
TT	Temperature Transmitter	

Chapter 1

Introduction

1.1 Background

A promising renewable energy conversion technique is biomass gasification. Gasification is a thermochemical conversion technique, that is able to convert biomass into product gas containing gaseous species such as hydrogen, carbon monoxide, methane, carbon dioxide, water vapor and tar. Because gasification is a partial oxidation process (running at insufficient oxygen compared to stoichiometric combustion), most chemical energy contained by the biomass is maintained as chemical energy in the form of gaseous species. All rest energy is converted into heat. Since the heat loss is relatively minor compared to combustion, the gasification process is considered highly efficient.

The product gas produced by biomass gasification can be used for a variety of applications. It can for example be used as a ground material for the production of a large variety of chemical substances (among which alternative fuels), or it can be used as a chemical energy source for energy conversion processes in turbines or internal combustion engines. These applications can be used on a large scale, as well as on a small scale. Biomass gasification in small-scale energy systems can be especially attractive for self-supporting energy consumers.

Tar formation during the thermal decomposition (pyrolysis) of biomass as part of the biomass gasification process is not avoidable. Tar is formed due to the depolymerization of the building blocks of biomass: cellulose, hemicellulose and lignin. The primary tar produced during pyrolysis mainly consists of oxygenated species. These species are converted relatively quick into secondary and subsequently into very stable tertiary tar species under influence of temperature. Tertiary tar consists mainly of (poly) aromatic hydrocarbons [59].

Thus, the term 'tar' as used in this thesis, is a complex mixture of organics that is produced during thermochemical biomass conversion processes. The term 'tar' describes a lump involving thousands of single substances [59], due to which an unambiguous definition of tar cannot be given. A general definition of 'tar' often used is: all organic contaminants having a molecular weight higher than benzene [63]. In this thesis, benzene itself is also considered a tar component since it is a main building block of all tar components.

As the term 'soot' will be frequently used throughout the thesis, it is defined here as well. In general, 'soot' is a randomly formed particulate carbon material and may be coarse, fine and/or colloidal in proportions depending on its origin. 'Soot' consists of variable quantities of carbonaceous and inorganic solids together with absorbed and occluded tars and resins [56]. Throughout the thesis it is assumed that 'soot' is formed by aggregation of soot-precursors, which on their turn are formed by tar polymerization.

The inevitable tar production during biomass gasification is the largest drawback of the conversion technique. Tar forms a nasty byproduct that can condense at low temperatures, because of which it can easily cause fouling, plugging and breakdown of after-treatment or end-use equipment. The tar content of product gas has to be reduced considerably before biomass gasification can become economically viable.

Tar reduction can be achieved by either primary or secondary measures [18]. Primary measures are taken in the gasifier itself, and are used to prevent tar formation or to convert tar immediately after production. The main primary measures are: (i) proper selection of the operating conditions, (ii) use of a proper bed additive or catalyst during gasification, and (iii) a proper gasifier design [18]. Secondary measures are after-treatments on the product gas to reduce its tar content. Examples of secondary measures are: thermal treatment, catalytic treatment, chemical conversion by corona plasma discharge, partial oxidative treatment, and mechanical separation by filters or scrubbers. Among the primary and secondary measures there are several techniques that are capable of strongly reducing the tar content in product gas. However, most readily available tar reduction techniques are not cost-effective for small-scale installations.

A seemingly useful after-treatment technique for small-scale installations is ex-situ tar reduction by partial combustion. The technique offers a cheap, simple, waste-free, infinite lifetime solution that can be used on product gas produced by any gasifier design. During ex-situ partial combustion the raw product gas is partially combusted at a low air-excess ratio. Ex-situ partial combustion is an after-treatment technique for tar reduction that is based on tar cracking. Tar cracking has the advantage above other ways of tar reduction that no soot or waste is formed. The heating value of the tars is thus contained in the end product at the expense of the heating value of the combusted part of the product gas.

Tar removal by noncatalytic partial combustion of product gas has not been studied extensively before. There are only a few experimental studies in which gasifier concepts have been developed using partial product gas combustion. These concepts show that the tar-content of raw product gas can be influenced by carefully controlling the combustion zone [33,78]. The drawback of these studies is that they

are based on varying gasifier concepts. The tar reduction is not only a consequence of partial combustion, but also of the changed gasifier concept. Furthermore, they did not study the working principle of tar reduction by partial combustion in detail.

Recently, partial combustion of tar-containing synthetic product gas has been studied more systematically by Houben [39]. The influence of partial combustion on the tar concentration was shown by adding naphthalene to an artificial product gas, and combusting it in the micro-scale swirl-burner shown in figure 1.1. The oxidizing air is injected into the product gas through 7 tilted circumferential holes that each form a jet in cross-flow configuration. Each jet creates a small blue colored combustion zone, as shown in figure 1.2. Although Houben called the process 'partial oxidation', it is called 'partial combustion' throughout this thesis to indicate that flames are present.

Houben tested the naphthalene conversion as a function of the air-excess ratio and the fuel hydrogen content of a methane/hydrogen/nitrogen-mixture with fixed energy content. When not counting benzene as a tar-component, partial combustion could reduce the naphthalene up to 95 vol.%. Depending on the air-excess ratio and the product gas composition, the naphthalene was either cracked or polymerized. In figure 1.3 the tar conversion results are shown as a function of the air-excess ratio for a fuel hydrogen content of 22.5 vol.%. In figure 1.4 the tar conversion results are shown as a function of the fuel hydrogen content for an air-excess ratio of 0.2. On both horizontal axes the measured remaining tar components are grouped as a function of their aromaticity, e.g. benzene (C_6H_6) having low aromaticity and 5-ring aromatics having high aromaticity. The added naphthalene has a two-ring aromaticity, because of which cracking leads to benzene or 1-ring species, and polymerization leads to 3 or higher ring species. Cracking of naphthalene mainly occurred at $\lambda < 0.4$ and Fuel Hydrogen Content (FHC) > 20 vol.%. In measurements outside this domain polymerization reactions prevailed. Hence, it was shown that both the fuel hydrogen content and the air-excess ratio are of major influence on the cracking of naphthalene.

To study the cause of tar cracking by partial combustion, Houben conducted experiments on the tar conversion effects of pure thermal product gas treatment. Therefore, a real product gas was heat treated in an oven at several residence times and temperatures. The results showed that only polymerization of the present tar components took place. It was concluded that the tar cracking by partial combustion could therefore not be caused singly by its thermal effects. This indicates that next to the temperature rise, also the chemical reactions or the release of specific chemical species influence the tar conversion process. It was argued that tar conversion was caused by free radicals, whose amount got influenced by the air-excess ratio and the fuel hydrogen content.

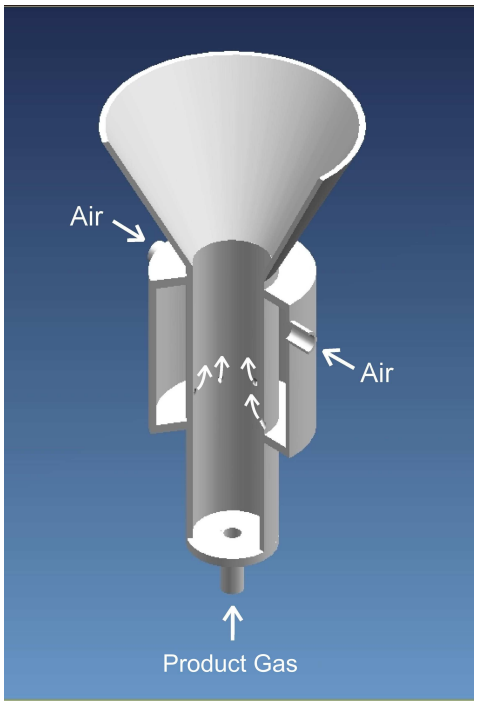

Figure 1.1 : Micro-scale swirl-burner as designed by Houben. Dimensions are similar to those shown in figure 5.2(b).

Figure 1.2 : Photograph of the 7 blue flames visible during the partial combustion process inside the micro-scale swirl-burner [39].

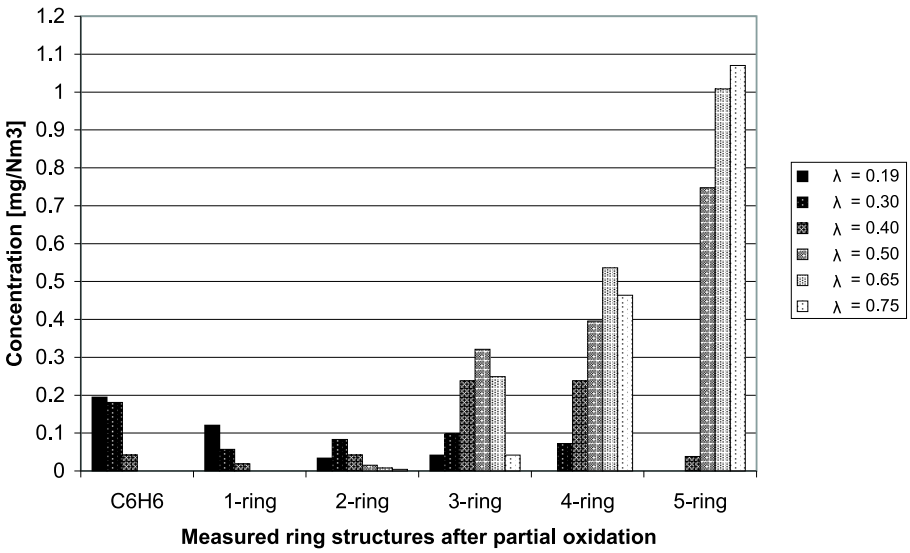

Figure 1.3 : Results of experimental tar reduction by partial combustion as a function of air-excess ratio; Inlet gas = 22.4 vol.% H_2, 5.0 vol.% CH_4 and 72.6 vol.% N_2; Inlet concentration $C_{10}H_8$ = 2.6 mg/Nm^3; Lower Heating Value = 4.2 MJ/Nm^3; Power = 2,8 kW; Inlet temperature = 200°C. Adapted from [39].

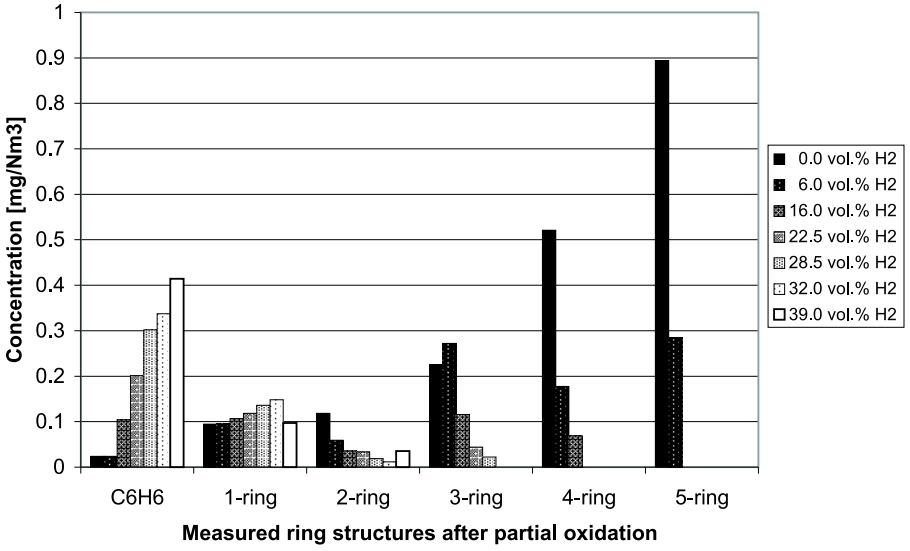

Figure 1.4 : Results of experimental tar reduction by partial combustion as a function of fuel hydrogen content; Inlet gas: a variable composition of H_2, CH_4 and N_2; Inlet concentration $C_{10}H_8$ = 2.6 mg/Nm^3; Lower Heating Value = 4.2 MJ/Nm^3; Air-excess ratio = 0.2; Power = 2,8 kW; Inlet temperature = 200°C. Adapted from [39].

The results obtained by Houben seem very promising for the application of partial combustion for tar reduction in product gas. However, some points remain unclear. First, the partial combustion was tested on an artificial product gas, containing only methane, hydrogen, nitrogen and naphthalene. Although the results are probably indicative, it is not conclusive that partial combustion of real product gas would lead to similar results. Second, the naphthalene concentrations added in the described experiments were very low. It has not yet been shown what the influence of the tar concentration is on the tar reduction results. It is expected that the tar concentration could influence the outcomes of partial combustion, because of which partial combustion of real product gas could lead to different results. And third, the influence of thermal effects on the tar content of product gas was only tested at relatively low fuel hydrogen content, while tar cracking was only found at high fuel hydrogen content. Therefore, it is still possible that thermal treatment of tar containing product gas at high fuel hydrogen content would lead to tar cracking.

Further, the tar reduction process itself is not yet understood. It shows that hydrogen has a positive effect on tar reduction by cracking, while oxygen shows a negative effect. Apparently hydrogen has a beneficial effect on the chemical kinetics of the tar cracking paths. The effect of oxygen on the cracking paths is ambiguous; a lack of oxygen ($\lambda = 0$) supposedly leads to polymerization, a slight amount of oxygen ($\lambda = 0.2$) leads to tar cracking, while a larger amount oxygen ($0.3 < \lambda < 0.8$) again leads to polymerization [39]. If partial combustion is to become a successful tar reduction technique, more knowledge should be gained on the mechanism of tar reduction. Especially interesting are the influence of gas composition, tar concentration, level of oxidation, process temperature, and process layout on the partial combustion and its tar reduction.

1.2 Objectives

Optimization of tar reduction by partial combustion can be better achieved if there is a clear knowledge of the tar reduction mechanisms, and of the influence of the partial combustion process on these mechanisms. Therefore, the first goal of this research is to set a step towards understanding the tar conversion mechanisms as function of process parameters such as temperature, level of oxidation, and mixture settings. The knowledge gained can be used for improving the partial combustion process.

Tar reduction by partial combustion has been shown for a synthetic gas-mixture containing trace amounts of naphthalene. Before partial combustion can be used in small-scale or industrial applications, the process has to be tested on real product gas. The second goal of this research is to understand the necessary preconditions for partial combustion of a real product gas. To achieve this goal the partial combus-

tion stability limits are studied to determine which parameters play an important role in the working range of the process. Further, an experimental setup containing a biomass gasifier is designed and constructed to evaluate the partial combustion stability on a real product gas.

This thesis is a result of the project *"Integrated IN and EX-SITU removal of tar in small-scale biomass gasification"*, funded by Senternovem. The aim of the project was the development of a small-scale gasification plant for biomass utilizing combined in-bed (catalytic) additives and thermal after treatment to reduce the tar content of its product gas. The part discussed in this thesis is the ex-situ thermal after-treatment part, which is more specifically aimed at the development of the partial combustion after treatment technique.

1.3 Outline

This thesis discusses basically three topics: (1) the possible chemical mechanisms responsible for tar reduction, (2) the design and construction of a biomass gasification test-setup, and (3) the functioning of partial combustion on several fuels including real product gas.

Topic one is discussed in chapters 2 and 3. In chapter 2 possible conversion mechanisms for typical aromatics under thermal and oxidative treatment are studied. Based on this chapter, the production of free radicals during partial combustion is studied in chapter 3 using chemical simulations. Especially, the dependence of cracking and polymerization of naphthalene on the partial combustion conditions is studied.

Topic two is described in chapter 4. The chapter describes the design of a small-scale test-setup containing a biomass gasifier, and a flare. The test-setup is constructed for testing the effect of partial combustion on the tar content in real product gas.

Topic three is discussed in chapters 5 and 6. In chapter 5 first the working area of a micro-scale swirl-burner is determined as a function of some burner-geometry parameters. Subsequently, an up-scaled swirl-burner is constructed, whose functioning is tested in the gasifier test-setup. Based on the results of chapter 5, a re-designed micro-scale partial combustion burner is discussed and tested for its working area in chapter 6. This micro-scale partial combustion burner design is also scaled-up to fit the gasifier setup.

The thesis is finalized by conclusions drawn from the described chapters.

Chapter 2

Consideration of thermal and oxidative tar treatment

Since tar conversion by partial combustion is not yet fully understood, literature is used to study tar cracking and polymerization mechanisms. The behaviour of tars during pyrolysis, combustion and partial combustion is studied. In section 2.1 the mechanisms of pure thermal tar treatment are discussed for various aromatics. Also the influence of steam and some major gases on the tar conversion mechanism by thermal treatment are discussed. In section 2.2 oxidative tar treatment is studied, and the tar conversion mechanisms under oxidative circumstances are discussed. In section 2.3 tar conversion by partial combustion is discussed with respect to the knowledge gained on thermal and oxidative tar treatment.

2.1 Thermal tar treatment

Thermal treatment of tar means that tar is converted by heating it to high temperatures (mostly above 900°C) for a certain residence time. The high temperature influences the stability of tar, because of which it can convert into other species.

Thermal tar treatment has been experimentally studied by Jess [44], who discussed the cracking, polymerization and sooting behaviour of different aromatic[1] and aliphatic[2] species under varying circumstances. The treatment temperature, treatment time, species concentration, and the ambient gas concentrations were varied to find their influence on the species conversion.

Thermal tar conversion is also experimentally studied by Miura et al., and by Garcia and Hüttinger [28, 58]. Miura et al. investigated the possibility to convert tar vapor of hot coke oven gas to a synthesis gas while varying the treatment temperature, kind of tar species, gas residence time, and the ambient gas concentrations. Garcia and Hüttinger studied the pyrolysis and steam gasification of saturated naphthalene, 1-naphtol and indene in argon. In their study they varied the treatment temperature, the residence time, and the naphthalene-steam ratio.

[1] Aromatic species: In the traditional sense species having a chemistry typified by benzene [56].

[2] Aliphatic species: Acyclic or cyclic, saturated or unsaturated carbon species, excluding aromatic species [56].

In the following subsections the influence of various parameters, such as the treatment temperature, treatment time, tar species, species concentration, steam concentration, and the ambient gas concentrations are discussed based on the work by Jess, Miura et al., and Garcia and Hüttinger. The tar species considered in this chapter are benzene, naphthalene and alkylated[3]-benzenes.

2.1.1 Thermal tar conversion mechanisms

The results by Jess, Miura et al., and Garcia and Hüttinger show that during thermal tar treatment, part of the tar is converted and part is not converted. The tar conversion increases for both increasing treatment temperature and gas residence time, and for increasing initial tar concentration. According to Jess [44], the rate at which the tar conversion is related to the tar concentration depends on the kind of species considered.

Tar conversion leads to both organic cracking products as well as polymerization products. There shows to be a linear relation between the amount of tar converted and the amount of cracking and polymerization products produced, irrespective of the treatment temperature and the gas residence time.

In pure pyrolysis situations of tar in inert gas, the formation of organic cracking products will always be accompanied by formation of polymerization products. This is a consequence of the low atomic hydrogen content of tar, which prevents production of cracking products with relatively high atomic hydrogen content without production of hydrocarbons with a lower hydrogen content as the original tar. A consequence is that the maximum gas yield and the matching heavy tar yield, depend on the hydrogen content of the reacting tar. More hydrogen in the tar means that more hydrogen is released during formation of polymerization products. This consequently leads to a higher gas/heavy tar yield ratio. The hydrogen atom transfer-mechanism can be called *'hydrogen shift'*, and is schematically shown in figure 2.1.

The aromaticity of tar influences its reactivity because of the difference in decomposition energy [44]. For example, the relative thermal reactivity of the considered tar species is: alkylated-benzenes $>$ naphthalene $>$ benzene.

Tar cracking paths

In general, aromatics form organic cracking products by the addition of hydrogen and the subsequent breaking of the ring structures. Important cracking products formed during thermal tar treatment are methane, C2-hydrocarbons and benzene.

[3] Alkylated species: Species having one or more side-chains.

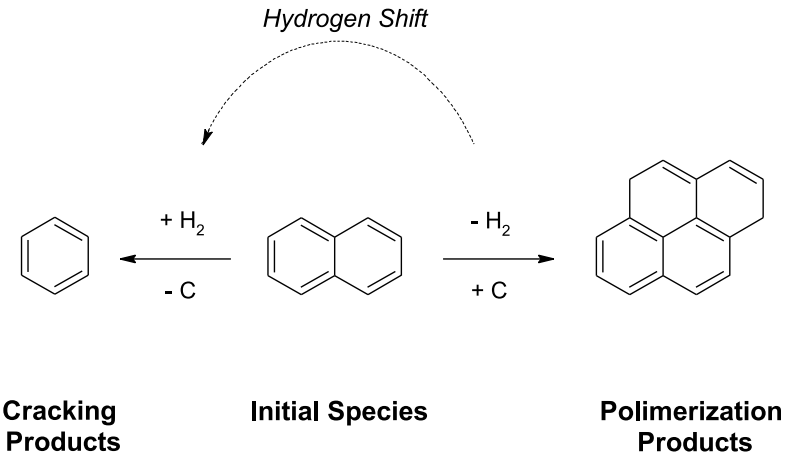

Figure 2.1 : Hydrogen shift during thermal tar treatment which is necessary for production of organic cracking and polymerization products.

They are all produced by their release from tar molecules. The initial abstracted radicals are stabilized by the addition of atomic hydrogen. Only very few of the organic cracking products react back to soot, so they can be assumed stable.

As the hydrogen content of aromatics decreases with increasing aromaticity, the co-occurrence of the cracking path relative to the polymerization path decreases. For example, the cracking path for benzene is equally important as its polymerization path, while the cracking path for naphthalene is relatively minor.

The main cracking paths of both benzene and naphthalene as given by Jess [44] are shown in figures 2.2 and 2.3. For benzene, ring-breaking hydration[4] reactions cause production of mainly methane and C2-hydrocarbons. The main cracking path of naphthalene is initiated by the hydration step to dihydronaphthalene, after which further hydrogen addition leads to benzene, methane and C2-hydrocarbons.

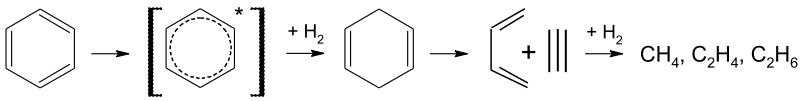

Figure 2.2 : Benzene cracking scheme [44].

Due to their low decomposition energies the cracking of alkylated-benzenes occurs at relatively low temperatures of 700 to 1000°C. The main cracking paths for the simplest alkylated-benzene 'toluene' are shown in figure 2.4. The main conversion

[4]Hydration: Addition of water or one of the elements of water (i.e. H and OH) to a molecular entity [56].

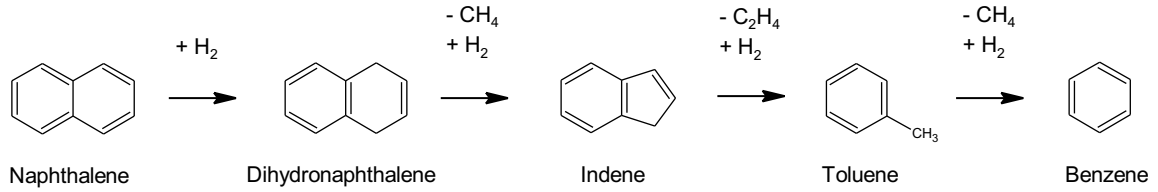

Figure 2.3 : Naphthalene cracking scheme [44].

products are hydrogen, methane and benzene. Apparently, the side chains of alkylated aromatics are first transformed into small cracking products, after which the parent aromatic remains for further thermal treatment. This means that the thermal treatment of alkylated aromatics only differs from the thermal treatment of non-alkylated aromatics by the formation of cracking products from their side chains.

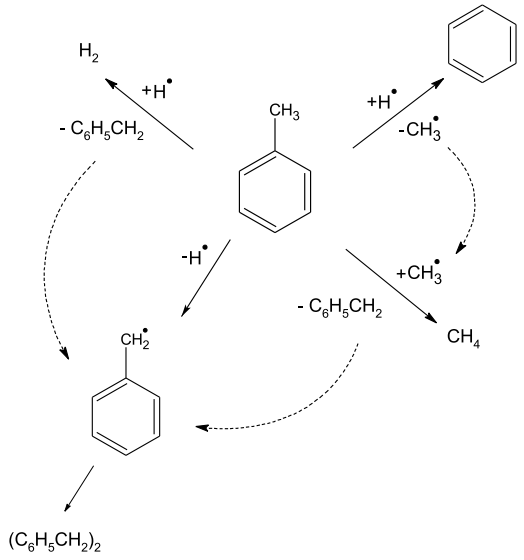

Figure 2.4 : Toluene cracking scheme [44,79].

Tar polymerization paths

Polymerization products formed during thermal tar treatment are various. These polymerization products will polymerize into soot-precursors and eventually into soot. With increasing treatment temperature, gas residence time and aromaticity, the soot production from converted tar increases while the soot-precursor level drops.

The formation of polymerization products and soot proceeds mainly by aromatic merging under release of hydrogen. Possible reaction paths of benzene and naphthalene into higher hydrocarbons are shown in figures 2.5 and 2.6. Striking is that the reaction path from naphthalene into indene can lead to polymerization as well as cracking products.

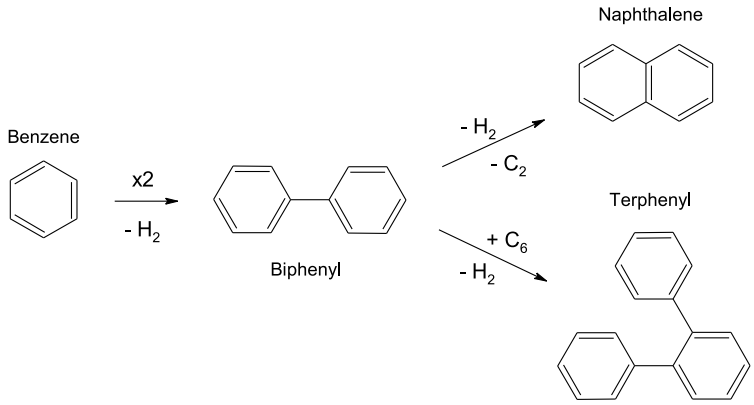

Figure 2.5 : Benzene polymerization scheme [44].

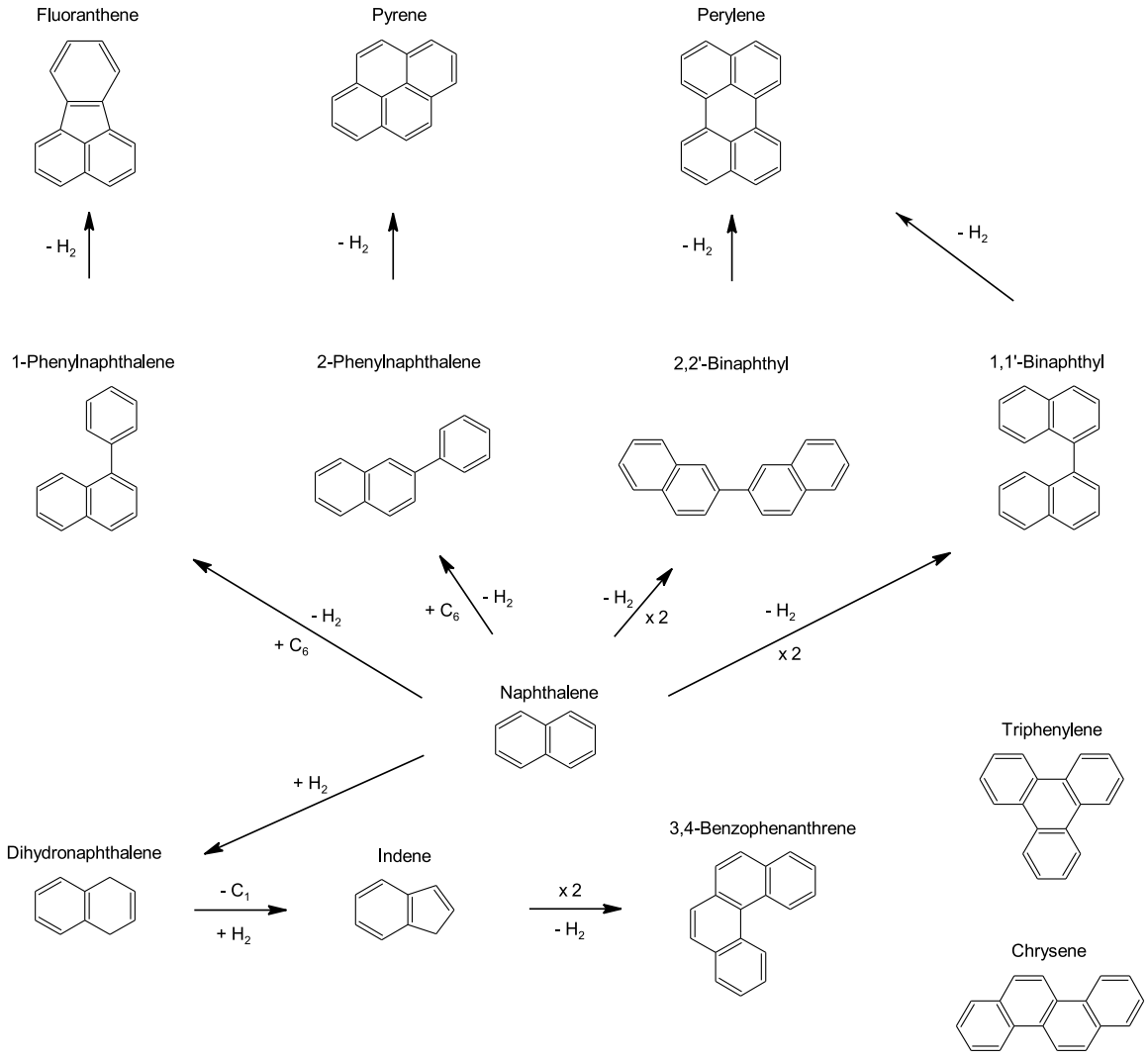

Figure 2.6 : Naphthalene polymerization scheme [44].

2.1.2 Steam influence on thermal tar treatment

According to Jess, Miura et al., and Garcia and Hüttinger it generally shows that steam does not directly influence the primary cracking or the polymerization reactions during thermal tar treatment. This means that steam does not react with the primary tars.

However, steam does react with the primary reaction products (including the activated forms of the primary tar) of thermal tar treatment at high temperatures to form CO and H_2 by a steam gasification reaction. This implies that H_2O is added to an activated PAH to form a hydroxyl group under release of a hydrogen radical. Subsequently, the O-atom is released together with its bonding C-atom to form CO and a reduced PAH molecule. Successively, part of the CO is converted into CO_2 by the water-gas-shift reaction:

$$CO + H_2O \rightarrow CO_2 + H_2. \tag{2.1}$$

The steam gasification generally increases with increasing temperature. Steam gasification of soot starts at approximately 1100°C, while steam gasification of methane starts above 1200°C. Contrary to the general behaviour, the steam gasification of soot reaches a maximum at approximately 1250°C. This maximum is probably caused by changes of the soot-structure into less reactive soot, which causes the steam gasification of soot to stop above 1400°C.

The amount of gas produced by the steam gasification of soot and cracking products can easily exceed the amount of gas produced by the initial cracking and polymerization reactions. Further, the gases produced by the steam gasification reactions influence the primary cracking and polymerization of tar. Therefore steam indirectly influences the primary cracking or polymerization reactions of thermal tar treatment.

2.1.3 Ambient gas influence on thermal tar treatment

The influence of ambient gas on thermal tar conversion can probably be derived from the chemical balances of the reactions taking place. Addition of a certain ambient gas can generate driving forces which can direct or redirect species balances of reactions. For instance, competitive inhibition by high concentrations can stop irreversible reactions or reverse reversible reactions.

Hydrogen

The influence of hydrogen on thermal tar conversion is two-fold. First hydrogen inhibits polymerization by competitive inhibition and stimulates cracking reactions by increased driving forces. This directs the general thermal tar reactions away

from polymerization and towards cracking. Second, as hydrogen-radicals react fast with unsaturated molecules, any recombination of unsaturated molecules or reaction with other (carbon-containing) radicals is inhibited. Because soot formation is suppressed, the total conversion of benzene and naphthalene is decreased by the presence of hydrogen.

Hydrogen does not necessarily show a positive effect on formation of cracking products, however, its effect also depends on the rate determining steps in the cracking paths. This is illustrated by Jess [44], who gives that in the possible benzene hydropyrolysis mechanism of figure 2.2, the first step, the destabilization of the benzene ring, is the rate-determining step. Consequently, the influence of hydrogen on the formation of cracking products from thermal benzene cracking is negligible. The rate determining step in the naphthalene cracking path is probably the hydration step into dihydronaphthalene, because of which the rate of conversion of naphthalene into cracking products is increased by hydrogen.

Other gases

The influence of most other major gases is probably not as profound. Methane might restrain methane-releasing cracking reactions by competitive inhibition. CO and CO_2 probably also have a competitively inhibiting effect on the secondary steam gasification reactions. Further, CO and CO_2 might have a (small) effect on the hydrogen and steam concentrations via the water-gas-shift reaction. Due to its inertness, the influence of nitrogen will probably be negligible.

2.1.4 Summary thermal tar treatment

From literature it shows that thermal cracking of tar is possible, but will mostly be accompanied by tar polymerization. This is a consequence of a necessary hydrogen shift. Hydrogen released during the formation of polymerization products is used to stabilize cracking products. If the hydrogen content of tar increases, more hydrogen has to be released for formation of polymerization products. This causes a shift in the balance towards more cracking products and less polymerization products.

A shift towards cracking products can also be caused by an increased ambient gas hydrogen concentration. The influence of other ambient gas species is probably relatively minor, except for steam. Steam helps the conversion of tar towards H_2 and CO by steam gasification of primary thermal tar conversion products.

2.2 Oxidative tar treatment

During oxidative tar treatment molecular oxygen is used to combust tar containing mixtures. Compared to thermal treatment, the addition of oxygen highly increases the reaction rates, by which the necessary residence times are greatly reduced. The amount of oxygen introduced is often measured by the air-excess ratio λ, which is the ratio of the amount of oxygen introduced over the amount of oxygen necessary for stoichiometric combustion. By varying the air-excess ratio of the treatment, different treatment effects can be expected.

In this section a summary is given of literature written on oxidative treatment of aromatics. Especially important is that the addition of O_2 introduces pathways towards tar cracking and growth other than those for thermal treatment. These differences start already in the chain initiation, and proceed in all subsequent reactions. Here the main reaction paths of aromatics during oxidative treatment are discussed. This includes a discussion of the main aromatic destruction and growth paths.

2.2.1 Chain initiation

Literature generally agrees that oxidative treatment gives higher reactivity, and has a lower apparent activation energy than thermal treatment. The differences between thermal and oxidative reactions rely on the relative reactivity of the different radicals produced [6,69]. Under thermal treatment conditions hydrogen (H) and methyl (CH_3) radicals are the active radicals. When oxygen is present in the reacting mixture, hydrogen (H), oxygen (O), hydroxyl (OH) and hydroperoxy (HO_2) radicals become dominant. The latter are capable of accelerating the hydrocarbon decomposition path by increased and faster H-atom abstraction. Oxygen is thus an excellent initiator of free radicals and plays an outstanding role in initiating reactions [6, 51, 52].

Besides, oxygen (partially) oxidizes relevant hydrocarbons to exothermically form carbon monoxide and water, releasing the heat necessary for propagation reactions of the remaining hydrocarbon [52].

2.2.2 Low- and high-temperature radical behaviour

Once the first chain initiating free radicals are produced, their interactions with present tar species become interesting. Barckholtz [4] kinetically studied the influence of single radicals (H, O, and OH) on benzene, and found clear differences between low- and high-temperature mechanisms. Shaddix [74] experimentally studied the high-temperature oxidation of alkylated and non-alkylated PAH, from which radical influences on PAH at different temperatures can be derived.

At low temperatures, the radical addition path is exothermic, and the activation barrier of that channel is lowest. This means that for H, O, and OH at low temperature, the radical addition channel to aromatics is the preferred path.

At high temperatures, the collision energies are high enough to overcome the endothermicity of the H-atom abstracting reactions, and the hydrogen abstraction channel becomes the dominant pathway for H, O and OH. Although the preference for the abstraction path by OH has been questioned in favor of an addition-elimination path that generates phenol[5]: $R + OH\cdot \rightarrow ROH\cdot \rightarrow ROH + H\cdot$.

The hydrogen abstraction rate will increase with decreasing C-H bond dissociation energy, which means that the abstraction rate increases for increasing aromatic size: phenanthrene $>$ naphthalene $>$ benzene. Further, again because of the bond dissociation energy, the barrier to H-atom abstraction from five-membered rings is higher than that for six-membered rings, which will show important in the path towards aromatic growth.

The crossover-temperatures at which the abstraction channel becomes kinetically and thermodynamically preferred over the addition channel for monocyclic aromatic rings increases in the order OH $<$ O $<$ H. An increasing aromatic size will probably have different effects for the H and for the O and OH radical crossover-temperatures. The H crossover-temperature will probably decrease with increasing arene[6] size due to the weak type-2 and type-3 C-H bonds (referring to carbon atoms adjacent to one or two fused-ring carbons). The crossover-temperatures of O and OH, however, will probably increase for increasing arene size due to an increased stability of O- and OH-PAH adducts, which have a greater effect than the decreased bond strengths.

2.2.3 Low- and high-temperature reaction mechanisms

The radical addition to hydrogen abstraction turnover behaviour leads to high- and low-temperature zones of hydrocarbon oxidation, which have their own prevailing reaction mechanisms. The turnover-temperature at which the transition between the high- and low-temperature mechanisms occurs depends on the conditions, such as the kind of hydrocarbon, the kind of radicals, the rate of oxidation, and the pressure [69,73]. According to Ranzi [69], the transition occurs roughly at 1000 K.

In the transition regime the overall rates of reaction decrease rather than increase with increasing temperature level, because of which it is sometimes referred to as the region of negative temperature coefficient [30].

[5] Phenols: Species having one or more hydroxy groups attached to a benzene or arene ring [56].
[6] Arenes: Monocyclic or polycyclic aromatic hydrocarbons [56].

The low-temperature mechanism of hydrocarbon oxidation is a complex process and involves the propagation and chain branching reactions of large unstable but long-lived (metastable) radicals, because of which the reaction rate only slowly increases with temperature [35, 69]. The low-temperature regime is also denoted as the cool flame region. The low-temperature oxidation of aromatics is characterized by the formation of metastable organic peroxy radicals (ROO·) from reaction of a fuel radical (R·) with molecular oxygen: $R\cdot + O_2 \leftrightarrow ROO\cdot$ [55, 73]. The formed phenylperoxy-type radicals prefer to form dioxiranyl radicals, which can subsequently react via a complex mechanism to all kind of decomposition products [5, 23, 24]. However, at temperatures greater than 432 K, cleavage of the O-O bond to form a phenoxy-type radical and an oxygen atom is the thermodynamically preferred pathway. Phenoxy-type radicals and phenols can, according to Barckholtz [5], also be produced at low temperature by reaction of phenylperoxy-type radicals with arene molecules: $ROO\cdot + R \rightarrow RO\cdot + ROH$.

The high-temperature regime is basically controlled by rapid chain branching reactions, and the development of a H, O, and OH containing radical pool [73]. The reactive biradical O-atom participates in direct attack on the fuel and intermediates. Next to the H-abstraction reactions from hydrocarbons, thermal hydrocarbon decomposition processes play a great role. Especially in the oxidation chemistry of aromatics with their high activation energies, decomposition reactions increasingly contribute to the fuel decay as the temperature rises [55, 74]. If the temperature is high enough, direct ring cleavage may become an important decomposition pathway [74].

Shaddix, Ranzi and Barckholtz [5, 69, 73] all give that the transition regime between the low- and high-temperature mechanisms is characterized by the diminishment of peroxy radical formation due to increasing reversibility of $R\cdot + O_2 \leftrightarrow ROO\cdot$ with increasing temperature. It is the competition of the nett flux of the reversible reaction with that of H-abstraction which causes the negative temperature coefficient behaviour at the upper boundary of the low-temperature regime. Next to reversible reaction products, phenylperoxy-type radicals can also decompose into phenoxy radicals and O atoms in the intermediate regime [5].

2.2.4 Low- and high-temperature ring-destruction

Very important to the rate of ring destruction in the low-temperature regime, is the H-addition to arenes to form activated cyclohexadienyl[7][8]-type radicals. The cylcohexadienyl-type radicals can further react in various ways, of which two of

[7] Cyclo-: A prefix used in names to designate a ring structure [56].

[8] Dienes: Compounds that contain two fixed double bonds (usually assumed to be between carbon atoms) [56].

them lead to ring destruction. Either unimolecular ring fragmentation leads to direct ring destruction. Or, addition of a second H to either the activated or stabilized cyclohexadienyl-type radical leads to formation of a weak ring structure that can be readily broken [74].

In the high temperature regime, reactions with O, HO_2, and O_2 are key to destruction of rings as well as removal of sidechains of PAH[9] [73]. Regardless of the aromaticity, ring consumption in the high-temperature range is expected to occur primarily via the general pathway shown in figure 2.7. Aromatic ring rupture is initiated by formation of resonantly stabilized phenoxy-type radicals, either by exothermic metathesis reactions[10] of arenes with molecular oxygen, or by O addition reactions to aryl[11] radicals. The phenoxy-type radicals decompose at high temperatures to cyclopentadienyl-type radicals under release of CO. If sufficient oxygen is available, the cyclopentadienyl-type radicals form cyclopentadienonyl by reaction with O or HO_2. The cyclopentadienonyl finally releases CO to break the ring structure.

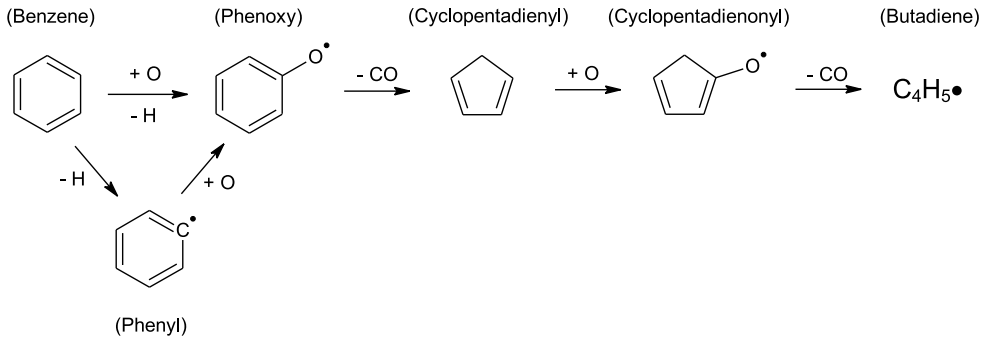

Figure 2.7 : General pathway for ring consumption in the high-temperature range.

2.2.5 Hydrocarbon growth at high temperature

There is consensus among several authors [27, 54, 70, 72, 81] that the formation of high-molecular-mass aromatic hydrocarbons occurs both through the resonantly stabilized radical (RSR) mechanism as the HACA mechanism. In both mechanisms reactive sites on aromatic hydrocarbons are activated by hydrogen abstraction [27, 72], after which a growth process forms stable PAH molecules [27]. Next to the RSR and the HACA mechanism, combination of aromatic hydrocarbon radicals and

[9] PAH: Poly Aromatic Hydrocarbons.

[10] Metathesis reaction: A bimolecular process formally involving the exchange of a bond (or bonds) between similar interacting chemical species so that the bonding affiliations in the products are identical [56].

[11] Aryls: Species derived from arenes by removal of a hydrogen atom from a ring carbon atom [56].

PAH isomerization are also of influence on the production of aromatic hydrocarbons [54]. The relative contributions of each reaction mechanism are likely to depend on the reigning conditions.

The hydrocarbon growth proces in the RSR-mechanism is caused by the polymerization of small PAH's by resonantly stabilized radicals. These radicals are formed in the oxidative pathways caused by the presence of molecular oxygen [81]. Resonantly stabilized radicals are important aromatic and PAH precursor species as they can build up in concentration within the flame since they are relatively resistant to oxidation by O_2 [54]. Examples of resonantly stabilized radicals are: cyclopentadienyl- ($c-C_5H_5$), propargyl- ($HCCCH_2$), allyl- (H_2CHCH_2) and 1-methylallenyl- (H_2CCCCH_3) radicals [81]. The key reactions in the RSR-mechanism leading to aromatics formation are: combinations of resonantly stabilized radicals, propargyl addition to benzyl radicals, and the sequential addition of resonantly stabilized radicals to aromatic rings [81].

The growth process in the HACA-mechanism proceeds by acetylene additions to activated aromatic or small aliphatic hydrocarbons. Additions of two single acetylene molecules to an aromatic can increase the ring number by one. Contrary to the resonantly stabilized radicals, acetylene is not resistant to oxidation. Therefore, the rate of formation of aromatics as predicted by the HACA-mechanism is reduced by the addition of O_2.

The role of both aromatic growth mechanisms is influenced by the fuel/oxygen ratio, and by the process temperature. In oxygen rich situations, the RSR-mechanism is the main aromatics forming mechanism. In very fuel-rich and pyrolysis situations, or when O_2 is completely consumed, the HACA-mechanism is the main aromatic forming mechanism [81]. However, Ranzi [70] showed that if the temperature is low enough in oxygen-rich situations, the HACA mechanism could still play a significant role.

As an example of a typical hydrocarbon growth path, the RSR-mechanism controlled path towards PAH formation for a n-butane-oxygen-argon flame is shown in figure 2.8. The most important steps involved in this PAH formation process require the phenyl and naphthyl to be oxidized by O_2. Cyclopentadienyl appears to be important in the growth process of aromatic species and formation of soot, particularly during formation of naphthalene and phenanthrene [75]. This is supported by Marinov [54] who gives that the removal of cyclopentadiene and propargyl radical by H atoms inhibits naphthalene production, while reactions that can increase cyclopentadienyl formation enhance naphthalene production.

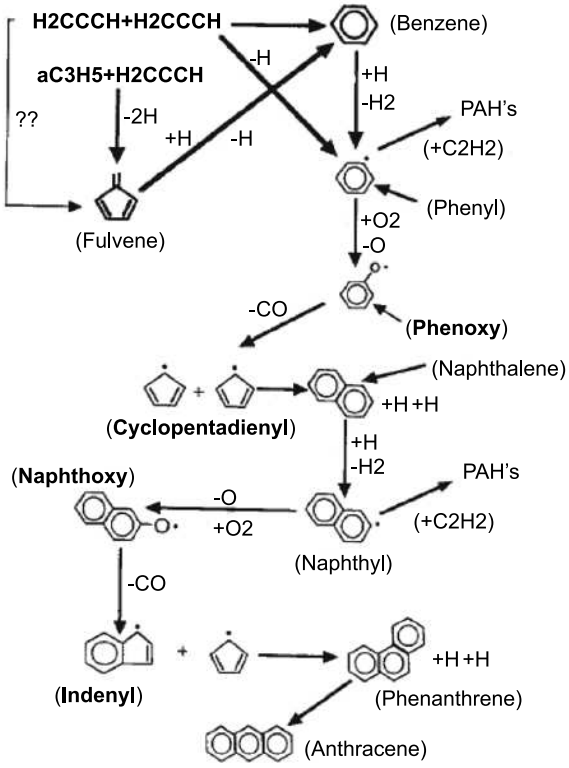

Figure 2.8 : Reaction flux/pathway diagram for the important pathways leading to aromatic and polycyclic aromatic hydrocarbon formation in a n-butane-oxygen-argon flame [54].

2.2.6 Alkylated aromatics kinetics at high temperature

According to Shaddix [73, 74], many of the important reactions of the single and multiple alkylated benzenes and PAH are analogous to the reactions of corresponding aliphatic species, i.e. the aromatic rings often act as an unreactive ligand replacing an H atom on the corresponding aliphatic species. This means that the aromatic ring is not significantly attacked until the side chains are removed. The high temperature oxidation of alkylated benzenes or PAH generally leads to the formation of phenyl-type radicals or non-alkylated aromatics.

In absence of sufficient O_2 to oxidize the alkylated aromatics, acetylene addition can also lead to aromatic hydrocarbon growth [54]. For instance, as shown in figure 2.9, acetylene addition to a benzyl radical can lead to the formation of indene. The hydrogens on the five-membered ring part are very weak and can therefore be easily abstracted leading to indenyl. The indenyl-type radicals can react further with cyclopentadienyl to phenanthrene.

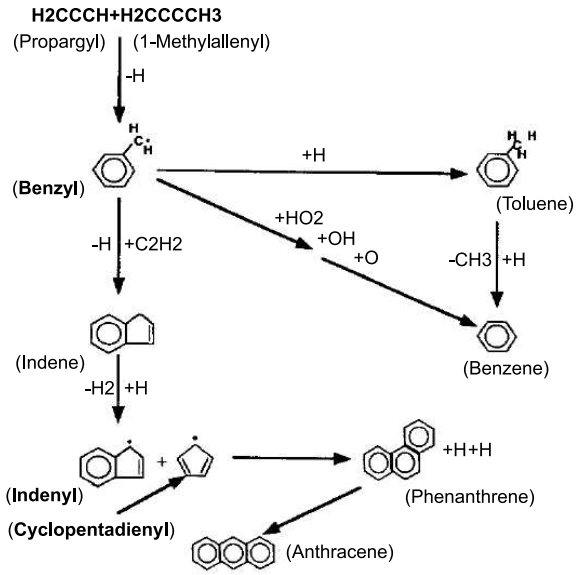

Figure 2.9 : Reaction flux/pathway diagram for the important pathways leading to aromatic, branched aromatic, and polycyclic aromatic hydrocarbon formation in a n-butane-oxygen-argon flame [54].

2.2.7 Steam influence on oxidative tar treatment

Both the modeling and the experimental work of Skjøth-Rasmussen et al. [75] indicate a significant chemical effect of water vapor on the gas-phase chemistry of fuel-rich systems. Water vapor affects the oxidation chemistry of acetylene and reduces or even eliminates formation of soot at temperatures above 1500 K. It is believed that formation of OH radicals from water vapor accounts for changes in the

acetylene chemistry by oxidation. Reduced acetylene concentrations would lead to reduced aromatics growth.

2.2.8 Summary oxidative tar treatment

Compared to thermal treatment, the reactivity of oxidative treatment is increased by molecular oxygen. Molecular oxygen accelerates the chain initiating hydrocarbon decomposition path by increased and faster H-atom abstraction. Introduction of oxygen further creates a pool of very reactive O containing radicals, that become dominant over the ones present during pyrolysis. The H-atom abstraction rates increase for increasing aromaticity. It further seems that alkylated species are converted into nonalkylated species before significant H-atom abstraction from arenes takes place.

After the H abstracting chain initiation reaction, the chain propagation reactions become temperature dependent. At low temperatures the channel for addition of radicals and molecular oxygen to hydrocarbons prevails. At high temperatures the endothermic hydrogen abstraction channel becomes dominant. The turnover temperature between the low- and the high-temperature mechanism is determined by the reversibility of the addition reactions and the strength of the abstraction reactions.

The temperature zones each have their own hydrocarbon oxidation mechanism. In the low-temperature mechanism free radicals or molecular oxygen add to hydrocarbons, after which internal rearrangements and subsequent reactions create a wide variety of products. In the high-temperature mechanism, oxidation of activated aromatics forms phenoxy-type radicals, which mainly decompose to form CO and a cyclopentadienyl-type radical. The amount of oxygen in the process determines whether the cyclopentadienyl-type radicals will oxidize and cause ring destruction, or will rearrange with another cyclopentadienyl-type radical to cause ring growth. According to Marinov it shows that PAH formation is promoted by small amounts of O_2 rather than inhibited [54]. However, as the temperature rises direct aromatics decomposition increasingly contributes to fuel decay.

It shows there are basically two mechanisms towards aromatic growth, the resonantly stabilized radicals mechanism and the H-abstraction acetylene addition mechanism. Based on pathway diagrams of several authors it can be concluded that these two mechanisms both seem to play a role next to each other, with the reaction conditions determining which mechanism is dominant. The HACA mechanism seems dominant in low temperature and in very fuel-rich situations, whereas the RSR mechanism seems dominant in fuel-rich to fuel-lean situations.

2.3 Discussion

Thermal treatment of tar containing product gas can be used to convert part of the tar into organic cracking and polymerization products. For high tar conversion, high temperatures and long residence times would be necessary. It has become likely that a high hydrogen and steam content of the product gas would help to direct the conversion more towards cracking products. Therefore, it might be possible to obtain tar cracking by thermal treatment of a hydrogen- or steam-rich tar containing atmosphere. However, experiments by Houben [39] show that during thermal product gas treatment mainly polymerization products are formed. Apparently the hydrogen and steam contents of the product gas in those experiments were not high enough to direct the main part of the thermal conversion process towards cracking.

Oxidative treatment of tar containing product gas can lead to low- and high-temperature tar conversion mechanisms. However, according to Heywood [35], methane only shows oxidation according to the high-temperature mechanism, and benzene and other aromatics hardly give any low-temperature oxidation. So it becomes unlikely that during partial product gas combustion aromatics are converted in the low-temperature regime. This means that the aromatics will be converted by the reaction paths as described by the high-temperature mechanism.

High-temperature oxidation leads to chemical reactive species and high temperatures. Ring rupture has to occur by radical pool attack or by thermal decomposition. The oxygen level in the reactions determines whether the temporary ring rupture leads to permanent ring rupture (cracking), or to ring growth (polymerization). Remarkable is that according to literature, permanent ring rupture should be stimulated by an increasing oxidation level, while the measurements by Houben shown in figure 1.3 show just the opposite. Nevertheless, literature and experiments do agree on the driving effect of hydrogen towards tar cracking.

It should be noted that next to the temperature and the amount of oxygen, the physical transport processes play an important role in hydrocarbon oxidation. A simple example is given by Granata [34], who gives that there are different kinetic paths in benzene formation in diffusion and premixed flames because of the fuel-air mixing effect. Geisbrecht [30] further gives that apparent heterogeneous influences on product distributions arise indirectly from finite thermal transport processes. McEnally [55] finally gives that in nonpremixed flames, due to the absence of oxygen on the fuel side, the reaction products tend to react with one another, forming larger hydrocarbons and ultimately soot, instead of oxidizing to carbon dioxide and water.

2.4 Conclusions

It can be concluded that thermal and oxidative tar treatment both have their own specific tar conversion mechanisms, in which free radicals play a dominant role. Both treatment techniques can lead to cracking as well as polymerization of aromatics, depending on the conditions.

Because thermal treatment is a relatively slow process, the treatment times are next to the treatment temperature, of influence on the conversion of aromatics. Thermal treatment always leads to a balance between cracking and polymerization reactions due to a necessary hydrogen shift. The balance can be shifted towards cracking by ambient hydrogen as well as steam.

Oxidative treatment is a rapid process due to the production of a reactive radical-pool. The temperature and the level of oxidation determine the conversion processes taking place during oxidative treatment. The most likely conversion mechanism for aromatics is the high-temperature conversion mechanism, in which the amount of oxygen determines whether tar cracking or polymerization will take place. The more oxygen present, the more tar cracking and oxidation reactions take place. However, at very low air-excess ratios, the importance of polymerization reactions by the oxidative treatment can even exceed those of thermal treatment. It is likely that ambient gases have a similar influence during oxidative treatment as they have during thermal treatment. It might even occur that hydrogen stimulates tar cracking by steam gasification, as steam is produced during hydrogen oxidation.

The tar conversion mechanisms show both similarities and contradictions to the experimental results by Houben. The effect of the fuel hydrogen content can be explained by the driving effect of hydrogen towards cracking reactions. The effect of the air-excess ratio cannot be explained by the conversion mechanisms. The only theoretic explanation for polymerization reactions at relatively high air-excess ratios is that locally mixture fractions with low air-excess ratio are created, in which polymerization reactions are stimulated.

It becomes likely that the tar conversion found after partial product gas combustion is a consequence of both thermal and oxidative treatment. Oxidation reactions probably initiate high-temperature oxidative conversion reactions, which lead to either to cracking or polymerization products depending on the local fuel/oxygen mixture fractions. Further, high temperatures generated in the oxidation reactions, probably cause thermal conversion reactions that can also lead to both cracking and polymerization products depending on product gas composition.

Chapter 3

Chemical analysis of partial combustion

In this chapter[1] the chemical kinetics of partial product gas combustion are subject of study. Goal is to gain knowledge about operating conditions influencing tar cracking by partial combustion. Especially the roles of the fuel hydrogen content and the air-excess ratio are interesting, since these can be compared to experimental results.

In section 3.1, a hypothesis on tar cracking by partial product gas combustion is formulated. Based on this hypothesis the production of free radicals during partial combustion is studied in section 3.2. To investigate tar conversion by partial combustion, the kinetics of aromatic species during partial combustion are studied in section 3.3. Both kinetic studies are performed as a function of the fuel hydrogen content and the air-excess ratio. The results are discussed and compared to experimental results in section 3.4.

3.1 Introduction

To find the cause of tar cracking by partial combustion, figure 1.2 is again considered. The figure shows that inside the micro-scale swirl-burner small blue-colored combustion zones are created at each air injection hole. The color of the flames indicates that at each jet/cross-flow interaction plane, part of the product gas is combusted at high air-excess ratio. This means that most oxygen is consumed by just a small part of the product gas. It is thus unlikely that the 95% tar reduction as shown by Houben [39, 40] is caused by direct oxidation of the tar, as oxygen is consumed before it can come into contact with 95% of the tar.

Tar in the micro-scale swirl-burner is probably not converted by direct oxidation, but more likely by the two side effects of the fractional product gas combustion: raised temperature and/or the formation of reaction products. Thermal treatment can lead to tar cracking (especially at high hydrogen concentrations), but will probably also lead to tar polymerization, as explained in chapter 2. Furthermore, due

[1] Part of this chapter has been published as: T.A. van der Hoeven, H.C. de Lange, and A.A. van Steenhoven. Analysis of hydrogen-influence on tar removal by partial oxidation. *Fuel*, 85:1101-1110, 2006. [38]

to the low reaction rates at thermal treatment, large residence times would be necessary to obtain the experimental partial combustive tar cracking results by thermal treatment. Therefore, it is expected that next to the raised process temperature, (intermediate) product gas combustion-products are necessary to activate tar cracking. This is supported by several studies into the partial oxidation of methane [2, 19, 62, 84], which state that oxygen is rapidly consumed by part of the fuel in a fast oxidation zone, after which the remaining fuel is converted by the oxidation-products in a (slow) conversion zone.

Cracking of aromatic hydrocarbons can be achieved by ring rupture. The first steps towards ring rupture at high temperature, are hydrogen abstraction and oxidation reactions by the influence of free radicals and molecular oxygen, as explained in chapter 2. As molecular oxygen is probably rapidly consumed (see previous paragraph), it is likely that the naphthalene cracking seen in the experiments by Houben is caused by free radicals that are produced during combustion of a part of the product gas. A hypothesis can now be formulated:

> *Tar cracking by partial combustion is caused by free radicals produced during combustion of a part of the product gas at a relatively high air-excess ratio.*

It is very hard, nearly impossible, to perform measurements on free radicals during partial combustion. Therefore, to verify the hypothesis, simulations are done on the chemical kinetics of partial combustion. A first model is used to study the order of magnitude of concentrations and residence times of free radicals during partial combustion of tar-free product gas. Goal is to find trends between the fuel hydrogen content or air-excess ratio and the production and residence time of free radicals during partial combustion. This relation can be compared to the tar conversion results shown in figures 1.3 and 1.4, which might indicate whether the hypothesis stated above is correct. A second, separate, model is used to study the cracking and polymerization behaviour of tar species during combustion of product gas in different oxidation regimes. Goal is to find which parameters are likely to stimulate tar cracking. This may lead to a better understanding of the chemical reactions causing tar cracking during partial product gas combustion.

Partial combustion of tar containing product gas is a highly complex mechanism in which diffusion, turbulent mixing, and chemical reactions play a role. Often complicated heterogeneous behaviour is observed, which indirectly is a consequence of the finite rate of thermal transport processes [30]. So the full partial combustion process is hard to simulate including both the chemical reactions as well as the physical transport processes. That is why for both simulations the transport and chemical processes are decoupled by assuming that the transport processes are infinitely fast compared to the chemical kinetics.

Decoupling the chemical kinetics and the physical transport processes leads to chemical time-scales of the partial combustion process. To put these chemical time-scales into perspective, they have to be compared to the time-scales of the transport processes. Since the time-scales of physical transport in the micro-scale swirl-burner probably depend on both diffusion and on turbulent mixing, they cannot be readily determined. However, typical time-scales of physical transport can be estimated using the average flow velocities in the swirl-burner and the swirl-burner dimensions shown in figure 5.2(b). At a fuel power of 2.8 kW and a Lower Heating Value (LHV) of 4.2 MJ/Nm^3, the average gas velocity in the burner, based on the product gas flow and the burner diameter, becomes 1.2 m/s. Adding air at an air-excess ratio of 0.2, increases the average gas velocity to 1.4 or 1.5 m/s, depending on the fuel hydrogen content. The air flow velocity in the injection holes varies from 5.6 to 6.8 m/s, depending on the fuel hydrogen content. A characteristic length-scale of 50 mm (the height of the burner above the air injection holes), gives a typical residence time of reactive mixture in the burner of $3.6{\cdot}10^{-2}$ seconds. An estimated characteristic length-scale of 9 mm (the length of the visible flames), gives (based on the air injection velocity) a typical residence time of air in the combustion zone of approximately $1.5{\cdot}10^{-3}$ seconds.

3.2 Kinetics of free radicals

To study the concentrations and the residence times of free radicals during partial combustion, a model is developed. Using this model, the concentrations of small chemical species can be studied as a function of their residence time during an approximate partial combustion process of tar-free product gas. The concentrations and residence times of the main free radicals are studied as a function of the fuel hydrogen content and the air-excess ratio of the partial combustion process. To evaluate the results, the computed concentrations of some major gas species are compared to experimental results from literature.

3.2.1 Modeling partial combustion

The partial combustion process is considered a two-step process, following the two-step oxidation/conversion theory of partial methane oxidation. This is modeled by two successive reactors, as can be seen in figures 3.1 and 3.2. The first reactor is fed by a model product gas with a stoichiometric amount of air to represent the oxidation process at high air-excess ratio in the primary reaction zone. After a certain residence time the reaction products of the first reactor are mixed in the second reactor with extra product gas, to represent the conversion process in the secondary reaction zone.

Decoupling of the chemical kinetics and the physical timescales is integrated in the reactors using the Perfectly-Stirred-Reactors code of the Chemkin 2.0 package [32]. This code assumes a small thermally insulated chamber with both a feed stream and a product stream. After the reaction components reach the reactor, the feed is instantaneously completely mixed. The walls of the chamber are non-catalytic, and the flow through the atmospheric constant-volume reactor is characterized by a nominal (average) residence time τ. The reactor volume does not influence the model outcomes and is thus chosen arbitrarily, due to which the reactor volume- and mass-flow also become arbitrary. A stationary Perfectly Stirred Reactor (PSR) thus describes the mixture situation and temperature in the reactor only as a function of the nominal residence time. PSR's are used to model the partial combustion process because they assume infinitely fast transport processes, due to which the time-scales of the chemical kinetics can be estimated. Further, PSR's model a continuous feed of fresh reactants, which is also present in the swirl-burner of figure 1.1.

It should be noted that the computed results are only indicative, since in the real situation undoubtedly transport processes play an important role. Therefore, the computations are only indicative for the absolute magnitude of chemical timescales and the concentrations of free radicals.

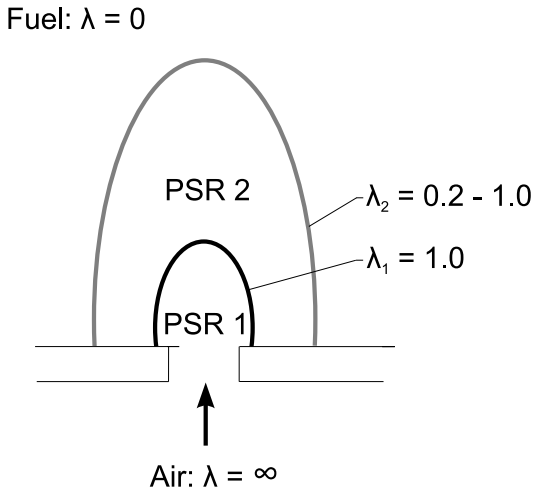

Figure 3.1 : Representation of two-step PSR-model in supposed partial combustion process.

The applied nominal residence time of the gases in the first PSR (τ_1) is based on the moment of peak amounts of radicals in the reactor, which in reality is likely reached near the flame front position. Peak amounts of radicals are determined from the summed mole fractions of H·, O· and OH·. These are the three main radicals as they each have mole fractions several times higher than any other free radicals present. It is chosen to base τ_1 on the peak amounts of radicals because it is a hypothetic goal to transfer as much free radicals as possible into the conversion zone.

Further, τ_1 then presumably shows best the influence of the secondary conversion step on the free radicals level in the partial combustion process. Because the primary reaction zone is assumed at stoichiometry, the air-excess ratio in the first PSR (λ_1) is equal to 1.0.

The average air-excess ratio in the second PSR (λ_2) (based on the summed air and product gas inputs in both reactors) is lowered by adding extra product gas to the reaction products of the first PSR. By varying the amount of extra product gas added, λ_2 is varied between 1.0 and 0.2. The air-excess ratio is varied to check the influence of the oxidation level on the reactions in the conversion zone. The input of the second PSR is calculated using:

$$\alpha \cdot MF_{\mathrm{PSR1-result}} + (1-\alpha) \cdot MF_{\mathrm{Product-gas}} = 1.0 = MF_{\mathrm{PSR2-input}}, \tag{3.1}$$

in which $MF_{\mathrm{PSR1-result}}$ is the resulting gas composition of PSR1 in mole fractions, $MF_{\mathrm{Product-gas}}$ the product gas composition in mole fractions, $MF_{\mathrm{PSR2-input}}$ the gas input composition for PSR2 in mole fractions, and α a proportionality factor. Using the molar fraction of product gas over air at stoichiometry MR_{st}, the proportionality factor α is equal to:

$$\alpha = \frac{\frac{MR_{\mathrm{st}}}{\lambda_1}+1}{\frac{MR_{\mathrm{st}}}{\lambda_2}+1} \tag{3.2}$$

The nominal residence time τ_2 of the gases in the second PSR, is varied from practically nil to $1{\cdot}10^1$ seconds. The calculations are stopped at $\tau_2 = 1{\cdot}10^1$ seconds since the chemical time-scales are then already much longer than the physical residence times in the swirl-burner, and because the reactions then have reached practically constant concentrations.

The chemical reaction mechanism used in the two-step PSR model, is the GRI-Mech 3.0 reaction mechanism [76]. This mechanism is optimized for methane oxidation at air-excess ratios between 0.2 and 10, which encompasses the air-excess ratios of the partial combustion experiments by Houben [40]. According to Konnov [48], GRI-Mech 3.0 usually gives satisfactory agreement between experimental and modeled partial methane oxidation at temperatures above 1000 K. GRI-Mech 3.0 is chosen because the oxidation reactions of methane and hydrogen are both decently described in the mechanism, due to which it can reliably describe methane and hydrogen combustion.

The composition of the model product gas is varied to study the influence of the fuel hydrogen content on the presence of free radicals. The model product gases used are the same as those used in the experiments by Houben [40], and consist of methane, hydrogen and nitrogen. Although real product gas also contains carbon monoxide as a combustible component, it is not used in the model computations as there are yet no experimental results to back its influence. The lower heating

value of the model gas is held constant at 4.2 MJ/Nm^3. The fuel hydrogen content is varied from its minimum, 0.0 vol.%, to its maximum, 39.0 vol.%. The initial gas temperature is 473 K, which is equal to the gas temperatures in the experiments by Houben.

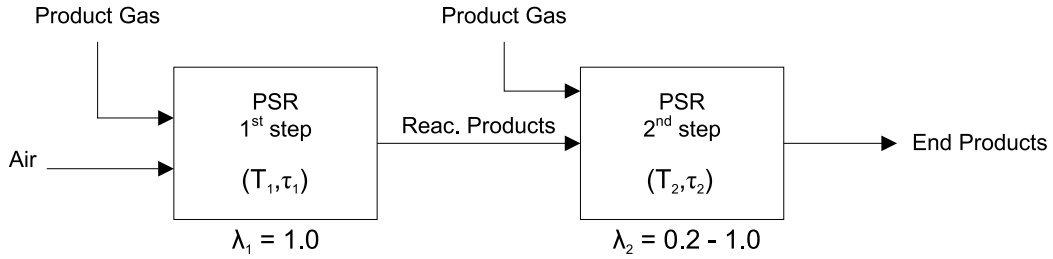

Figure 3.2 : Two-step PSR-model of partial combustion process

3.2.2 Free radicals in the oxidation zone

In the first PSR, an oxidation process proceeds when τ_1 exceeds the ignition delay time, due to which reaction rates and reactor temperature strongly rise. The combustibles methane and hydrogen are converted with oxygen into mainly carbon dioxide and water via intermediate reaction products like carbon monoxide and free radicals.

The summed concentrations of H·, O·, and OH· are given in figure 3.3 as a function of the nominal residence time τ_1 for different product gas compositions. As shown before in [36], the share of H· in the sum of the three main radicals is considerably larger than the share of O· and OH·. The results as a function of the fuel hydrogen content are very much alike, though there are large differences in their ignition delay times and the peak radical sums.

It shows that the higher FHC, the shorter the ignition delay time becomes. Apparently, hydrogen makes a gas mixture easier to ignite. Fotache [26] found that hydrogen addition significantly improved methane ignition through a mechanism of increased radical production and weakening of kinetic inhibition by diffusive separation of branching and termination reactions. The last argument, however, is not valid here, as a perfectly stirred reactor is considered. Therefore, the decreasing ignition delay time with increasing fuel hydrogen content is probably a consequence of increased radical production.

The argument by Fotache coincides with the increasing peak radical-sum computed for increasing FHC. Hydrogen shows a strong creator of free radicals in oxidation reactions, and/or methane is a free radical inhibiter. Another reason why an increasing FHC stimulates H· and OH· production, is given by the combustion

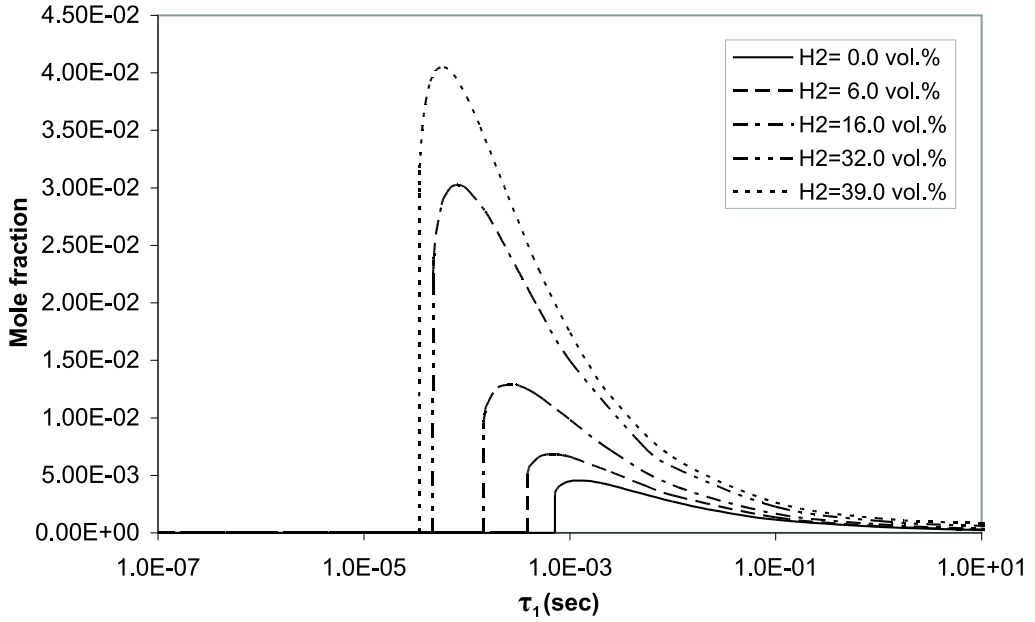

Figure 3.3 : Summed mole fractions of H·, O·, and OH· as a function of the nominal residence time as calculated by PSR1 for oxidation of 4.2 MJ/Nm^3 $CH_4/H_2/N_2$-mixtures with different fuel hydrogen contents at λ = 1.0.

enthalpies ΔH_i of the hydrogen and methane combustion reactions,

$$H_2 + \tfrac{1}{2}O_2 \rightarrow H_2O \qquad \Delta H_i = 241.8\,\text{kJ/mol} \tag{3.3}$$

$$CH_4 + 2O_2 \rightarrow CO_2 + 2H_2O \qquad \Delta H_i = 802.3\,\text{kJ/mol}. \tag{3.4}$$

To reach a certain combustion energy, 3.3 times more moles of hydrogen are necessary than of methane. The ratio of H-atoms per mole of hydrogen and methane is 1 and 2 respectively, because of which the amount of H-atoms per kilojoule is 1.65 times higher for hydrogen than for methane combustion. Hence, the higher the hydrogen level, the more H· and OH· radicals can be produced in the oxidation reactions.

Karim [46] further gives that the H·, O·, and OH· concentrations tend to increase rapidly with increasing combustion temperature. The calculated adiabatic combustion temperatures increase from approximately 1700 K for 0.0 vol.% hydrogen to approximately 2000 K for 39.0 vol.% hydrogen. The higher radical levels for increasing FHC might thus also be explained by the increasing combustion temperature.

The first PSR clearly shows that the sum of H·, O·, and OH· in stoichiometric product gas combustion increases with increasing FHC. Further, the higher FHC, the shorter the ignition delay time.

3.2.3 Free radicals in the conversion zone

The most characteristic results of the second PSR are shown in figures 3.4, 3.5, and 3.6 for FHC of 0.0, 16.0, and 39.0 vol.% respectively. Each figure shows the sum of H·, O·, and OH· as a function of τ_2 for different air-excess ratios. The radical level at $\tau_2 = 1.0{\cdot}10^{-7}$ seconds varies with the air-excess ratio due to the varying dilution of the PSR1-reactants, obtained by the extra product gas added in the second PSR to obtain the respective air-excess ratios.

To quantify the residence times of the three main radicals in the second reactor, lower mole fraction limits, or cut-off limits are introduced. At the moment the amount of radicals decreases below these cut-off limits, any further reactions are assumed negligible. Therefore, the residence times determined by the cut-off limits represent the maximum residence times necessary for chemical reactions. To enable comparison of the maximum necessary residence times at different FHC and λ, for each FHC the cut-off limit is chosen equal to its summed radical level for $\lambda_2 = 1.0$ at $\tau_2 = 1.0{\cdot}10^{1}$ seconds. The cut-off limits become equal to $2.5{\cdot}10^{-4}$, $3.7{\cdot}10^{-4}$, and $8.5{\cdot}10^{-4}$ mole fractions at FHC of 0.0, 16.0, and 39.0 vol.% respectively, and are shown by the dotted lines in figures 3.4, 3.5, and 3.6.

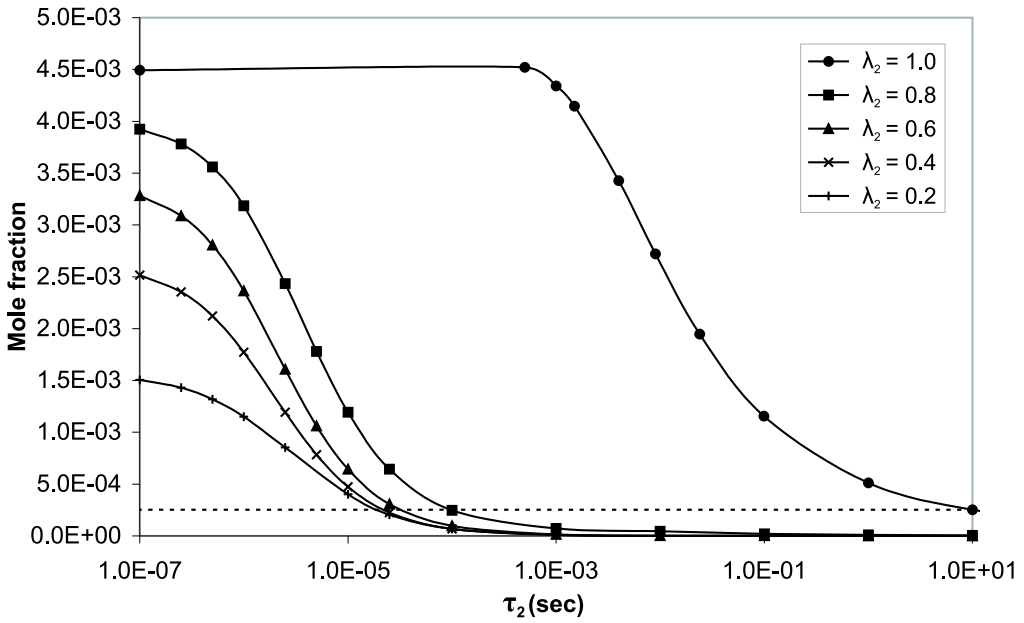

Figure 3.4 : Summed mole fractions of H·, O·, and OH· as a function of the nominal residence time as calculated by PSR2 at various λ_2 for a 4.2 MJ/Nm^3 $CH_4/H_2/N_2$-mixture having a FHC of 0.0 vol.%. Dotted line shows cut-off limit.

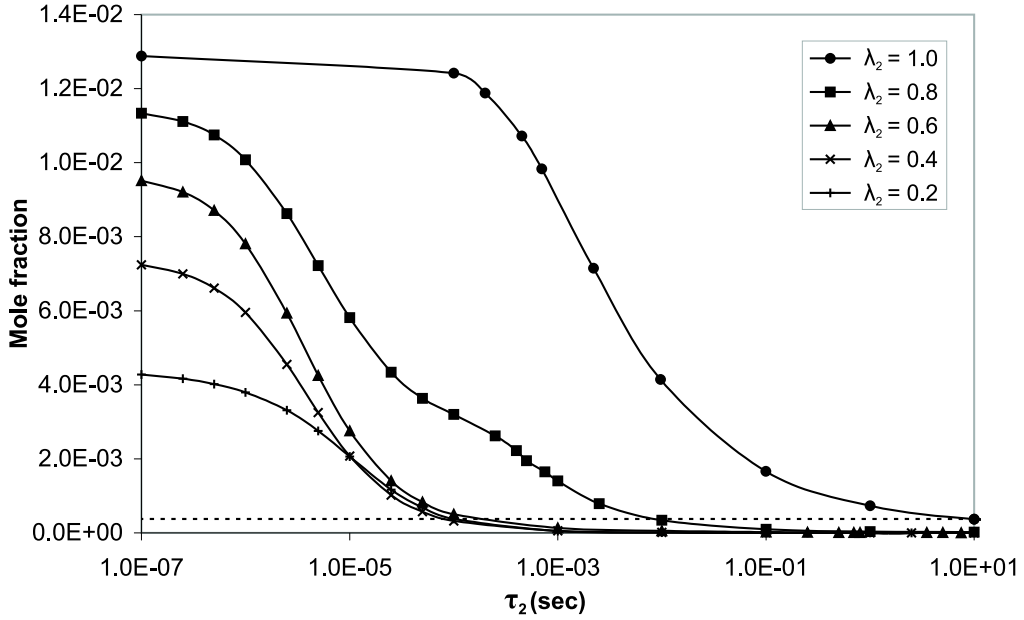

Figure 3.5 : Summed mole fractions of H·, O·, and OH· as a function of the nominal residence time as calculated by PSR2 at various λ_2 for a 4.2 MJ/Nm^3 $CH_4/H_2/N_2$-mixture having a *FHC* of 16.0 vol.%. Dotted line shows cut-off limit.

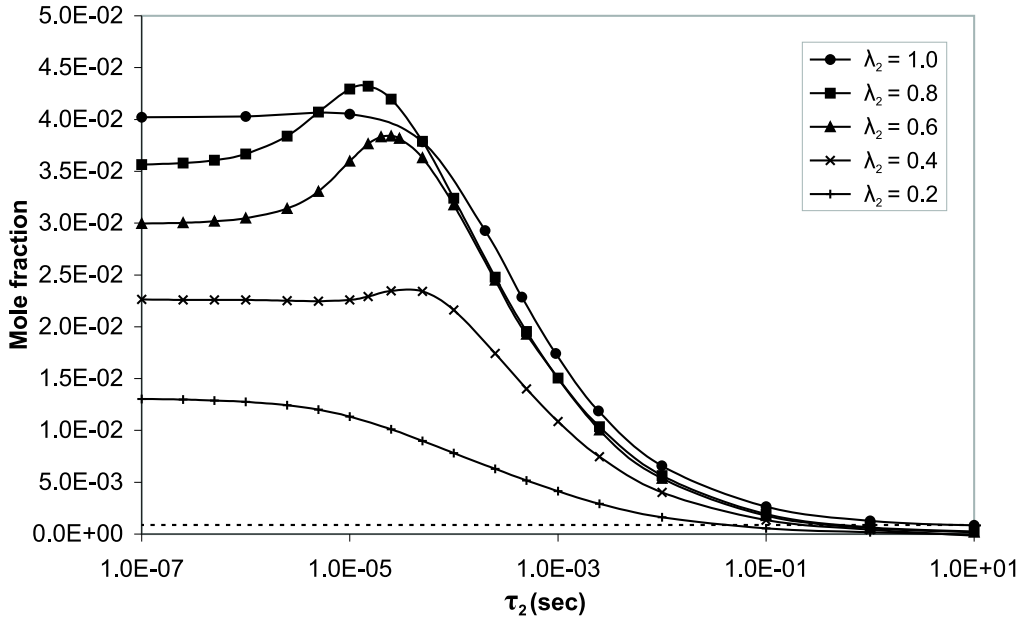

Figure 3.6 : Summed mole fractions of H·, O·, and OH· as a function of the nominal residence time as calculated by PSR2 at various λ_2 for a 4.2 MJ/Nm^3 $CH_4/H_2/N_2$-mixture having a *FHC* of 39.0 vol.%. Dotted line shows cut-off limit.

From figure 3.4 it shows that at FHC = 0 vol.% product gas addition quickly reduces the radical level present after PSR1, irrespective of the value of λ_2. The maximum radical residence time till cut-off varies between $2{\cdot}10^{-5}$ and $1{\cdot}10^{-4}$ seconds for λ_2 between 0.2 and 0.8. Due to its definition, the maximum radical residence time for λ_2 = 1.0 is equal to 10^1 seconds.

From figure 3.5 it shows that for FHC = 16 vol.% the radical level for λ_2 of 0.2 to 0.6 is also reduced to cut-off in approximately 10^{-4} seconds. For λ_2 = 0.8, however, the initial quick reduction in radical level slows down after 10^{-5} seconds, because of which the maximum radical residence time is increased by two orders of magnitude to approximately 10^{-2} seconds.

From figure 3.6 it shows that for FHC = 39 vol.% the maximum radical residence time for all λ_2 considered varies between $3{\cdot}10^{-2}$ and $1{\cdot}10^{0}$ seconds. The radical level shows to gradually decrease for both λ_2 = 1.0 and λ_2 = 0.2. The radical level for the other air-excess ratios first shows a short increase before decreasing. The increase is strongest for λ_2 = 0.6 and λ_2 = 0.8.

Since the choice of τ_1 might be of influence on the reaction profiles above, the results for FHC = 16 vol.% at λ_2 = 0.8 have been recalculated for varying τ_1. The computed summed mole fractions of H·, O·, and OH· are shown in figure 3.7 as a function of τ_1 over the summed residence time $\tau_1 + \tau_2$. It shows that the radical level is certainly influenced by τ_1, since the free radical profiles vary with varying τ_1. The larger τ_1, the faster the reduction towards cut-off in the second reactor. However, the total radical residence time in the PSR-model remains approximately constant at 10^{-2} seconds. Further, the radical level at $\tau_2 = 1{\cdot}10^{1}$ seconds does not significantly depend on τ_1.

The computations show that the behaviour of the free radicals in the secondary step of the two-step PSR-model is influenced by the fuel composition, the air-excess ratio, and τ_1. Both a rising FHC and a rising λ, cause an increase in the radicals residence time, and ensure a slower reduction of the initial radical-level. Chain branching reactions can be triggered if product gas is added to the reaction products of the first PSR. However, if λ_2 becomes too small, chain breaking reactions prevail, probably either due to dilution or temperature-drop. The critical λ_2 below which chain breaking reactions prevail is dependent on FHC and on τ_1. Both a rising FHC, and a decreasing τ_1 stimulate chain branching reactions in the secondary reactor.

3.2.4 Evaluation of results

To evaluate the computational results obtained with the PSR-model, they are compared to experimental data obtained by Houben [39]. Since the experimental data is limited to the concentrations of major species after the partial combustion process, the computed concentrations of CH_4, H_2, CO, CO_2, and O_2 at $\tau_2 = 1{\cdot}10^{1}$ seconds are

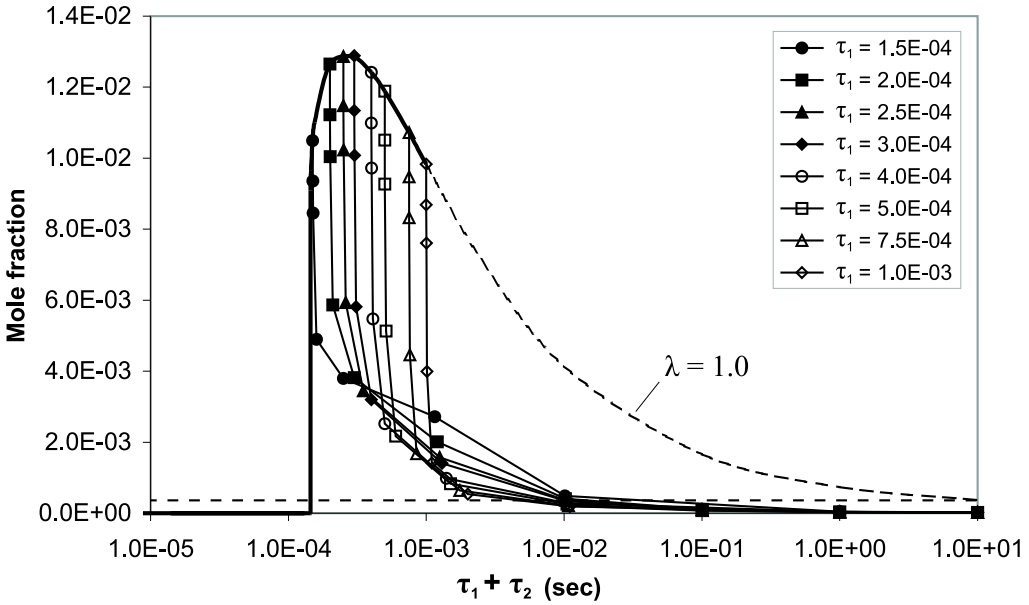

Figure 3.7 : Summed mole fractions of H·, O·, and OH· as calculated by the PSR-model as a function of τ_1 over the summed residence time $\tau_1 + \tau_2$, for oxidation at $\lambda_2 = 0.8$ of a 4.2 MJ/Nm^3 $CH_4/H_2/N_2$-mixture having a *FHC* of 16.0 vol.%. Horizontal dotted line shows cut-off limit.

considered. Further, to determine the value and time-dependency of the computational and experimental results, both are compared to their equilibrium concentrations. These equilibria are calculated by another program, and are unique since there only exists one equilibrium for a given mixture.

In the experiments gas chromatography is used to measure the concentrations of several major gases after a partial combustion process as a function of the fuel hydrogen content and the process' air-excess ratio. The micro-scale swirl-burner shown in figure 1.1 and a glass bell were used. The glass bell was necessary to control the oxidation level of the partial combustion process. However, contrary to the reason of the glass bell, a secondary air-stream (~ 1%) under the glass bell was used to prevent flow recirculations at the swirl-burner rim. Since the gas concentrations were measured at the top of the glass bell, they could be influenced by the secondary air stream. The influence should, however, be minor since the amount of secondary air only represents an increase in air-excess ratio of 0.02 to 0.03. Thus, the experimental data as a function of the air-excess ratio and of the fuel hydrogen content are assumed reliable, although the stated air-excess ratios were probably slightly higher in reality.

Two-step PSR-model versus experiments

The major gas concentrations as computed by the PSR-model at $\tau_2 = 1{\cdot}10^1$ seconds and as measured in the experiments by Houben, are shown as a function of FHC for an air-excess ratio of 0.2 in figure 3.8, and as a function of air-excess ratio for a FHC of 32 vol.% in figure 3.9.

Figure 3.8 shows that the PSR-model and the experiments yield similar trending in the gas concentrations as a function of FHC for an air-excess ratio of 0.2, although differences appear in the absolute concentrations. At very low FHC, the CH_4 concentration computed by the PSR-model is considerably over-predicted, and the H_2 and CO concentrations are considerably under-predicted. At very high FHC the H_2 concentration is somewhat under-predicted. In between, the differences vary linearly with FHC.

Figure 3.9 shows that the computed and experimental gas concentrations for a FHC of 32.0 vol.% show similar trending as a function of λ. Again differences appear in the absolute gas concentrations. At low air-excess ratio the CH_4 concentration is slightly over-predicted, and the CO_2 and H_2 concentrations are respectively slightly and considerably under-predicted. For rising air-excess ratio the concentrations of CH_4 and CO_2 are continuously better predicted, while the under-prediction of H_2 becomes worse, and CO becomes slightly over-predicted.

Shortly, it shows that at low air-excess ratio the oxidation of methane is under-predicted by the computational model, while the oxidation of hydrogen is over-predicted. The consequence is that at low FHC the concentrations of the methane oxidation products (H_2, CO, CO_2) are under-predicted, and the concentrations of reactant (CH_4, O_2) are over-predicted. At high FHC, the only result is that the H_2 concentration is under-predicted. Since the differences at low FHC are considerably larger than at high FHC, it can be concluded that the under-prediction of methane oxidation results in larger deviations from the experiments than the over-prediction of hydrogen oxidation.

At high fuel hydrogen content, the oxidation reactions in the computational model show to increase in strength with the air-excess ratio. This is likely a consequence of the increasing oxygen concentrations. Oxidation of methane becomes correctly predicted, while oxidation of hydrogen becomes even more over-predicted.

A consequence of the above mentioned results is that the released amount of free radicals is probably not correctly predicted. Since methane oxidation is under-predicted, and since methane oxidation seems to have a strong inhibiting effect on the radical level, the predicted radical levels at low FHC are probably lower in reality. Similarly, since hydrogen conversion is over-predicted, and since hydrogen oxidation is a strong source of free radicals, the predicted radical levels at high FHC are

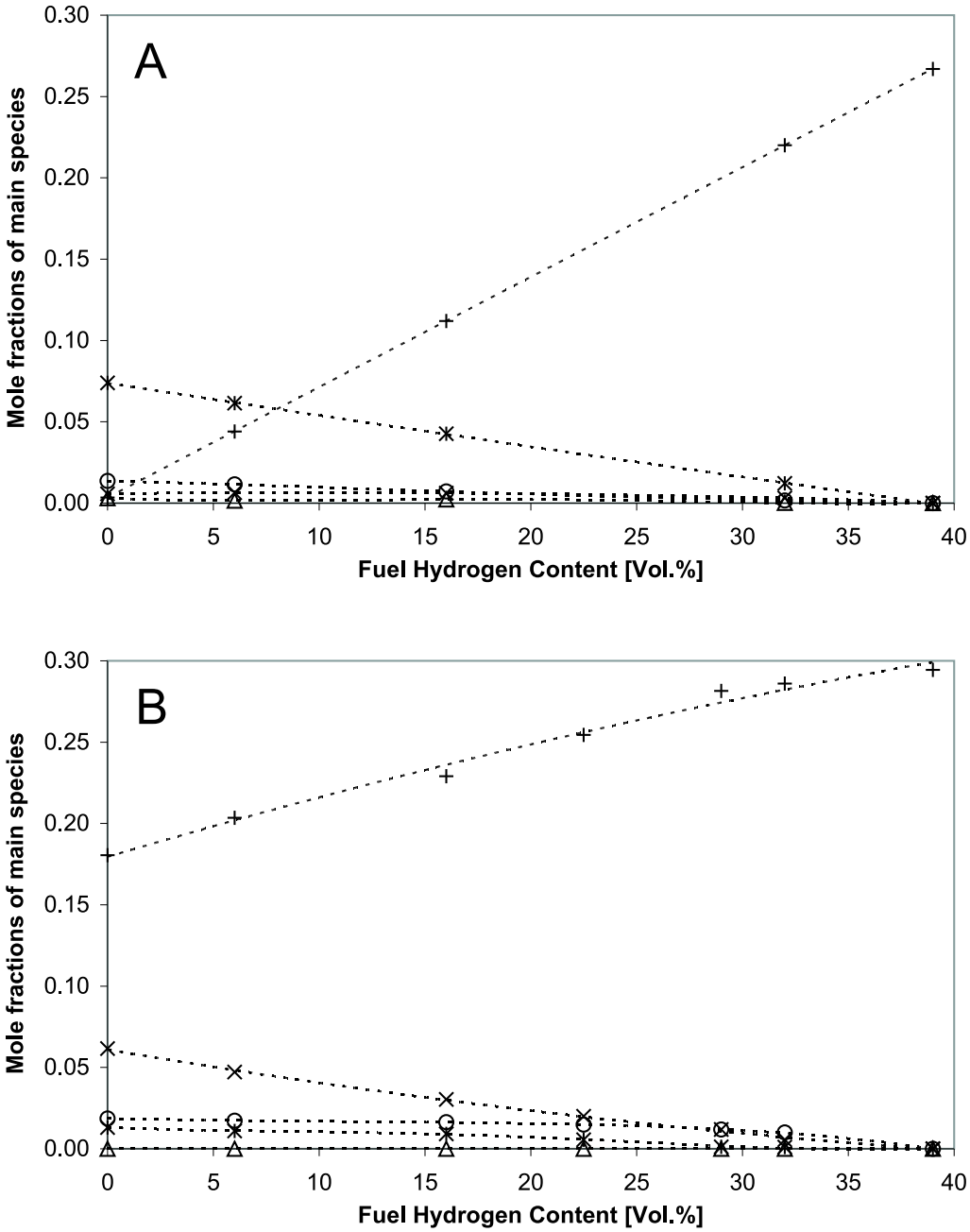

Figure 3.8 : Normalized equilibrium concentrations as a function of fuel hydrogen content after partial combustion of a 4.2 MJ/Nm^3 $CH_4/H_2/N_2$-mixture at an air-excess ratio of 0.2, as (A) computed by the two-step PSR model and (B) experimentally determined by Houben [39].
$*$=[CH_4], $+$=[H_2], $\times$=[CO], O=[CO_2], Δ=[O_2]

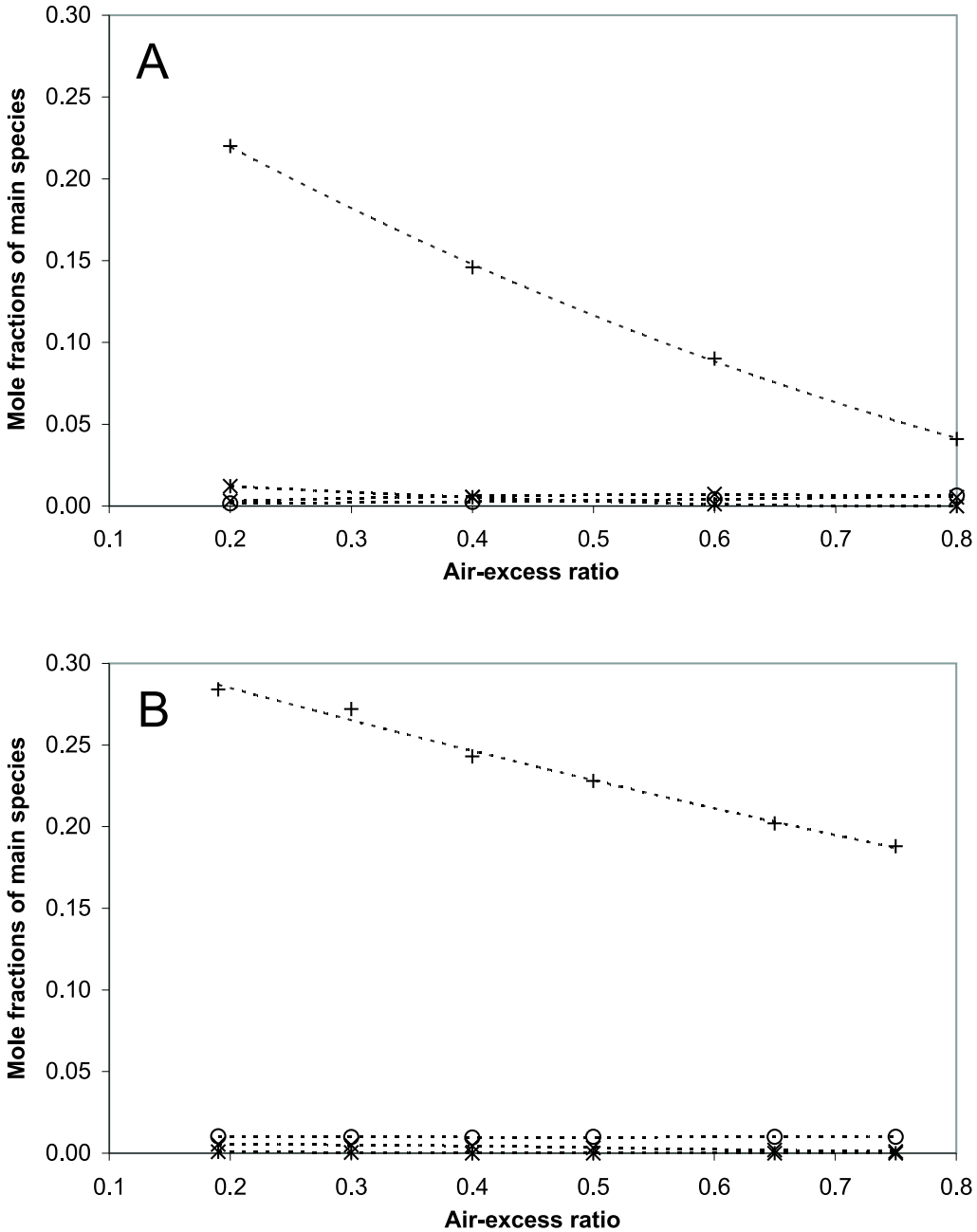

Figure 3.9 : Normalized equilibrium concentrations as a function of air-excess ratio after partial combustion of a 4.2 MJ/Nm^3 $CH_4/H_2/N_2$-mixture with a fuel hydrogen content of 32.0 vol.%, as (A) computed by the two-step PSR model and (B) experimentally determined by Houben [39].
$*$=[CH_4], +=[H_2], $\times$=[CO], O=[CO_2]

probably also lower in reality. However, it is still expected that FHC has a positive effect on the release of free radicals in the partial combustion process. The benefit of the air-excess ratio on the level of free radicals is probably also lower in reality, since hydrogen oxidation becomes more and more over-predicted with increasing air-excess ratio.

Two-step PSR-model versus equilibrium calculations

To value the computed PSR-results and study their time-dependency, they are compared to equilibrium concentrations calculated with the Chemkin-code Equil [53]. Equil is a Fortran program that computes the chemical equilibrium state of an ideal gas or solution mixture. For similarity reasons, the thermodynamic data-base of the chemical reaction mechanism GRI-Mech 3.0 [76] is used. The input concentrations specified are equal to the summed product gas and air input concentrations of the two-step PSR model. The input temperature is again taken 473 K. The calculated equilibrium concentrations as a function of FHC and λ are shown in figures 3.10 and 3.11 respectively.

Comparing figures 3.10 and 3.8A shows that the PSR-results closely resemble the equilibrium results at high FHC, while increasing differences appear with decreasing FHC. The differences are formed by over-prediction of CH_4, under-prediction of H_2, under-prediction of CO, and slight under-prediction of CO_2 by the PSR-model. These differences are similar to the differences found between the PSR-results and the experiments, which have already been attributed to the under-prediction of CH_4 oxidation in the PSR-model.

Since both the PSR-model and the Equil calculations should eventually lead to the same equilibrium results, it shows that at $\tau_2 = 1{\cdot}10^1$ seconds not necessarily an equilibrium situation is reached in the PSR-model. The approximation of equilibrium by the PSR-results at $\tau_2 = 1{\cdot}10^1$ seconds is indicated by the reactor temperatures T_{Equil} (as calculated by Equil) and T_{PSR} (as calculated by the PSR-model). Table 3.1 shows that these reactor temperatures are similar at high FHC, while T_{PSR} becomes increasingly over-predicted for decreasing FHC. This means that the PSR-results increasingly better approximate equilibrium with increasing FHC. This is explained by the relatively low methane oxidation rates compared to the hydrogen oxidation rates, because of which at low FHC longer residence time are necessary before equilibrium is reached. The contradictory result that T_{PSR} is over-predicted while methane oxidation is under-predicted can, however, not be explained.

Comparing figures 3.11 and 3.9-A shows that the PSR-results as a function of λ closely resemble the equilibrium results, although there is a slight under-prediction of methane oxidation at low λ. Apparently, the methane oxidation rates are increased by increasing air-excess ratio, as the under-prediction diminishes for in-

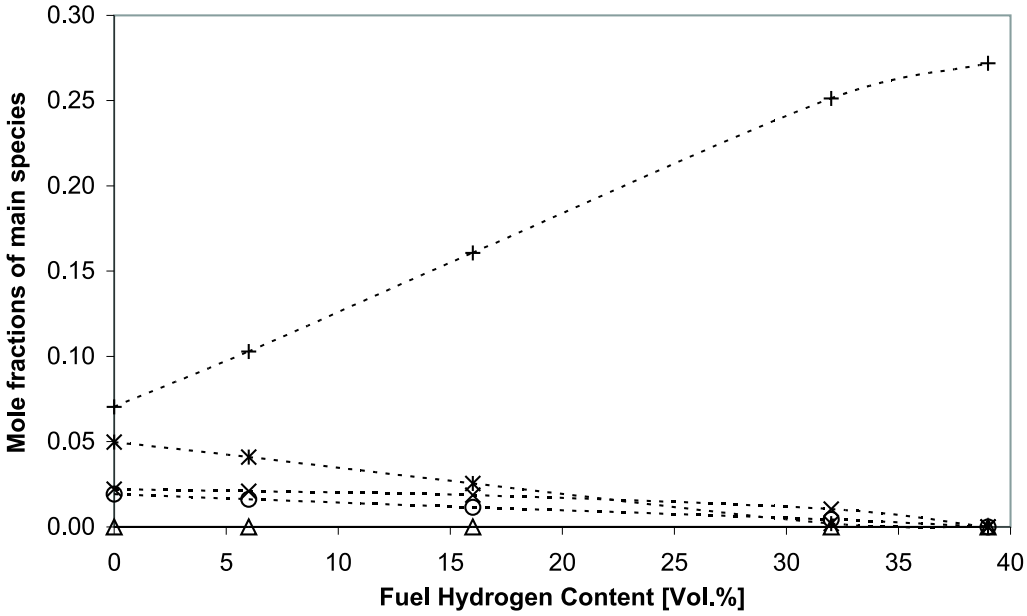

Figure 3.10 : Normalized equilibrium concentrations as a function of fuel hydrogen content after partial combustion of a 4.2 MJ/Nm^3 $CH_4/H_2/N_2$-mixture at an air-excess ratio of 0.2 as calculated by Equil.
$*$=[CH_4], +=[H_2], $\times$=[CO], O=[CO_2], Δ=[O_2]

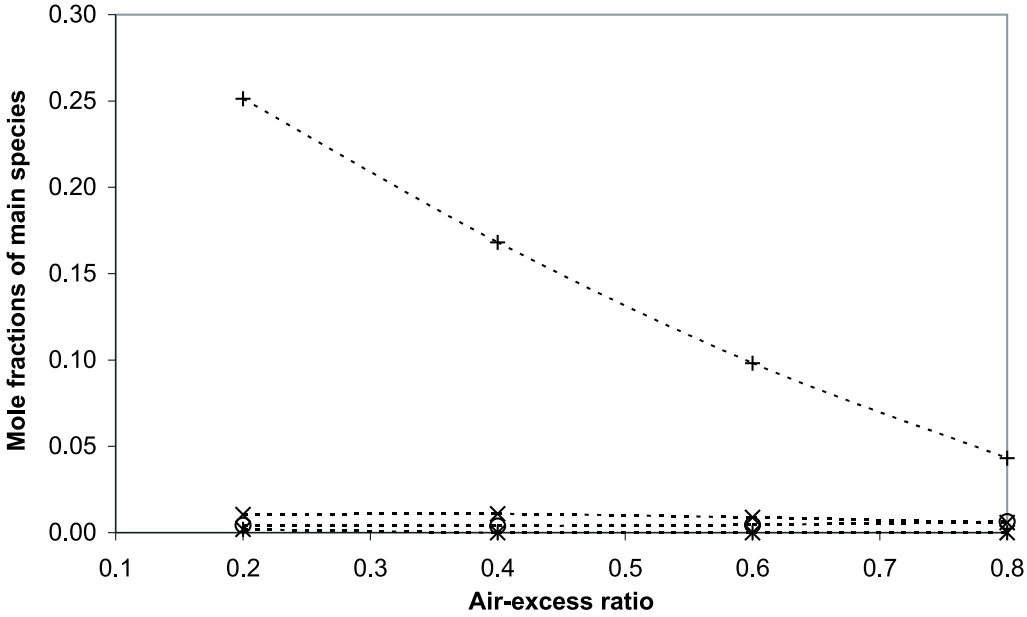

Figure 3.11 : Normalized equilibrium concentrations as a function of air-excess ratio after partial combustion of a 4.2 MJ/Nm^3 $CH_4/H_2/N_2$-mixture with a fuel hydrogen content of 32.0 vol.% as calculated by Equil.
$*$=[CH_4], +=[H_2], $\times$=[CO], O=[CO_2]

Table 3.1 : Reactor temperatures T_{Equil} as calculated by Equil, T_{PSR} as computed by the two-step PSR-model, and T_{Exp} as measured in experiments by Houben [39] as a function of FHC at an air-excess ratio of 0.2.

FHC [vol.%]	0	6	16	32	39
T_{Equil} [K]	778	798	830	909	1005
T_{PSR} [K]	862	888	918	959	1003
T_{Exp} [K]	1033	1036	1038	1045	1050

creasing λ. This is supported by the reactor temperatures shown in table 3.2, which show equal T_{PSR} and T_{Equil} at high λ, but over-predicted T_{PSR} at low λ. Again, the PSR-reactor temperature is over-predicted, while the methane oxidation is under-predicted.

Table 3.2 : Reactor temperatures T_{Equil} as calculated by Equil, T_{PSR} as computed by the two-step PSR-model, and T_{Exp} as measured in experiments by Houben [39] as a function of λ at a FHC of 32 vol.%.

λ	0.2	0.4	0.6	0.8
T_{Equil} [K]	909	1276	1557	1771
T_{PSR} [K]	959	1300	1560	1767
T_{Exp} [K]	1045	1057	1070	1083

Experiments versus equilibrium calculations

From figures 3.8 to 3.11, it can also be concluded that the experimental results differ from the equilibrium results. As these differences can give insight into the reliability of the experimental results, the experimental results are compared to the equilibrium calculations as well.

Comparing figures 3.8B and 3.10 shows that the experimental results differ from the equilibrium results by over-oxidation of methane and under-oxidation of hydrogen. Figures 3.9B and 3.11 show that the measured under-oxidation of hydrogen becomes even stronger with increasing λ.

In tables 3.1 and 3.2, also the measured process temperature T_{Exp} of partial combustion is listed as a function of FHC and λ. The T_{Exp} are measured by Houben [39], this time at a position 120 mm downstream of the swirl-burner top. Although the temperatures were measured at a position different than the gas-measurement sample-point, they are still considered reliable process temperatures. The tables indicate that the experimental temperatures at $\lambda = 0.2$ are all higher than T_{Equil}. The

difference between both temperatures decreases as FHC increases. The fact that both an over-oxidation of methane and an under-oxidation of hydrogen give a process temperature higher than the equilibrium temperature cannot be explained. For increasing λ, the measured temperatures become lower than T_{Equil}, with differences increasing with increasing λ. A slight under-oxidation of hydrogen at low λ gives experimental temperatures higher than equilibrium, while over-oxidation of hydrogen at high λ gives experimental temperatures lower than equilibrium. Again this cannot be explained.

It shows that the measured gas compositions and temperatures after partial combustion in the swirl-burner differ from their equilibrium results. The over-oxidation of methane cannot be explained. The under-oxidation of hydrogen might be explained by the measured reactions not yet having reached equilibrium. This is, however, in contrast with the PSR-results, which indicate that hydrogen oxidation reaches equilibrium before methane oxidation. This indicates that the equilibrium calculations do probably not hold for the experimental situation. Either, the reaction mechanism used in the calculations does not correctly describe the partial combustion reactions, or the gas compositions and temperatures are not measured correctly, or the situation in the swirl-burner differed from the given input in the equilibrium calculations.

3.2.5 Discussion kinetics of free radicals

The computed results show a clear dependence of the radical concentrations and the radical residence times on the fuel hydrogen content and air-excess ratio. An increasing FHC reduces the ignition delay time, increases the radical level, and increases the radicals residence time. An increasing air-excess ratio mainly leads to increased radical residence times.

The PSR-model is constructed based on assumptions for λ_1 and τ_1, and on a decoupling between the chemical and transport processes. The assumption on τ_1 has been shown to influence the free radical levels, but does not strongly influence their maximum residence times.

The assumption on λ_1 probably influences the radical levels by creation of different amount of radicals in the first reactor. It is therefore likely that the amount of free radicals at τ_2=0 seconds changes for changing λ_1, due to which probably also the residence times change. Whether a higher or a lower λ_1 is better for free radical production should be studied.

The decoupling between the chemical and transport processes gave insight into the chemical time-scales of partial combustion. It, however, shows that these time-scales can be of the same order of magnitude as the physical time-scales, depending on the fuel hydrogen content. At low FHC, the radicals' residence times are shorter

than the physical time-scale of the visible flame of $1.5 \cdot 10^{-3}$ seconds. At high FHC, the radicals' residence times exceed the physical time-scales. In between, at realistic FHC for real product gas, the chemical and physical mixing time-scales are of the same order of magnitude, due to which the two processes may not be decoupled. However, chemical time-scales exceeding those of transport for increasing FHC, indicates for increasing FHC it becomes more and more likely that free radicals produced during the initial product gas combustion come into contact with the rest product gas. Since contact between fresh product gas and free radicals hypothetically causes tar cracking, an increasing FHC probably stimulates tar cracking.

3.3 Kinetics of aromatics

Another model is used to study the dependency of tar conversion on the oxidation settings. The model describes the kinetics of relatively large hydrocarbons as a function of the oxidation regime and mixture conditions. Following the experiments by Houben [40], the kinetics of a naphthalene containing gas mixture are considered. In the experiments, a small amount of naphthalene was added to the fuel of the setup described in section 3.2.4. The tar conversion was measured by gas chromatography, which gave the results shown in figures 1.3 and 1.4. Using the model the influence of the air-excess ratio and fuel hydrogen content on the fate of carbon-atoms is studied. The modeling results are compared to the experimental results.

3.3.1 Method

Recently, Evlampiev [21] developed the C-Mech code, which greatly reduces calculation times necessary for large chemical reaction mechanisms. To improve computational performance for large chemical reaction mechanism, the input data, originally formatted in CHEMKIN-III standards, are translated into C++ inline source code on the preprocessing stage [22]. This development enabled the use of complex reaction mechanisms for the study of chemical kinetics of aromatics.

The reaction mechanism used to study the chemical kinetics of naphthalene during product gas combustion, is the Richter mechanism [72]. The Richter mechanism describes formation and consumption of PAH and soot for oxidative low-pressure applications. The kinetic mechanism consists of 295 species, 1102 conventional gas phase, and 5552 reactions describing particle growth. Because the number of species of similar mass and the number of structural isomers increase quickly with molecular mass, classes (BIN's) of very large PAH and of particles covering certain mass ranges have been defined. A consequence of using this mechanism is that all results can only be considered indicative, since the mechanism has only

been partly validated in oxidative environments, and has not been validated in non-oxidative environments.

To calculate the chemical kinetics, the C-Mech code is applied to a single-step Rapid Compression Machine (RCM) function held at constant pressure, which computes homogeneous adiabatic gas phase chemical processes for the input specified. An RCM function at constant pressure basically represents a homogeneous reactor, and is used because at the time being it is the only reactor on which C-Mech has been proven to work well.

The input of the RCM consists of a methane/hydrogen/nitrogen-mixture with a certain lower heating value, to which a small volume percentage of naphthalene ($C_{10}H_8$) and an amount of oxidizing air are added (see figure 3.12). It is chosen not to count the naphthalene to the LHV to enable better comparison of the gas properties. Again carbon monoxide is omitted as a combustible component in the model gas, which is for the same reasons as in the previous section.

The behaviour of the C-atoms in the reactor is studied as a function of the air-excess ratio λ, the naphthalene concentration, the FHC, the LHV, and the initial reactor temperature. This is done by inducing small variations on a chosen standard RCM-input. The standard RCM-input has a FHC of 20 vol.%, a LHV of 5 MJ/Nm^3, an added naphthalene concentration of 1 vol.%, and an air-excess ratio of 0.4. This input setting is chosen because: (1) the FHC is in the middle of its range, and the tar cracking results as a function of the air-excess ratio shown in figure 1.3 are given at an approximately equal FHC, (2) product gas from a biomass gasifier often has a LHV of approximately 5 MJ/Nm^3, (3) 1 vol.% naphthalene approximately equals 50 g/Nm^3 in the applied gas, which is in the middle of the range of tar levels found in product gas from updraft biomass gasifiers [64], and (4) an air-excess ratio of 0.4 is the lowest ratio for which the RCM data-log is still manageable. Because a RCM function is used, a relatively high initial reactor temperature has to be chosen to obtain ignition. Therefore the input temperature is set to 2000 K. Different scenarios with different species concentrations or initial reactor temperature have been computed, of which the most typical results are given below.

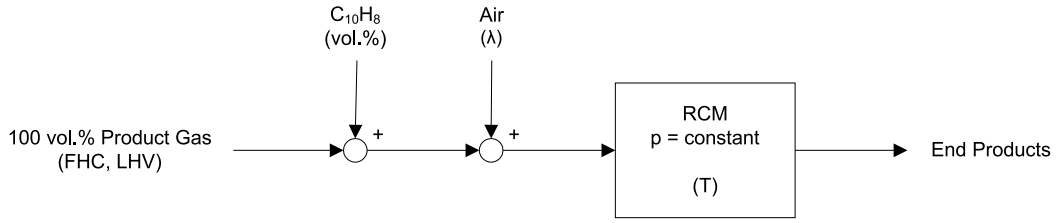

Figure 3.12 : One-step RCM model for calculation of kinetics of aromatics as a function of FHC, LHV, $C_{10}H_8$-concentration, λ, and inlet temperature T.

3.3.2 Cracking vs polymerization of aromatics

The C-Mech calculations result in a list of mole fractions of all 295 species as a function of residence time in the reactor. To study the behaviour of the C-atoms, the obtained mole fractions are converted into C-atom fractions per cluster of species. The clusters considered in this analysis in order of increasing amount of C-atoms are: C1-species, sum of C2-to-C9-species, C10-species, sum of C11-to-C30-species, sum of BIN1 (C24) to BIN19 (C6483968) species, and BIN20-species (C12972032). The C1-cluster contains all species having one C-atom, etc. The consequence is that, compared to naphthalene, all cracking products are contained by the C1 and C2-to-C9-clusters, while the polymerization products are contained by the C11-to-C30 and BIN-clusters. The BIN20-species are considered soot, while the BIN1-to-BIN19-species are considered soot-precursors. The C1, C10 and BIN20-species are singly clustered because they contain the most important input (CH_4 and $C_{10}H_8$) and reaction products (CO, CO_2 and soot).

Although BIN1-species contain 24 C-atoms and could thus be clustered among the C11-to-C30-species, they are clustered among the BIN-species because of their chemical reactions in the Richter mechanism. While the reactions described for the C1-to-C30-species are all reversible, the reactions described for all BIN-species are irreversible. Since only polymerization and oxidation reactions are described for the BIN-species, their amount can only be reduced by oxidation reactions, thus not by reversed polymerization reactions.

High air-excess ratio

For comparison reasons, the results for oxidation of the standard gas setting at an air-excess ratio of 1.0 are discussed first. As shows from figure 3.13, there seem to exist three subsequent reaction regimes in the reactor. After $7{\cdot}10^{-6}$ seconds oxidation reactions start, which consume a lot of C10-species, produce a lot of light (C1 to C9) and heavy (C11 to BIN19) species, and rapidly increase the reactor temperature. The first regime is followed by a stable regime in which the temperature slowly rises, and the C-atom fractions of all species are relatively constant. The second regime is followed by a third regime, in which the reactor temperature becomes approximately constant, and the C-atom fractions of most C-species drop, except for the C1-species. The C1-species thus become the main equilibrium-species.

Figure 3.13 clearly shows the C-atom fractions per subgroup as a function of time, but does not show the main conversion reactions. Therefore the rates of change of the C-atom fractions per subgroup are shown in figure 3.14. A positive or negative rate of change means that the C-atom fraction of the respective subgroup respectively increases or decreases. The graph shows that the reactions start by reduction of the C10-subgroup into C2-to-C9-species and slightly into C1-species. Shortly after, the C1-fraction slightly decreases followed by a strong C1 production. During

the C1 production peak, the rate of change of C2-to-C9, C10, and C11-to-C30 are all negative, which means they are converted into C1-species.

It can be concluded that oxidation of the standard gas at a high air-excess ratio leads to full oxidation or cracking of naphthalene towards C1-species, although polymerization reactions also create some higher hydrocarbons. The first reactions in the reactor are conversion of C10-species into C2-to-C9 species, probably by oxidation as a slight C1 (CO) production can be noticed. The negative C1-coefficient just after the start of the process is probably caused by polymerization reactions of methane. After a while a lot of C1-species are produced, which indicates that oxidation reactions take place. During the oxidation process initially some C11-to-C30 and BIN1-to-BIN19-species are produced. Later in the oxidation process all higher hydrocarbons are converted into small species by oxidation. The rates of change of the conversion process during the third specified regime are negligible, which indicates that it is a slow process.

Low air-excess ratio

Varying the air-excess ratio to 0.8 and 0.6 does not show to cause any significant differences compared to the result at λ = 1.0. However, oxidation of the standard gas setting at an air-excess ratio of 0.4 or 0.2 does show differences compared to the results at high air-excess ratio. The results for oxidation of the standard setting at a λ of 0.4 are shown in figure 3.15. There still seems to be a primary oxidation regime in which the temperature rapidly rises and C10 species are consumed under formation of both lighter and heavier species. After most oxygen has been depleted at approximately $2{\cdot}10^{-5}$ seconds, most C-atoms are transferred to C1-species and some to BIN1-to-BIN19-species. The temperature only slightly varies after the primary oxidation. For increasing residence time the smaller BIN-species gradually accumulate into BIN20-species, which is a main end-product next to C1-species.

The rates of change of the reactions are shown in figure 3.16. Similar behaviour is found as for oxidation at a λ of 1.0, except for the absolute and relative peak-values of rate of change. Again the reactions start by conversion of C10-species into C2-to-C9-species. Shortly after, a slight reduction of C1-species and production of C11-to-BIN19 species follows. As soon as oxidation reactions start, the rate of change of C1-species becomes positive, at the expense of C2-to-C9 and C11-to-C30 species. Later in the process (during the third regime) the levels of C1 and BIN1-to-BIN19 slowly decrease under production of BIN20-species.

The primary oxidation of the gas mixture seems to occur relatively similar both for λ = 1.0 and λ = 0.4. For both situations there is a strong drive towards C1-species by oxidation. However, for low air-excess ratios there is also a slight irreversible

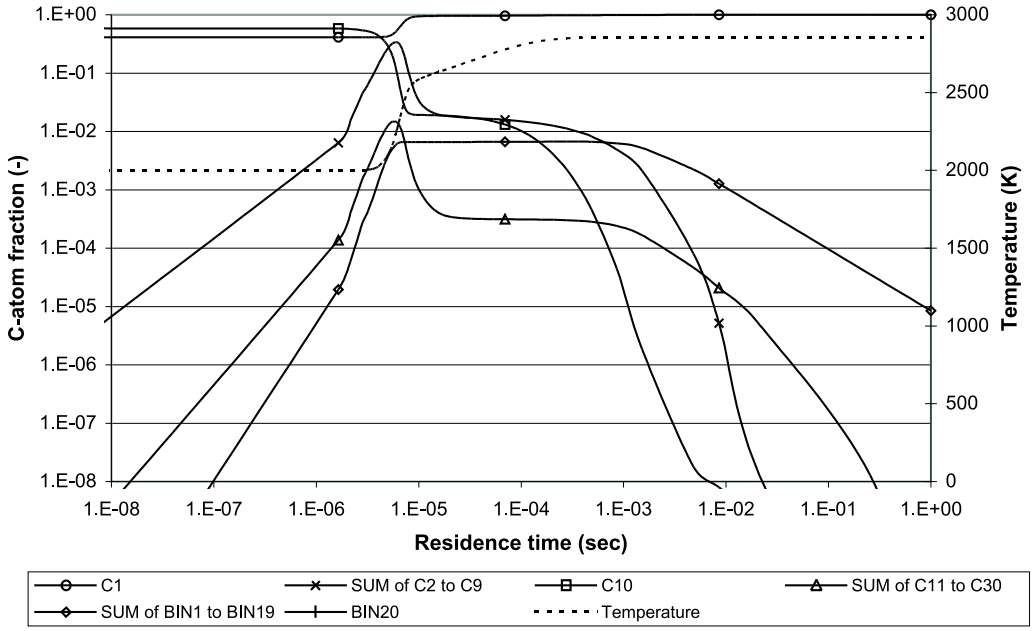

Figure 3.13 : C-atom fractions as a function of residence time in a perfectly stirred reactor as calculated by C-Mech using the Richter mechanism for 20 vol.% hydrogen, LHV of 5 MJ/Nm^3, 1 vol.% naphthalene, air-excess ratio of 1.0, and an initial temperature of 2000 K. The C-atom fractions of the BIN20-cluster are too low to be plotted.

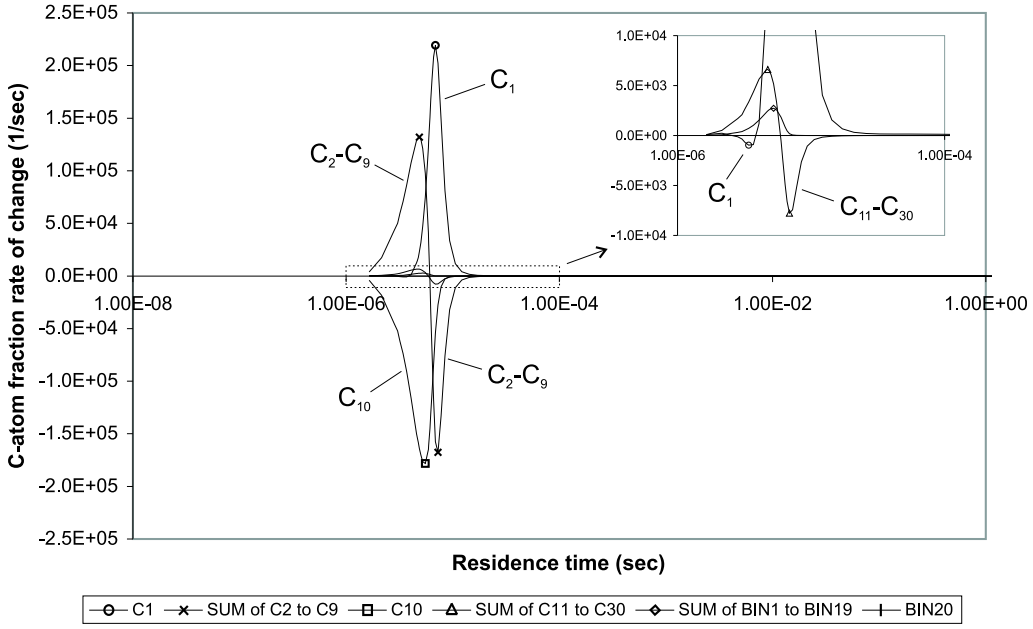

Figure 3.14 : Rate of change of C-atom fractions as a function of residence time in a perfectly stirred reactor as calculated by C-Mech using the Richter mechanism for 20 vol.% hydrogen, LHV of 5 MJ/Nm^3, 1 vol.% naphthalene, air-excess ratio of 1.0, and an initial temperature of 2000 K. The C-atom fraction rate of change of the BIN20-cluster is too low to be plotted.

production of polymerization products, which eventually leads to a substantial soot production. Some differences are a consequence of different reaction rates, shown by lower rates of change for $\lambda = 0.4$. However, most differences are generated during the relatively slow secondary and tertiary reaction regimes. This indicates that the slow conversion reactions after the initial oxidation have a considerable influence on the outcome of the reactions. Furthermore, the conversion reactions can be influenced by changing the initial oxidation conditions.

Fuel hydrogen content

The influence of the fuel hydrogen content is tested by oxidizing gas with 0 vol.% hydrogen (pure $CH_4/C_{10}H_8/N_2$-mixture) and with 46.3 vol.% hydrogen (pure $H_2/C_{10}H_8/N_2$-mixture), while maintaining the standard LHV and naphthalene concentration.

In figures 3.17 and 3.18 the results for oxidation at $\lambda = 0.4$ are shown. The results at high air-excess ratio are not shown since a changing fuel hydrogen content did not lead to differences, although reactions again tend to have shorter ignition delay times with increasing FHC (just as for the two-step PSR model). It shows that at low air-excess ratio an increasing fuel hydrogen content leads to shorter ignition delay times, less BIN formation, an elongation of the secondary reaction regime, and eventually to less soot formation. The primary oxidation, however, does not seem to have changed substantially. This means, that most differences at maximum residence time are caused during the secondary and tertiary reaction regimes.

The rates of change shown in figures 3.19 and 3.20, show that the reaction rates become higher and the reaction times become shorter with increasing FHC. Further, it shows that for low FHC the C1 and BIN1-to-BIN19-species are slowly converted into BIN20-species during the secondary and tertiary reaction regime, while in the same regime for high FHC the BIN1-to-BIN19-species are converted into C1-species.

It shows that hydrogen has a driving effect towards C1-species and increases the rate of reactions. The reactions that do take place do not seem to be altered by a varying hydrogen concentration since the relative peak positions remain the same. However, the maxima of rate of change for the various subgroups do change relative to each other. This indicates that the relevance of reactions is shifted. Further, it shows that the slow reactions during the secondary and tertiary reaction regime can be shifted from polymerization/accumulation into cracking/oxidation by increasing the fuel hydrogen content.

Naphthalene content

Adding 2 vol.% naphthalene, instead of 1 vol.%, to the oxidation of the standard gas at an air-excess ratio of 0.4, does not lead to large variations in the results. The results in figure 3.21 show that the soot production is slightly increased compared to the

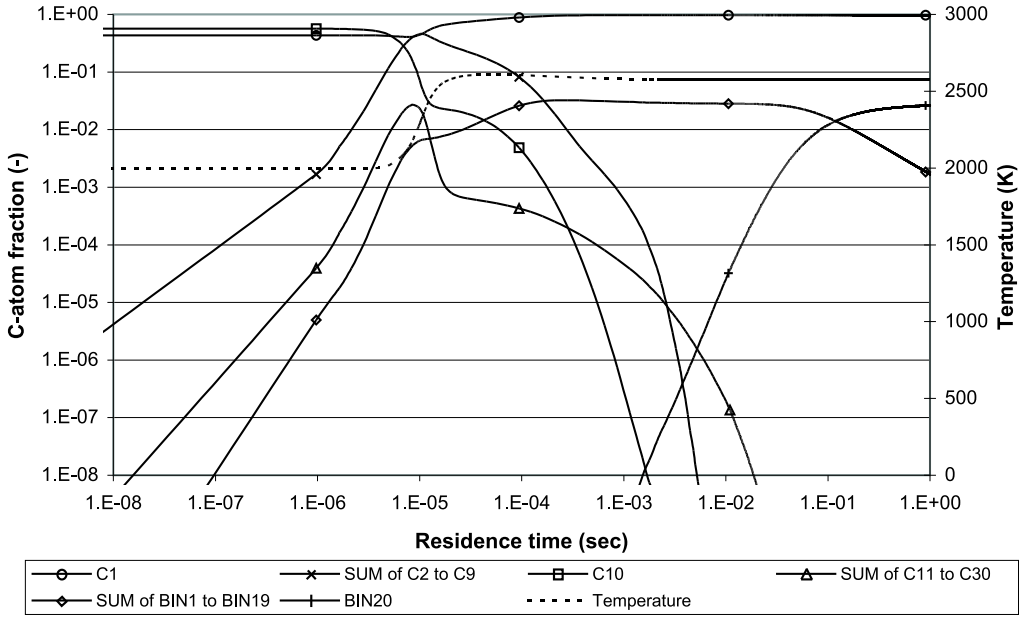

Figure 3.15 : C-atom fractions as a function of residence time in a perfectly stirred reactor as calculated by C-Mech using the Richter mechanism for 20 vol.% hydrogen, LHV of 5 MJ/Nm^3, 1 vol.% naphthalene, air-excess ratio of 0.4, and an initial temperature of 2000 K.

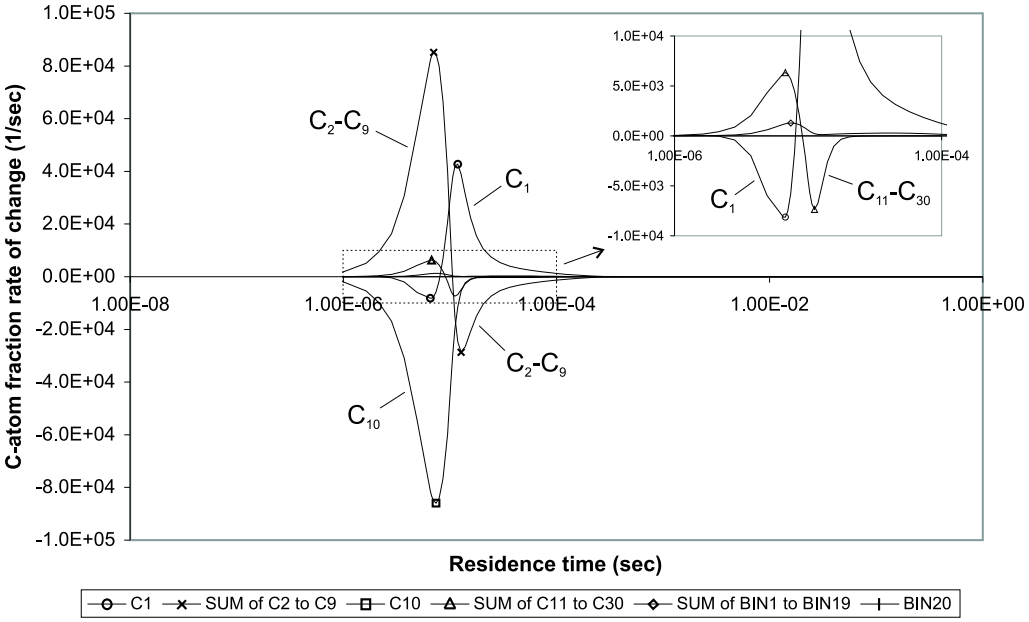

Figure 3.16 : Rate of change of C-atom fractions as a function of residence time in a perfectly stirred reactor as calculated by C-Mech using the Richter mechanism for 20 vol.% hydrogen, LHV of 5 MJ/Nm^3, 1 vol.% naphthalene, air-excess ratio of 0.4, and an initial temperature of 2000 K. The C-atom fraction rate of change of the BIN20-cluster is too low to be plotted.

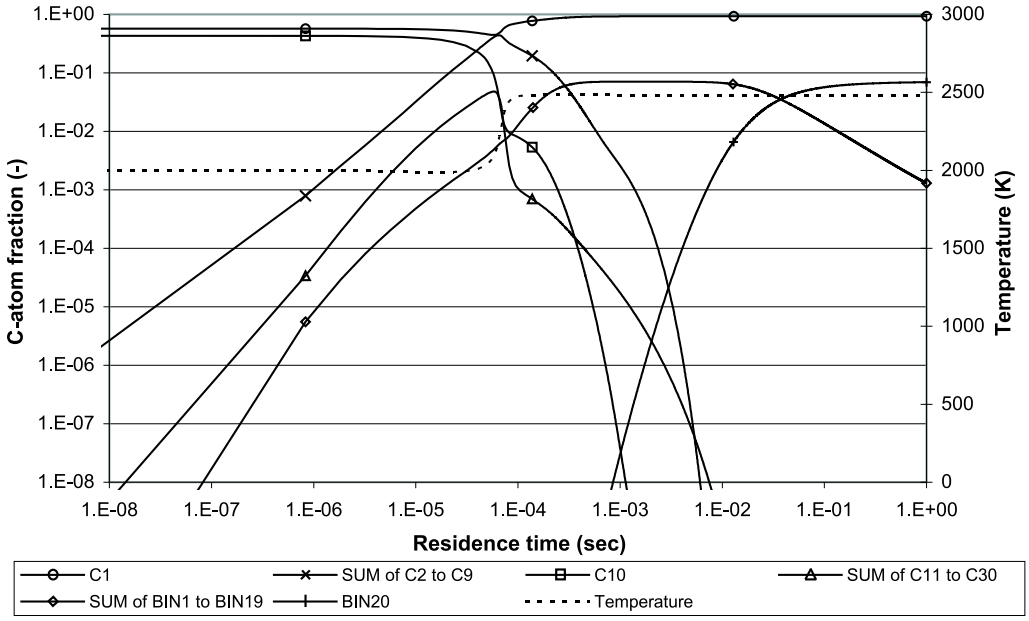

Figure 3.17 : C-atom fractions as a function of residence time in a perfectly stirred reactor as calculated by C-Mech using the Richter mechanism for 0.0 vol.% hydrogen, LHV of 5 MJ/Nm^3, 1 vol.% naphthalene, air-excess ratio of 0.4, and an initial temperature of 2000 K.

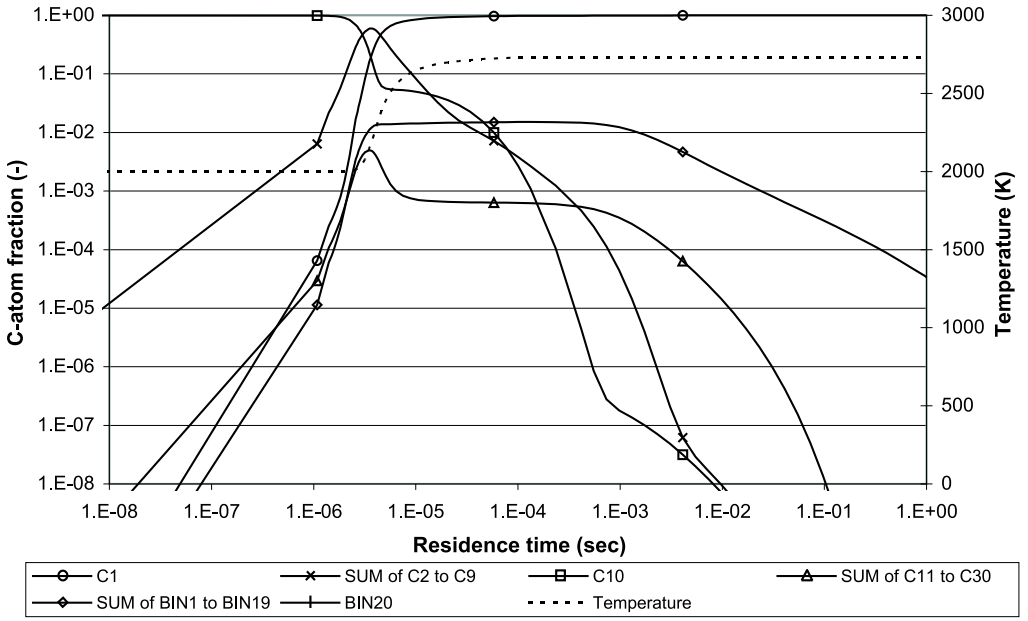

Figure 3.18 : C-atom fractions as a function of residence time in a perfectly stirred reactor as calculated by C-Mech using the Richter mechanism for 46.3 vol.% hydrogen, LHV of 5 MJ/Nm^3, 1 vol.% naphthalene, air-excess ratio of 0.4, and an initial temperature of 2000 K. The C-atom fractions of the BIN20-cluster are too low to be plotted.

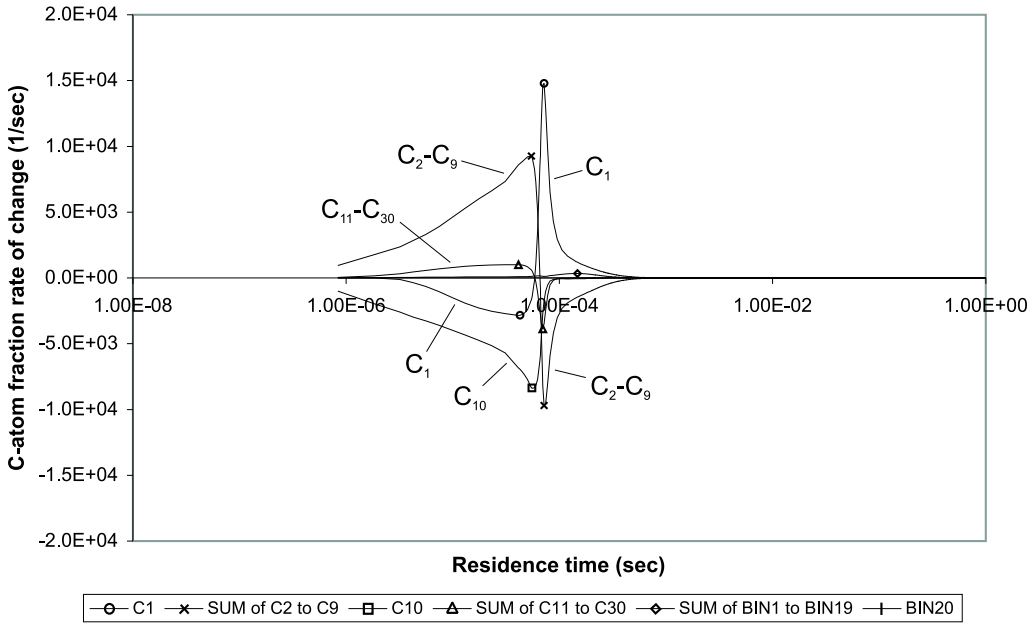

Figure 3.19 : Rate of change of C-atom fractions as a function of residence time in a perfectly stirred reactor as calculated by C-Mech using the Richter mechanism for 0.0 vol.% hydrogen, LHV of 5 MJ/Nm^3, 1 vol.% naphthalene, air-excess ratio of 0.4, and an initial temperature of 2000 K. The C-atom fraction rate of change of the BIN20-cluster is too low to be plotted.

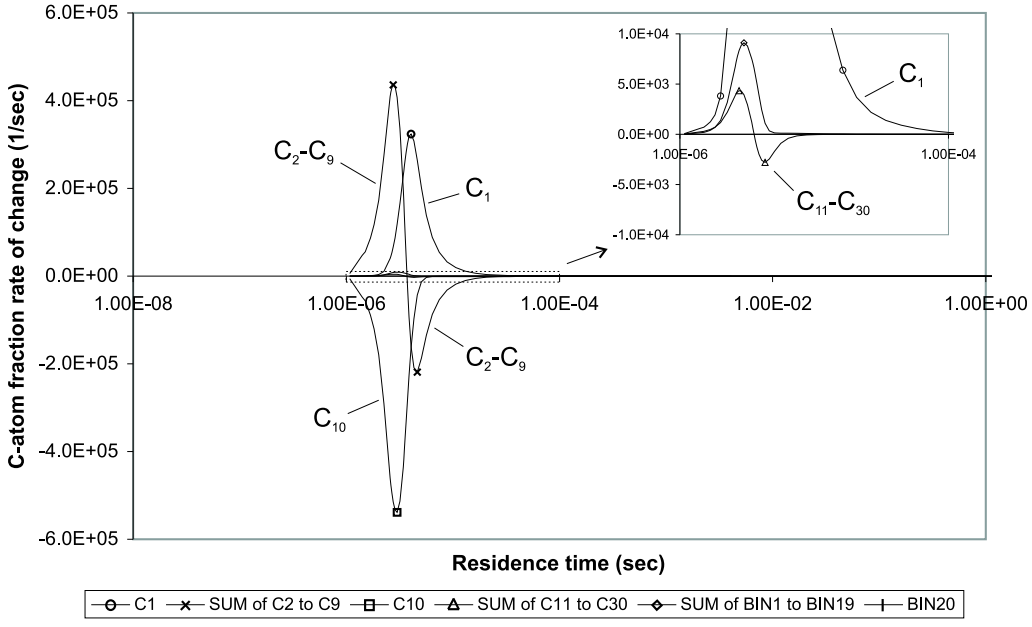

Figure 3.20 : Rate of change of C-atom fractions as a function of residence time in a perfectly stirred reactor as calculated by C-Mech using the Richter mechanism for 46.3 vol.% hydrogen, LHV of 5 MJ/Nm^3, 1 vol.% naphthalene, air-excess ratio of 0.4, and an initial temperature of 2000 K. The C-atom fraction rate of change of the BIN20-cluster is too low to be plotted.

standard situation shown figure 3.15. The reactions in the primary and secondary regime seem rather similar to the results shown in figure 3.15, although the level of BIN1-to-BIN19-species is higher. Although a lot of BIN20-species are created, the final C-atom fraction for the standard gas with 2 vol.% naphthalene is still almost entirely contained by C1-species.

Not shown but worth mentioning, by decreasing the naphthalene level to 0.5 vol.% the formation of soot precursors (BIN1-to-BIN19) is reduced by a factor 10, which results in a soot (BIN20) reduction by a factor 10^4. All other C-atom fractions as a function of residence time are not significantly changed by lowering the naphthalene concentration from 1 to 0.5 vol.%.

It shows that an increasing naphthalene concentration increases polymerization reactions, even though a stoichiometric amount of oxygen is present. The increased polymerization is probably a consequence of the increased presence of PAH building blocks in the form of naphthalene.

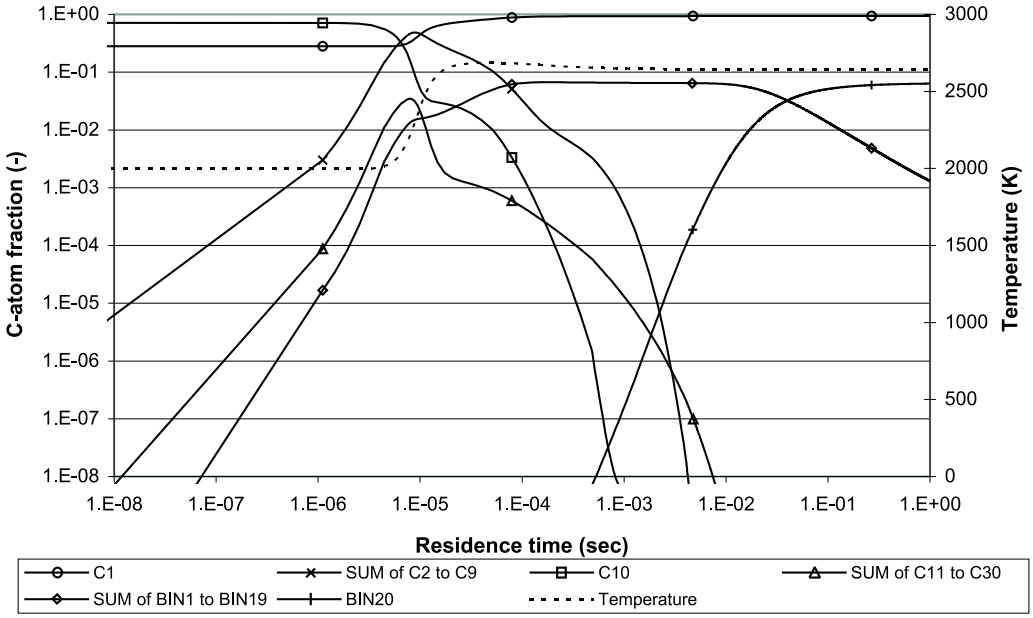

Figure 3.21 : C-atom fractions as a function of residence time in a perfectly stirred reactor as calculated by C-Mech using the Richter mechanism for 20 vol.% hydrogen, LHV of 5 MJ/Nm^3, 2 vol.% naphthalene, air-excess ratio of 0.4, and an initial temperature of 2000 K.

Reactor temperature

Up to now the initial reactor temperature was 2000 K, which was chosen such that the reactions could start easily. By decreasing the initial reactor temperature, the ignition delay times become longer and the final reactor temperatures are reduced.

The C-atom fractions per subgroup do not change significantly. The only striking difference that arises, is that for decreasing reactor temperature the initial C10-conversion increases. Since the absolute C10 rate of change is lower than for the standard temperature setting, it can be concluded that the C10-conversion increases due to increasing reaction duration. The reactor temperature thus mainly influences the reaction rates, but does not seem to influence the reactions taking place.

Lower Heating Value

Increasing the product gas lower heating value from 5 to 10 MJ/Nm^3 at an air-excess ratio of 1.0 does not lead to major differences, although the production of heavy hydrocarbons is slightly reduced. At an air-excess ratio of 0.4, the same LHV increase leads to a strong formation of cracking/oxidation products and a strong reduction in soot formation. This effect is probably a consequence of the relatively low amount of naphthalene compared to the amount of methane and hydrogen. Furthermore, the total fuel hydrogen content increases with increasing LHV as the nitrogen concentration strongly decreases. As already shown before, a higher fuel hydrogen content leads to increased cracking reactions.

3.3.3 Discussion kinetics of aromatics

According to the computations, (partial) combustion of a naphthalene containing $CH_4/H_2/N_2$-mixture gives three subsequent reaction regimes. In a first regime, oxidation reactions create a wide variety of species and strongly increase the reactor temperature. In a second regime, the reactions slow down and the reactor temperature becomes constant. In the third regime reforming reactions take place while the temperature remains constant. Because the reaction rates do not change in the secondary and tertiary reaction regimes, these regimes can be considered as one slow conversion regime. This coincides with the oxidation/conversion mechanism found for partial methane oxidation, as described in section 3.1.

The reactions in the oxidation regime seem to be relatively independent of the input settings, since the results for all calculations gave strongly resembling reaction profiles. Main influence found is that a higher initial $C_{10}H_8/CH_4$-ratio causes a small drive towards heavy species.

The reactions in the conversion regime generally lead to the polymerization and accumulation of small C-species to BIN-species. Depending on the conditions in the reactor, soot formation by polymerization reactions can be inhibited while tar cracking is stimulated. Tar cracking is stimulated by a high air-excess ratio, a high fuel hydrogen content, a high LHV, a low naphthalene concentration, and a high initial reactor temperature, which (except for LHV) are all also tar cracking stimuli found in chapter 2.

In all situations computed, the sum of the C-atom fractions of all C11-to-BIN20-species at $1 \cdot 10^0$ seconds is lower than the initial C-atom fraction of naphthalene. It can therefore be concluded that for each situation tar reduction is predicted. This coincides with the experimental results by Houben [39], who regardlessly of the partial combustion settings always found tar reduction.

Comparison of figures 3.15, 3.17, and 3.18, with figure 1.4, shows agreement between the computational and the experimental naphthalene conversion results as a function of the fuel hydrogen content. Both show an increased naphthalene cracking and decreased soot formation with increasing fuel hydrogen content. However, the computations always predict full naphthalene conversion either into C1-species or into soot(-precursors), while the experiments also show considerable formation of either C6-to-C9 or C11-to-C30-species. This difference can probably be explained by the finite rate of transport processes in the experiments, which prevent the homogeneousness assumed in the computations. Consequently, species concentrations become dependent on the position in the swirl-burner.

Comparison of figures 3.13, and 3.15, with figure 1.3, shows disagreement between the computational and the experimental naphthalene conversion results as a function of the air-excess ratio. The computations predict increased naphthalene cracking with increasing air-excess ratio, while the experiments showed a decreasing naphthalene cracking and increasing soot formation with increasing air-excess ratio. More specifically, according to the experiments the air-excess ratio should, for a gas with an FHC of 22.5 vol.%, be smaller than 0.3 to obtain tar reduction by cracking. Possible reasons for the obtained difference as a function of the air-excess ratio are: 1) there are (yet undisclosed) input settings for the calculations that have a large effect on the results, 2) the one-step RCM-model does not represent the partial combustion process correctly, 3) the used reaction mechanism does not correctly describe the reactions taking place inside the partial-oxidator, or 4) the measurements by Houben [40] are incorrect. Most likely, as has been concluded in chapter 2 as well, the transport processes have an effect on the mixture fractions in the swirl-burner and such on the local air-excess ratio. Therefore, the homogeneous RCM-reactor does not correctly describe the situation in the swirl-burner.

3.4 Conclusions

It is hypothesized that tar cracking by partial product gas combustion happens by a two-step oxidation/conversion mechanism. The free radicals formed during the oxidation reactions hypothetically cause tar cracking by conversion reactions. The hypothesized two-step chemical mechanism is supported by the results computed by the one-step RCM model described in section 3.3. The results predict a two-step chemical process with a clear oxidation regime and a clear conversion regime.

During the oxidation regime, all product gas components (including tar) are converted into a wide variety of species next to a lot of small oxidation products. In the conversion regime, the variety of species created is converted to either cracking or polymerization products depending on the conditions.

Tar cracking by partial combustion in the micro-scale swirl-burner of Houben [39] increases with increasing fuel hydrogen content, as shown in figure 1.4. This coincides with the results of the RCM-model, which predict an increased tar cracking, and a decreased soot formation, with increasing fuel hydrogen content. This result is further supported by the computed results obtained by the two-step PSR model described in section 3.2. The computations show that an increasing fuel hydrogen content increases the amount of free radicals produced during the reactions, and also increases their residence times. The residence times of free radicals at high fuel hydrogen content become so large, that the radicals are likely to come into contact with fresh non-combusting product gas in the swirl-burner. Contact between free radicals and (fresh) tar hypothetically leads to tar cracking. Although the hypothesis is supported, it is not yet proven.

As shown in figure 1.3, tar cracking by partial combustion in the micro-scale swirl-burner of Houben [39] decreases with increasing air-excess ratio. This result cannot be supported by either the two-step PSR-model nor the one-step RCM-model. According to both models, tar cracking should increase with increasing air-excess ratio. This was also concluded from the theoretic analysis in chapter 2. The differences are most likely caused by transport processes that play a role during partial combustion, while they have not been modeled.

Again a high fuel hydrogen content shows beneficial for tar cracking, while the influence of the air-excess ratio remains dubious.

Chapter 4

Experimental gasifier setup

To test tar reduction by partial combustion on real product gas, a test-setup containing a biomass gasifier is required. This chapter focusses on the design and construction of such a test setup. In section 4.1 a basic setup layout is proposed, after which the design of two of its components, a gasifier and a flare are described in sections 4.2 and 4.3. In section 4.4, the results of tests on the operation of the designed setup are described. The design of an up-scaled swirl-burner for testing partial product gas combustion is described in chapter 5.

4.1 Basic setup layout

The test-setup layout is based on a few basic requirements: (1) it should produce product gas, and (2) it should not emit any harmful components. A biomass gasifier is used to produce tar containing product gas. The product gas is fed from the gasifier directly to the up-scaled swirl-burner. The gases leaving the swirl-burner after oxidative treatment, still contain combustible, poisonous and tarry components. Therefore, an end-of-the-line gas cleaning system is necessary. A flare is used to clean the gases by combustion of the harmful components. The cleaned gases are led from the flare to an open exhaust. The basic test-setup then becomes as schematically shown in figure 4.1.

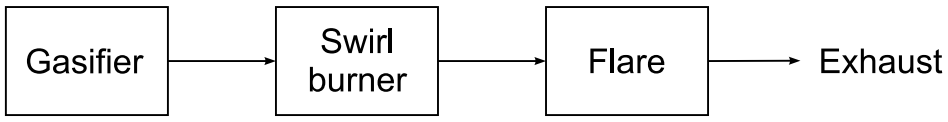

Figure 4.1 : Basic test-setup layout.

4.2 Gasifier

The biomass gasifier is not a goal of this study, but a means to produce the necessary product gas. Based on this thought the design demands for the gasifier become: (1) it should have a simple design, (2) it should be easy to operate, (3) it should produce (a lot of) tar, and (4) it should have a power of approximately 20 kW. A gasifier power of 20 kW is chosen because the gasifier then becomes large enough for reliable operation, while it is still small enough to build and operate in our laboratory.

Based on these demands, it is chosen to design and construct a 20 kW batch operated updraft gasifier. Updraft gasifiers are generally easy to operate and can handle a broad range of fuels with moisture contents up to 50% [45]. An updraft gasifier also produces a lot of tar due to its specific process. A batch operated process is chosen to prevent the common leakage and blockage problems of fuel feed systems. A consequence is that the run-time of the gasifier is restricted.

In the following sections first the principles of updraft gasification are described, after which the design of the gasifier is discussed in detail.

4.2.1 Updraft gasification

Fixed bed updraft gasification can best be described using reaction zones. The zones present in a updraft gasifier are an oxidation, a reduction, a pyrolysis and a drying zone, as shown in figure 4.2(a). The gasification fuel (in this case biomass) is packed onto a supporting grate at the bottom of the gasifier. The gasifying agent (in this case air) is injected below the grate and diffuses upwards through the bed of fuel. In all zones different reactions occur, who all together convert the biomass and gasifying agent into product gas and ash.

The main reactions taking place in each zone are shown in figure 4.2(b). In the oxidation zone, complete oxidation of char takes place to produce very hot (~1000°C) CO_2 and some H_2O. The ash remaining after the char oxidation is removed through the supporting grate. In the reduction zone, the hot oxidation gases rising from the oxidation zone endothermically react with char to form H_2 and CO. In the pyrolysis zone, the ascending hot (~750°C) reducing gases release heat to the descending dry biomass, by which the biomass thermally decomposes into gases (CO, CO_2, H_2, H_2O, CH_4), tar, and charcoal. The charcoal formed in the pyrolysis zone descends into the reduction and oxidation zone, where it is used in the reigning reactions. The heat that remains in the gases rising from the pyrolysis zone, is used in the drying zone to dry the wet biomass. [12, 71]

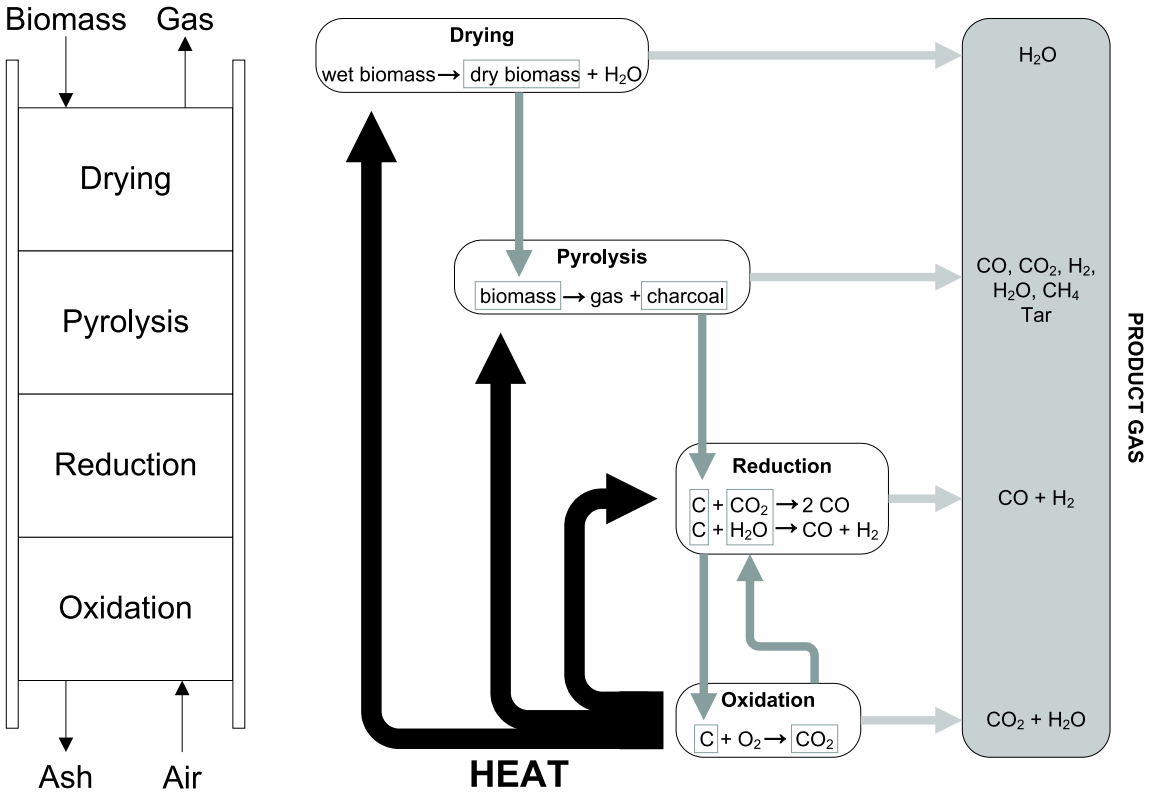

(a) Zones in updraft gasification

(b) Chemistry in updraft gasification

Figure 4.2 : Schemes of an updraft gasification process.

4.2.2 Fuel and oxidizer conversion rates

Fuel conversion rate

Beech-wood chips (~10×10×2 mm) are used as fuel for the gasifier. These are used because they produce very little ash, and are readily commercially available. The average moisture content and lower heating value LHV_{fuel} of the beech-chips are approximated at 13% and 18 MJ/kg respectively. To obtain a gasifier capacity P_{gasifier} of 20 kW, the fuel conversion rate $\dot{m}_{\text{fuel}}$ should become $1.1{\cdot}10^{-3}$ kg/s, following:

$$\dot{m}_{\text{fuel}} = \frac{P_{\text{gasifier}}}{LHV_{\text{fuel}}}. \tag{4.1}$$

Oxidizer conversion rate

The amount of oxygen used in the gasification process is measured by the air-excess ratio λ, and determines the reaction products and the temperatures in the process. A typical air-excess ratio for biomass gasification processes is 0.25. At this ratio the energy conversion from wood to gas reaches a maximum.

If heat losses to the environment are neglected, it is likely that a batch-type updraft gasification process automatically runs at an air-excess ratio of 0.25. Consider for instance a stable gasification process running at an air-excess ratio of 0.25. If the oxidizer feed rate is increased, the char in the oxidation zone is rapidly consumed. This char oxidation generates extra heat, which increases the rate of the pyrolysis process above. The pyrolysis will thus produce char at a higher rate. A new balance will be found where char oxidation again equals char production. This balance is found at an air-excess ratio of 0.25. This equilibrating process also holds if the oxidizer feed rate is decreased instead of increased. However, a requirement is that the total height of the gasification zones does not exceed the height of the batch load of biomass.

Consequence of the equilibrating process is that the gasifier will always adapt its balance to the amount of oxygen introduced. So the amount of oxidizer introduced determines the speed of the gasification process and the power of the gasifier, but will not affect the efficiency of the process.

If biomass combustion is assumed to occur typically [71] by

$$CH_{1.4}O_{0.6} + 1.05O_2 \rightarrow CO_2 + 0.7H_2O, \tag{4.2}$$

then gasification of biomass at an air excess ratio of 0.25 requires 0.2625 mol O_2 per mol biomass ($CH_{1.4}O_{0.6}$). Using the molar weight of oxygen and biomass, the molar ratio can be converted into a weight ratio of 0.365 kg O_2 per kg biomass. The 20 kW gasifier has been determined to use biomass at a rate of $1.1{\cdot}10^{-3}$ kg/s, which results in an approximate oxygen usage rate of $4.0{\cdot}10^{-4}$ kg/s. At standard conditions (300 K, 1 bar) this approximately coincides with $1.8{\cdot}10^{-3}$ kg/s or $1.45{\cdot}10^{-3}$ Nm^3/s air.

4.2.3 Gasifier dimensions

Gasifier diameter

The diameter of the gasifier will be based on a '*The Battelle*' gasifier, which is a proven updraft gasifier design. A Battelle gasifier typically has a diameter of 0.9 m and a biomass conversion rate of 90 kg/h [60]. For biomass with a LHV of 18 MJ/kg, the grate capacity of a Battelle gasifier is equal to 0.7 MW/m^2. It is chosen to base the gasifier design on the same grate capacity as used in a Battelle gasifier. A 20 kW gasifier then should have a grate-area of approximately $2.9 \cdot 10^{-2}$ m^2. This grate-area coincides with an inner gasifier diameter of 0.192 m. For reason of DIN-standardization the outer gasifier diameter is chosen to be 0.219 m (NW 200).

Gasifier height

The height of the gasifier is determined by the laboratory height. Due to the height necessary at the top and at the bottom of the gasifier for feeding and cleaning purposes, the maximum height of the gasifier is restricted to 1.5 m. For a nominal Battelle reaction front velocity of 0.6 m/h [60], such a height results in a batch run-time of approximately 2.5 hours. This run-time is very short for gasification standards, but is still long enough for testing partial combustion in a downstream swirl-burner. The dimensions of the gasifier thus become as shown in figure 4.3.

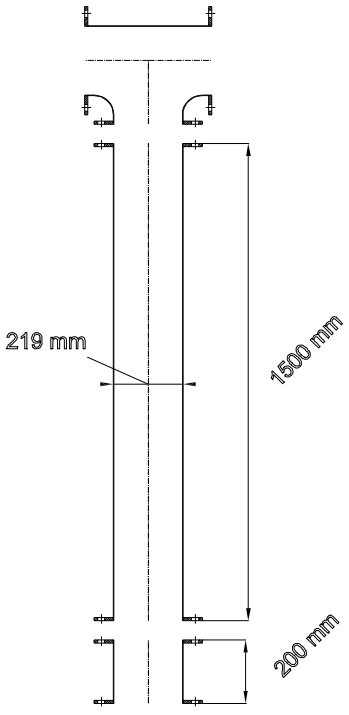

Figure 4.3 : Gasifier dimensions.

Gasifier material

The construction material of the gasifier is steel 1.4762, which is a heat resistant nickel-free material. A nickel-free material is chosen to prevent any catalytic tar decomposition by the Nickel component in a material. The disadvantage of using steel 1.4762 is that the gasifier pipe has to be rolled from sheet material. Therefore, the wall thickness is restricted to 2 mm, which leads to a relatively small maximum gasifier pressure.

As turned out later, nickel is only released from ordinary steel in considerable rates at high temperatures. Contrary, tar is only found in the relatively cold parts of an updraft gasifier. So where there is nickel there is no tar, and where there is tar there is no nickel. As a result, means could have been saved, and construction could have been simplified, by choosing a nickel-containing heat resistant steel. Furthermore, the updraft gasifier probably produces such a lot of tar that any catalytic tar decomposition will probably not even be noticed.

Maximum gasifier pressure

Because of the small wall thickness of the gasifier and the high temperatures in the oxidation zone, the allowable pressure in the gasifier is restricted. The overpressure p_+ (based on the tangential wall pressure stress in a pressurized cylindrical vessel) in the gasifier that leads to fracture after 10^4 h can be calculated using:

$$p_+ = \frac{\sigma_{\backslash} t}{R_{\text{gasifier}}}, \tag{4.3}$$

where $\sigma_{\backslash}$ is the creep strength of the material, t the wall thickness, and R_{gasifier} the gasifier radius. The creep strength (the level of stress that can be taken and results in fracture at 10^4 h) is dependent on the temperature, and is given for steel 1.4762 in table 4.1.

Table 4.1 : Creep strengths of the gasifier material at specified temperatures. The value marked by * is extrapolated.

Temperature (°C)	600	700	800	900	1000
Creep strength 10^4 h (MPa)	35	9.5	4.3	1.9	1.0*

Using the creep strength of the gasifier material at 1000°C, the maximum overpressure p_+ in the gasifier becomes 0.018 MPa. The maximum gasifier pressure is thus approximately 1.2 bar. This value is relatively small considering that the pressure loss over the biomass-bed may thus not become higher than 0.2 bar. Fortunately, the gasifier wall (in the oxidation zone) will probably not reach temperatures of 1000°C due to heat losses to the other gasifier zones and the environment. The maximum allowable pressure in the gasifier increases strongly for lower temperatures, for example to 1.8 bar for a wall temperature of 800°C.

Next to the tangential stress, the longitudinal stress in the gasifier wall is considered. It is assumed that the longitudinal stress is most critical at the oxidation zone due to the high temperatures. The total stress in longitudinal direction is equal to the sum of the longitudinal wall pressure stress and the longitudinal stress due to the weight of the gasifier. The longitudinal wall pressure stress is equal to half the tangential wall pressure stress. Using equation 4.3, the longitudinal wall pressure stress at an overpressure of 0.2 bar becomes 0.55 MPa. The longitudinal weight stress is estimated at 0.19 MPa, by dividing the assumed total weight load on the gasifier wall at the height of the oxidation zone of 25 kg by the cross-sectional gasifier wall area. The total longitudinal stress on the gasifier wall at the oxidation zone thus becomes 0.74 MPa. This stress level is lower than the maximum stress of 1.0 MPa at 1000°C, because of which the longitudinal stress in the gasifier wall will probably not be problematic.

4.2.4 Gasifier bottom end

The bottom end of the gasifier should house some special functions. It is the place where (1) the oxidizing air is provided, (2) the gasifier is ignited, (3) the biomass grate is supported, (4) the produced ash is collected, (5) an extinguishing agent is provided, and (6) an emergency overpressure line is fixed. The design of all necessary utilities is described below.

Ash container

The bottom end of the gasifier is physically formed by an ash container. The ash container is a tube of the same diameter and construction material as the gasifier, but only has a height of 0.20 m (see figure 4.3). At its top, the ash container is bolted to the main gasifier tube by a flange connection. At its bottom, the ash container is closed by a blind-flange. The ash container is used to collect the ash that falls through the grate, and to create a buffer to distribute the air evenly over the grate for a uniform gasification process. To remove the ash from the ash container, the blind-flange has to be removed. An ash-tube is placed on top of the blind-flange to hold the ash when removing the blind-flange. The ash-tube diameter and height are chosen to just fit the ash container.

Grate

As discussed before, the biomass is supported by a grate. The grate should provide openings for the air to flow to the biomass, and for the ash to fall into the ash container. Because the grate will be subject to harsh conditions (oxidative environment, high temperatures, combustion gases, mechanical load of the wood bed) it is chosen to construct the grate of 3 mm thick perforated stainless steel 304. The perforations are 5 mm in diameter and give a total grate porosity of 35%. The perforations are

small enough to prevent the biomass or coal to fall through the grate, while the porosity is high enough for the oxidizer and ash to pass the grate.

The grate is supported by three protuberances fixed at the top of the ash container. The protuberances each span 60°, and are equidistributed along the circumference of the ash container. Because the grate contains three similar protuberances, it can be installed by positioning the protuberances of the grate onto those of the ash-container. Protuberances are used because the grate can then be removed without removing the ash-container by turning the grate 60°. The holes that appear between the gasifier wall and the grate when the grate is in place, are filled by three protruding intruders on top of the ash-tube, as shown in figure 4.4. Because of this grate supporting method, the blind-flange can be removed without moving the grate. This is advantageous if work on the blind-flange is required when the gasifier is already fed with a batch load of biomass.

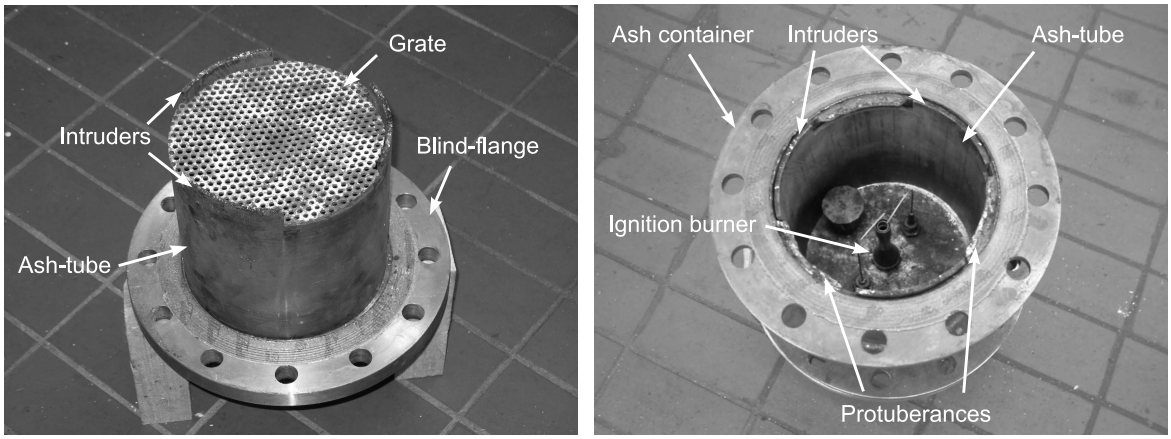

(a) (b)

Figure 4.4 : Blind-flange, ash container, ash-tube, grate, and ignition burner design. The intruders fill the holes between the gasifier wall and the grate when the grate is in place.

Ignition burner

A Bunsen-burner is positioned on top of the blind-flange (as shown in figure 4.4) to ignite the gasification process with its flame. The burner is fed with methane and air in a near stoichiometric ratio, and its fuel power can be adjusted between 0 and 3.5 kW. The flame is ignited by controlled spark-ignition, and is monitored by a flame-ionization-detector. Once the flame is ignited it directly heats the biomass on top of the grate. To reduce the total amount of fittings to the blind-flange, the air supply line that is used for the Bunsen-burner is also used to supply the gasification air.

Nitrogen flush line

A nitrogen supply-line is added to the blind-flange. This line is used to flush the gasifier prior to, and after a run, and to extinguish the gasifier if necessary. Nitrogen can be used to extinguish the gasifier as it is inert and drives away all gases from the gasifier. The nitrogen flush line is fixed by a tube protruding the blind-flange. On top of the tube a cap is placed to prevent ash to fall into the supply-line.

Overpressure line

To prevent too high pressures in the gasifier due to blockages downstream of the gas feeds, an overpressure line is attached to the blind-flange. The overpressure line is fixed to the blind-flange in the same way as the nitrogen flush line: a pipe protruding the blind-flange protected against ash by a cap. The overpressure line is made of stainless steel 304 and has a diameter of 25.4 mm.

4.2.5 Gasifier necessities

The gasifier produces product gas and heat, which both have to be contained in the setup. Therefore, a connection has to be made between the gasifier and the up-scaled swirl-burner, and the gasifier has to be insulated. The design of the gasifier top and its connection to the swirl-burner, and the design of the gasifier insulation are described below.

Gasifier top

The product gas produced during gasification leaves the gasifier at its top. A gasifier top is necessary that directs the product gas towards the swirl-burner, and that gives access to the gasifier for biomass feeding purposes. A T-piece is attached to the top of the gasifier. The base of the T-piece is flanged to the top of the gasifier tube, and its side arms are closed by blind flanges. As the T-piece will be subject to temperatures up to 300°C in an aggressive environment, it is made out of stainless steel 316. The dimensions of the gasifier top have already been shown in figure 4.3. One of the side arms is used to feed the gasifier with a batch load of biomass, by removing the blind flange temporarily. Because flange connections are used, a biomass feed system can be attached to the gasifier if longer gasification runs are necessary. The other side arm is used to attach a product line to, which transports the product gas to the swirl-burner.

Product line

The product line thus transports the product gas from the gasifier to the swirl-burner, but will also be used to transport the product gas from the swirl-burner to the flare. Due to the oxidative, acidic and condensative properties of product gas,

the product line is constructed of highly chemical resistant stainless steel 316 pipe. For a product gas flow of 2.9 g/s, a product gas density assumed equal to that of air at standard conditions, and a nominal gas velocity of 2 m/s, a product line diameter of 39.5 mm is necessary. For DIN-standardization, a pipe is chosen with an outside diameter of 48.3 mm (DN40) and a wall thickness of 2.0 mm. To keep the setup flexible to additions and changes, flange-connections with graphite seals are used.

The product line is heated to 300°C by heating-tape to prevent any tar condensation. To reduce heat loss, the product line is insulated. An alkaline earth silicate (AES) wool blanket that can be used up to 1100°C is used for the insulation due to good practical experiences. The heat loss resistance Ω of the insulation layer against respectively conduction and convection is calculated using:

$$\Omega = \frac{\ln(R_o/R_i)}{2\pi kL} + \frac{1}{2\pi R_o L h}, \tag{4.4}$$

in which R_o and R_i are the outer and inner insulation radii, k and h the conduction and convection coefficients of the insulation material, and L a measure for the pipe length. The heat loss resistance of the pipe itself is not taken into consideration, as the pipe is considered to be at a constant temperature of 300°C. By using the derivative of equation 4.4, the critical insulation thickness of minimum heat loss resistance is determined to be 3.5 mm. Adding more material will benefit the insulation and reduce the heat loss. For practical reasons it is chosen to use an insulation layer with an outside diameter equal to the outside diameter of the flanges. This gives an insulation layer thickness around the product line of 50 mm.

Further, to be able to measure tar concentrations in the product gas before and after the swirl-burner, two tar sampling points are added to the product line. Tar concentrations are determined by a Solid Phase Adsorption (SPA) method. A sample is collected by adsorption and condensation at room temperature on an s.p.a. column containing 100 mg of amino phase following the method described by Brage [9]. A needle (Luer lock, 0.9 mm i.d. x 120 mm) is fixed to the top of the s.p.a. column and a gastight syringe (100 ml) to the base of the column. Tar samples are taken by inserting the syringe needle into the product line via a septum (three layer Teflon coated silicone, with maximum injector temperature of 280°C). A Teflon coated septum is used to withstand the aromatic compounds present in the product line. A 100 ml sample is collected by pulling product gas through the column using the syringe. The column is subsequently disconnected and has to be sent off for analysis.

Gasifier insulation

To prevent heat loss from the gasifier as much as practically possible, the gasifier is insulated with the same material as the product line. To come to a practical and good insulation, the effects of the insulation thickness and an aluminum radiation sheet have been considered.

At first instance two configurations are studied, one without (configuration A) and one with (configuration B) an aluminum radiation sheet, as shown in figure 4.5. The resistance of conduction through the gasifier wall and the insulation layer, the conduction resistance through the aluminum sheet, and the convection and radiation resistance of the outer layer to the environment are modeled. To study the insulation differences between both configurations the temperature of the gasifier wall is considered constant at 900°C. Material parameters have been assumed temperature independent.

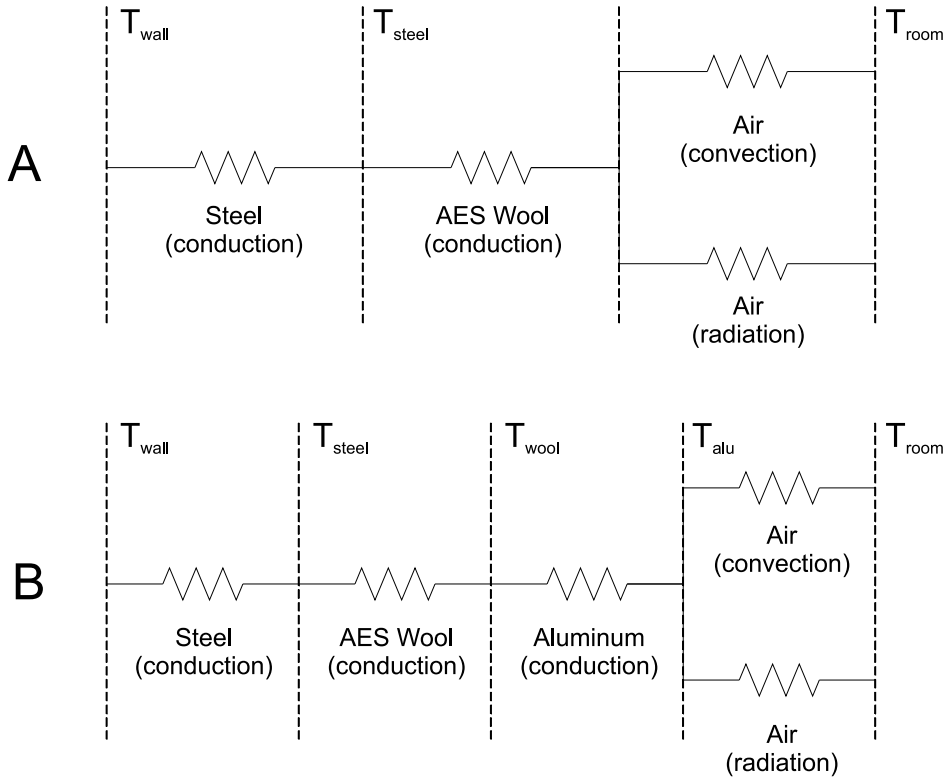

Figure 4.5 : Insulation resistance schemes for configurations A and B, respectively without and with an aluminum radiation sheet.

The heat loss results as a function of the wool layer thickness for configurations A and B are are shown in figure 4.6. It shows that an aluminum radiation sheet is beneficial to reduce the heat loss up to a AES wool layer thickness of 0.1 m. Above that layer thickness the heat loss becomes constant, irrespective of the layer thickness or the aluminum sheet.

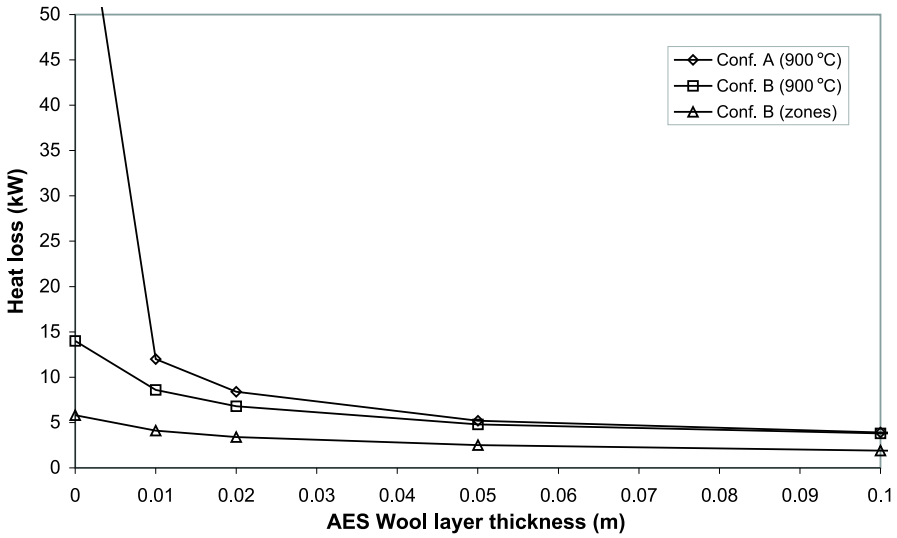

Figure 4.6 : Gasifier heat loss as a function of the insulation layer thickness for various configurations. [1]

A drawback of the previous heat loss estimates is that a gasifier wall at constant temperature is considered. A more realistic heat loss has been calculated by assuming wall-temperature-zones for configuration B. The assumed wall temperatures and zone-heights are based on the expected temperatures and zone-heights in an updraft gasifier. The assumed zonal distribution is given in table 4.2.

Table 4.2 : Gasifier wall temperature zones.

1.2 m	200 °C	Drying zone
0.1 m	400 °C	Pyrolysis zone
0.1 m	900 °C	Reduction zone
0.1 m	1100 °C	Combustion zone

The results of the zonal calculation are again shown in figure 4.6. It shows that a zonal approach leads to lower heat losses than a constant wall-temperature approach. This is a result of the lower average gasifier-wall temperature. It further shows that the heat loss reaches a stable value at an insulation thickness of 0.05 m. Therefore, it is chosen to use an insulation layer of 0.05 m backed up by an aluminum radiation sheet. The total gasifier heat loss is expected to approximate 2.5 kW.

4.2.6 Instrumentation

Next to the tubing and insulation already described, process equipment is necessary to feed the gases to the gasifier. Further, a control unit is designed for easy control of the gasifier during operation. The process equipment used and the design of the control unit are discussed below.

Process equipment

In figure 4.7 the process equipment used to run the gasifier is shown. The air, methane and flush nitrogen feeds are controlled by Mass Flow Controllers (MFC) and fast shut-off valves (FSV). An emergency nitrogen feed line is supplied that, next to a shut-off valve, contains a flow transmitter/indicator (FT/FI) for visual reference. The pressure in all gas supply lines is monitored by pressure indicators (PI).

The status of the gasifier is measured by temperature transmitters attached to the outside of the gasifier at different heights. The temperature transmitters do not protrude the gasifier wall because the gasifier material is hard to attach fittings on, and because the transmitters are not strong enough to last through the filling of the gasifier. The top temperature transmitter does measure inside the gasifier as it protrudes the same blind flange as the product line is attached to. The startup Bunsen-flame is ignited by spark ignition, and is detected by a flame ionization detector. Next to the ionization detector, the ash container also contains a temperature transmitter (TT) to monitor the status of the Bunsen-flame. The temperature transmitters used are K- or N-type thermocouples.

The overpressure line opens either by a controlled shut-off valve or a pressure relieve valve. The pressure in the gasifier is measured by a pressure transmitter, which is located in the overpressure line as its temperature limits are restricted. The pressure relieve valve is used as a back up for the controlled shut-off valve in case of a control error or a current blackout. The pressure relieve valve opens at an absolute pressure of 1.5 bar. A temperature transmitter is added to the overpressure line because the shut-off valve has to be replaced if its temperature increases over 90°C.

Controller

The process equipment is operated by a pre-programmed control-unit. Three standard gasifier control-modes are programmed: a flush mode, a start-up mode, and a shut-down mode. In these modes the control is fully automated by monitoring of the settings and conditions, and emergency actions to be taken if a system failure occurs. The settings of the control-modes can be adjusted via a touch-screen. Next to the standard control-modes, the gasifier can be run on manual mode, which enables bypass of the gasifier control.

During flush mode the gasifier is flushed with nitrogen (30 l/min) by opening the nitrogen MFC. The flush mode continues until a set flush-time (6 min) has been reached, after which the system goes into rest.

During start-up mode the gasifier is ignited and subsequently automatically operated till gasification has to be stopped. Before ignition the total system is checked for correct pressures and temperatures or any system errors. If there are no errors, the air and methane FSV's are opened and their MFC's set to the start-up settings of 2.5 and 20 l/min respectively. Then the spark ignition is used to light the Bunsen-flame in the ash container. If the ionization pen detects the flame, it is kept on till the lowest temperature transmitter on the gasifier wall determines a certain preset temperature (500°C). At that temperature the gasifier is assumed 'on', the methane feed is closed, and the airflow is set to the gasification setpoint of 90 l/min. If during start-up mode no flame is detected or a system failure occurs, the start-up mode is stopped and the gasifier proceeds in shut-down mode.

During shut-down mode the gasifier is extinguished by closing the air and methane MFC's and opening the nitrogen MFC at its flush setting. This mode is continued until a manual reset is given, after which the entire gasifier system goes into rest. The shut-down mode is triggered when the Bunsen-flame extinguishes during ignition, when the temperature at the top of the gasifier reaches its preset maximum (which is set at 350°C to save downstream equipment), when a system error is detected, or when the shut-down mode is selected on the touch-screen.

In case of a current blackout, a pressed emergency button, or if the gasifier pressures limit is reached, the non-controlled emergency-nitrogen feed is opened. This results in a nitrogen feed flow of approximately 50 l/min, which is used to quickly extinguish the gasifier. In case of an overpressure, or current blackout, the controlled overpressure valve will be opened as well.

By using the touch-screen, the control of the gasifier can be adjusted. Values that can be set are the flow settings of CH_4, air and N_2 under each gasifier mode, the maximum gasifier pressure, the 'gasifier on' temperature, the maximum gasifier-top temperature, and the maximum overpressure-line temperature.

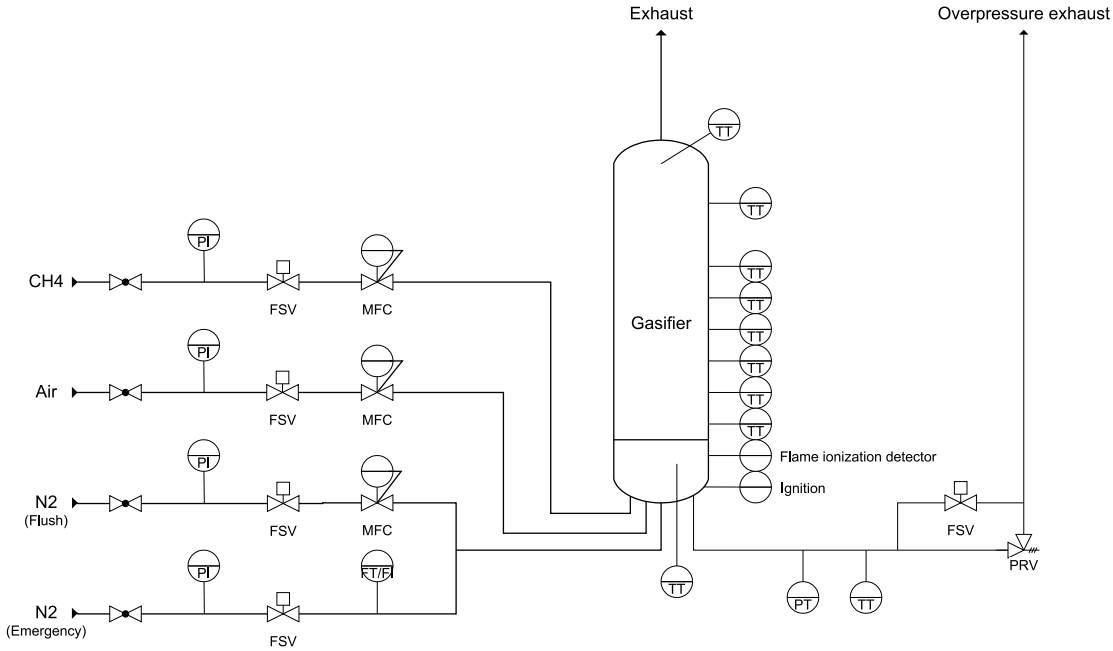

Figure 4.7 : Gasifier process equipment scheme: FI = Flow Indicator, FSV = Fast Shut-off Valve, FT = Flow Transmitter, MFC = Mass-Flow Controller, PI = Pressure Indicator, PRV = Pressure Relieve Valve, PT = Pressure Transmitter, TT = Temperature Transmitter.

4.3 Flare

The gas cleaning unit must clean the produced gases of poisonous and combustible substances, and convert or remove tar. These demands can all be met by controlled oxidation of the product gases: the main combustible species (H_2, CO, CH_4) and the tar are combusted to produce H_2O and CO_2. It is chosen to design a flare to oxidize the gas coming from the gasifier. In this section the design of the flare is discussed.

4.3.1 Basic design

The design of the flare is based on tubular combustion chambers as used in gas-turbines. In those combustion chambers a fuel stream is stoichiometrically combusted with air in a primary oxidation zone. The primary zone is followed by two or more staged cooling zones, by which the combustion process is optimized. The basic flare design is schematically shown in shown in figure 4.8.

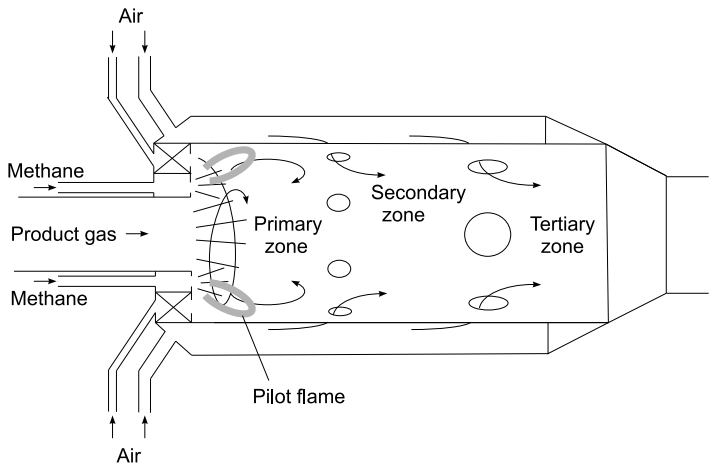

Figure 4.8 : Schematic flare design without quaternary zone, adapted from [20].

The combustion process in the flare is also based on a staged combustion/cooling. In a primary combustion zone, product gas and air are continuously supplied and mixed to create a (near) stoichiometric combustion process. A swirl generator is used on the air feed, to create a circulating flow path and subsequent good mixing of the product gas and air. To ensure ignition of the gas mixture, a stoichiometric methane/air pilot flame is used in the primary oxidation zone.

The flare has three cooling zones after the primary oxidation zone, which are referred to as the secondary, tertiary, and quaternary zone. In the secondary zone, air is added to cool the gases from the primary zone to approximately 1800 K to ensure complete CO oxidation. In the tertiary and quaternary zones the gases are further cooled and diluted by air to approximately 1200 K and 800 K respectively. A stepwise cooling is used to allow the combustion gases some residence time in a high

temperature oxidative environment to stimulate full combustion of any left-over tar components.

The described combustion process takes place inside a circular duct referred to as flame tube. The product gas, pilot methane, and the air are injected into the flame tube through an injector block. The air for the three cooling zones is injected into the flame tube from a surrounding circular casing. Several holes of different radii are used in the flame tube to inject the air and obtain the preferred zone temperatures.

Typical zone lengths are given by Lefebvre [50], who states that the typical length of the primary zone is about 1.5 times the diameter of the flame-tube. The length of the secondary zone can be based on the chemical kinetics, the residence time, or on the length needed for jet-mixing. A typical secondary zone-length varies between 0.5 and 1.0 times the flame-tube diameter. Typical lengths of the tertiary and quaternary zone vary between 1.5 and 1.8 times the flame-tube diameter.

4.3.2 Fuel and oxidizer feed rates

Pilot flame

It is chosen to operate the pilot flame at a nominal power of 2 kW. For stoichiometric pilot flame combustion this means that approximately 0.04 g/s methane and 0.69 g/s air need to be fed to the primary oxidation zone.

Fuel

The fuel of the flare is formed by the product gas leaving the swirl-burner. The product gas composition after the swirl-burner is assumed to be equal to the normal product gas composition from an updraft gasifier shown in table 4.3. The product gas feed rate is estimated at 2.9 g/s following section 4.2.2, disregarding air addition in the swirl-burner.

Table 4.3 : Normal product gas composition according to [61].

Component	Vol.%
H_2	20
CO	20
CH_4	2
Rest (CO_2 + H_2O + N_2 + tar)	58

Primary oxidizer

Next to the air necessary for the pilot flame, an amount of air is necessary to combust the product gas. To obtain stoichiometric combustion, the molar ratio of product gas to oxygen has to be 1:0.24, as can be calculated from table 4.3 when excluding tar as a combustible component. Assuming a product gas density equal to that of air, the necessary amount of air for stoichiometric combustion is 1.14 gram per gram of product gas. This results in a total primary oxidizer flow of approximately 3.3 g/s or $2.8{\cdot}10^{-3}$ Nm^3/s.

Secondary, tertiary, quaternary air

To determine the necessary amounts of cooling air in the secondary, tertiary and quaternary zone, the combustion temperature of the primary zone has to be known. The adiabatic combustion temperature of the primary zone has been determined using the program Gaseq, which calculates chemical equilibria in perfect gases [82]. Using the product gas, methane and air feed flows determined above, the adiabatic combustion temperature becomes approximately 2000 K (under the assumption that all feeds are 300 K and have a similar heat capacity and density to air at standard conditions).

Enthalpy balances can be used to determine the necessary amount of cooling air in each zone to obtain the prescribed temperature. A basic enthalpy balance that can be used is

$$\dot{m}_{\mathrm{gas-in}} \cdot \bar{c}_{p_{\mathrm{gas-in}}} \cdot (T_{\mathrm{gas-in}} - T_{\mathrm{out}}) = \dot{m}_{\mathrm{air}} \cdot \bar{c}_{p_{\mathrm{air}}} \cdot (T_{\mathrm{out}} - T_{\mathrm{air}}), \tag{4.5}$$

in which $\dot{m}_{\mathrm{gas-in}}$ is the mass flow of gas to cool, $\bar{c}_{p_{\mathrm{gas-in}}}$ the average gas heat capacity at constant pressure, $T_{\mathrm{gas-in}}$ the gas temperature, T_{out} the preferred temperature at the end of the zone, $\bar{c}_{p_{\mathrm{air}}}$ the average air heat capacity at constant pressure, T_{air} the air temperature, and $\dot{m}_{\mathrm{air}}$ the necessary amount of air.

Using equation 4.5, the secondary, tertiary and quaternary air mass-flows have been calculated to become as shown in table 4.4. It was assumed that the air inlet temperature equals 300 K, and that the gas leaving the combustion zone consists of equal amounts of CO_2 and H_2O. The average heat capacities have been determined by using the heat capacity equations for gas mixtures from [29] and the heat capacity data from [41].

To verify whether air addition in the cooling zones does not lead to temperature releasing oxidation reactions, Gaseq has again been used. Only in the secondary zone some oxidation reactions can be expected, but their influence on the process temperature is minute. Therefore, the enthalpy balance method in equation 4.5 is acceptable for calculating the necessary amounts of cooling air.

Table 4.4 : Mass flows of gases in the flare.

Gas	$\dot{m}$ (g/s)
Product gas	2.90
Methane	0.04
Primary air	3.99
Secondary air	1.44
Tertiary air	8.67
Quaternary air	19.84
Total	36.88

4.3.3 Flare dimensions

Casing

In the design of gas turbine combustion chambers the casing diameter can be determined using a reference velocity u_{ref}, which is the mean velocity across the casing area in absence of the flame tube [49]. The reference velocity typically ranges from 4 to 30 m/s [80]. The inside casing diameter D_{casing} is determined using

$$u_{\text{ref}} = \frac{\dot{m}_{\text{total}}}{\bar{\rho}_{\text{in}} \cdot \frac{1}{4}\pi D^2_{\text{casing}}}, \tag{4.6}$$

in which $\dot{m}$ is the summed mass flow of all flows entering the combustion chamber, and $\bar{\rho}_{\text{in}}$ is the average density of the respective mass flow at the combustion chamber entrance. The total mass flow entering the combustion chamber is equal to 36.88 g/s, as shown in table 4.4. Since 92% of the total mass flow at the entrance of the combustion chamber is air at room temperature, $\bar{\rho}_{\text{in}}$ is considered equal to the air density at standard conditions, which is approximately 1.2 kg/m^3. A low reference velocity has a positive influence on combustion stability and residence time, but increases the combustion chamber dimensions. As combustion stability is more important than small dimensions, the reference velocity in the flare is chosen to be 2 m/s. Using equation 4.6, the casing inside diameter should become approximately 0.140 m. The final outside casing diameter is based on DIN-standardization, and is chosen to be 0.139 m (NW 125).

Flame tube

The diameter of the flame tube in gas turbines can be determined by using the ratio k of the square flame tube diameter over the square casing diameter:

$$k = \frac{D^2_{\text{flametube}}}{D^2_{\text{casing}}}. \tag{4.7}$$

According to Lefebvre [50] the optimum k-value ranges from 0.7 to 0.8, which corresponds to a flame tube diameter of 0.116 to 0.124 m (disregarding wall thickness).

Following DIN-standardization, the flame tube is chosen to have an outside diameter of 0.114 m (NW 100) and wall thickness of 6 mm.

The flame tube is in direct contact with the product gas, combustion products, and the combustion process itself. That is why it is chosen to construct it of heat resistant steel 310s, which can resist temperatures up to 1100°C. Thermal expansion of the flame tube is taken into account in the construction of the flare. The thermal expansion ΔL can be estimated to be approximately 9 mm using

$$\Delta L = \alpha L \Delta T, \tag{4.8}$$

a thermal expansion coefficient α of 18 μm/(m $\cdot$ K), a tube length L of 0.5 m (see next section), and a temperature rise ΔT of 1000 K.

Air injection holes for the cooling zones

To obtain proper distribution of the cooling air when it is injected from the casing into the flame tube, its penetration should be approximately 0.2 times the flame tube diameter [49]. According to Lefebvre [49] the maximum penetration $Y_{\max}$ of round air jets into a tubular liner can be estimated using:

$$\frac{Y_{\max}}{D_{\mathrm{j}}} = 1.25 \left(\frac{\rho_{\mathrm{j}} u_{\mathrm{j}}^2}{\rho_{\mathrm{g}} u_{\mathrm{g}}^2} \right)^{0.5} \cdot \frac{\dot{m}_{\mathrm{g}}}{\dot{m}_{\mathrm{g}} + \dot{m}_{\mathrm{j}}}, \tag{4.9}$$

where D_j is the diameter of the jet, ρ the density, u the velocity, and $\dot{m}$ the mass flow rate. The indices g and j indicate the main gas stream and a single jet respectively. Due to vena contracta after gas discharge from a sharp orifice, the jet diameter D_{j} will be smaller than the injection hole diameter D_{h}. The jet diameter can be estimated using

$$D_{\mathrm{j}} = CD^{0.5} \cdot D_{\mathrm{h}}, \tag{4.10}$$

in which CD is a discharge coefficient. In case of a sharp orifice, the discharge coefficient can be estimated at approximately 0.6 [15].

Setting the amount of holes n in the secondary, tertiary and quaternary zones to 5, 15 and 11 respectively, and taking the jet velocity approximately equal to the main stream velocity, suitable hole diameters would be 21.5, 22.1, and 22.9 mm respectively. However, for historic reasons the hole diameters are only 9, 10, 13 mm respectively, due to which the jet velocity is not equal to the main stream velocity. Worse, however, is that the maximum penetration becomes similar to the flame tube diameter, due to which probably strong turbulence is created. Table 4.5 gives a summary of the temperature T, gas velocity u_{g}, amount of holes n, hole diameter D_{h}, jet diameter D_{j}, jet velocity u_{j}, and the maximum jet penetration $Y_{\max}$ per zone.

Figure 4.9 shows an impression of the flame tube with the air injection holes for the secondary, tertiary and quaternary zones, including dimensions.

The lengths of the primary and secondary oxidation zone are determined using the typical zone lengths given in section 4.3.1. Since the tertiary oxidation zone is mainly used for cooling, its length is chosen arbitrarily. The length of the quaternary oxidation zone is relatively long, as the zone continues in the exhaust.

4.3.4 Injector block

The injector block has a threefold function, it should (1) feed the product gas to the flame tube, (2) feed all air to the flame tube, and (3) feed the methane to the flame tube. Furthermore, it should induce a swirling motion on the air feed, for increased fuel/oxidizer mixing and better combustion stability.

The injector block is constructed of a circular block with feed openings for the product gas, the methane, and the air. The top deck of the block is positioned in the flame tube, approximately 50 mm from the flame tube bottom. The feed of the product gas is in the center of the deck. The feed openings for the methane are positioned in a circle around the product gas entry. The air openings form a circle around the methane openings and are positioned near the flame tube wall, as can be seen in figure 4.10. The swirl-motion is created by drilling the air feed holes under a angle of 45° in circumferential direction.

To prevent flash-back in the methane feed line, the methane is fed to the flame tube through 12 holes of 2 mm diameter, the small diameter of the holes acting as a flame arrester. Both the air for the primary product gas oxidation as the air for the pilot flame are fed through the same holes for construction reasons. Tests have shown that for flame stability it worked best to have 24 air injection holes of 5 mm.

Other tests have shown that it was necessary to lift the product gas inlet above the level of the air and methane inlets. If the product gas is released into the flame tube at the same level as the air and methane, the pilot flame extinguishes due to large product gas recirculations into the pilot flame area. Thus, to stabilize the pilot flame, the product gas enters the flame tube 30 mm above the injector block deck through an injection nipple, as shown in figure 4.11. The diameter of the opening in the top of the product gas injection nipple converges from 34 mm to 20 mm to increase the product gas velocity and minimize product gas recirculation into the pilot flame area.

Table 4.5 : Data of air injection in the secondary, tertiary and quaternary zone, T is the zone temperature, u_g is the main gas velocity, n is the amount of air injection holes, D_h is the hole diameter, D_j is the air jet diameter, u_j is the air jet velocity, and Y_{max} is the maximum penetration depth.

Zone	T[K]	u_g [m/s]	n [-]	D_h [mm]	D_j [mm]	u_j [m/s]	Y_{max} [m]
Secondary	1800	0.71	5	9	7	6.2	0.073
Tertiary	1200	0.85	15	10	8	9.6	0.106
Quaternary	800	1.74	11	13	10	19.1	0.124

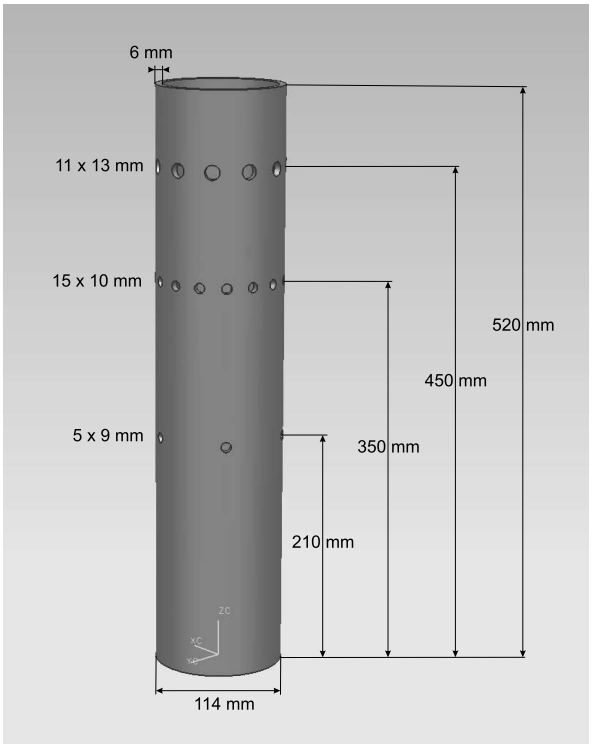

Figure 4.9 : Flame tube design.

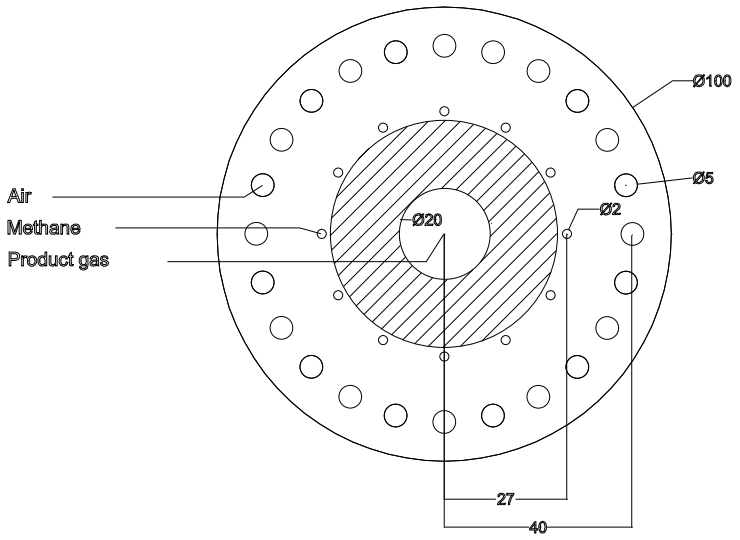

Figure 4.10 : Top view of injector block, dimensions in mm.

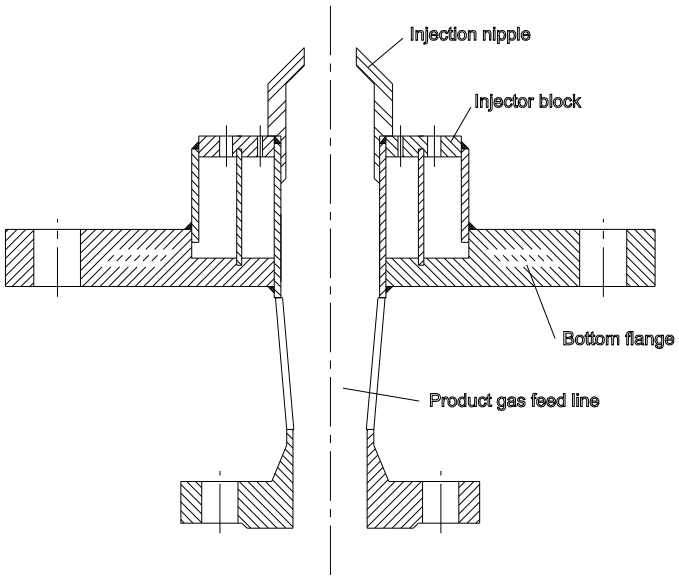

Figure 4.11 : Cross section of the injector block and construction flanges. Feed openings to injector block chambers are not shown.

4.3.5 Instrumentation

Next to the design and construction of the flame tube, the casing and the injection block, the flare also needs process equipment and a controller to guarantee its functioning. The flare should basically work automated, except for start-up and shut-down. In this section the equipment used and procedures developed to automate the flare are described.

Process equipment

The basic process equipment scheme of the flare is shown in figure 4.12. The product gas enters the flare from a heated product line through a flow transmitter/indicator (FI/FT). The flow transmitter is used to get an idea of the product gas flow, based on which the necessary amount of primary air is determined. The product gas flow measured is only a rough estimate of the real product gas flow, because the flow meter has been calibrated for air under the assumption that the product gas properties are roughly similar to that of air. Furthermore, the necessary amount of air is also a rough estimate, as the product gas composition is not known. To prevent fouling and clogging, the flow meter is heated to 300°C, which basically restricts its type to float-type flow meters. These have the disadvantage of a float protruding the product gas flow, but also the advantage of easy dismantling and cleaning possibilities.

The methane flow for the pilot flame is controlled by a Mass Flow Controller (MFC). For safety and fast control a fast shut-off valve (FSV) is added to the methane feed line.

The flow of air to the injector block is controlled by two parallel MFC's, one to provide the air necessary for the product gas combustion, and one to provide the air necessary for the pilot flame. The secondary, tertiary, and quaternary zones are controlled by air addition through proportional valves (PV). All air necessary for the flare is fed by a single feed line, in which a fast shut-off valve is used for safety reasons.

Further equipment are pressure transmitters (PT) and pressure indicators (PI) in the methane and air feed lines, two temperature transmitters (TT) protruding the flare wall to measure the cooling zone temperatures, a pilot flame spark ignition, a flame ionization detector, and an infrared (IR) flame detector.

Controller

The flare is operated by a pre-programmed control unit, whose setting can be adjusted via a touch-screen. There are three programmed modes for the flare to be in: start-up mode, flare-on mode and shut-down mode.

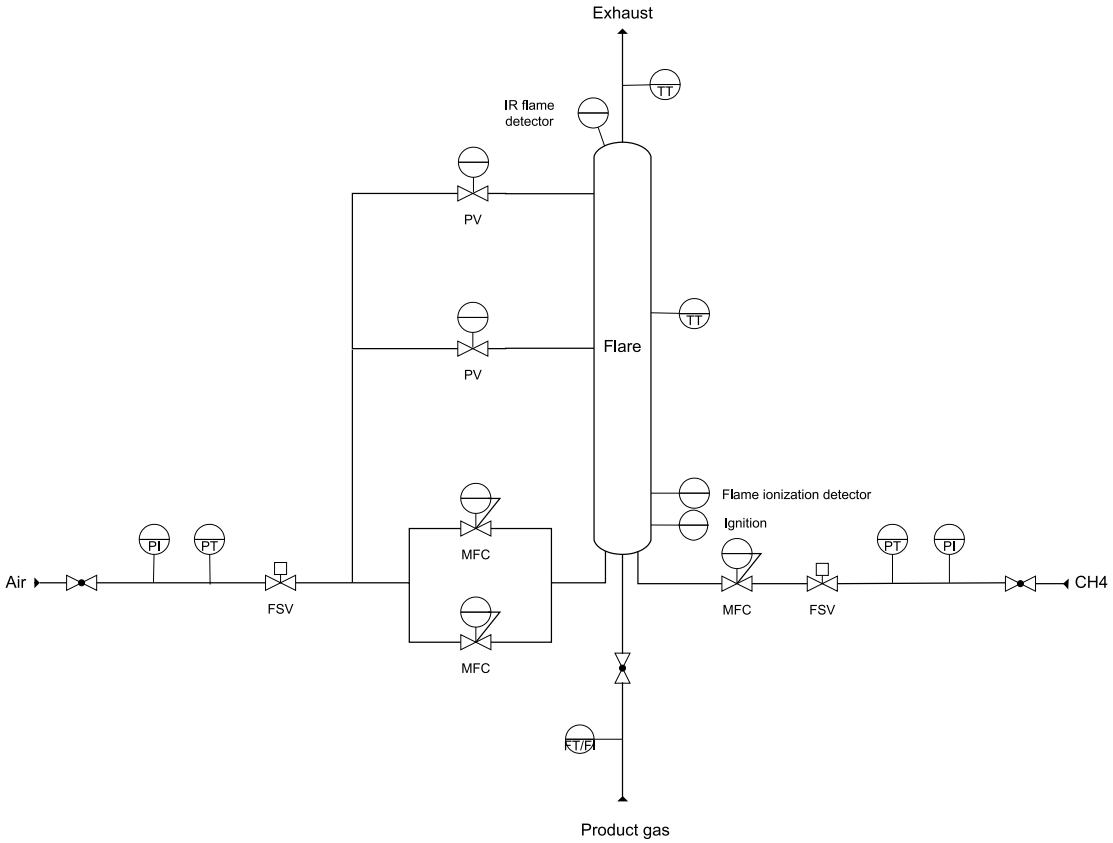

Figure 4.12 : Flare process equipment scheme: FI = Flow Indicator, FSV = Fast Shut-off Valve, FT = Flow Transmitter, MFC = Mass-Flow Controller, PI = Pressure Indicator, PT = Pressure Transmitter, PV = Proportional Valve, TT = Temperature Transmitter.

During start-up mode the feed line pressures are checked, the methane and air shut-off valves are opened, the methane and air mfc's are positioned into their pilot flame settings (3 and 75 l/min respectively), the spark ignition is turned on for 10 seconds, and the presence of a flame is checked. If the pressure in the feed lines is too low (<4.5 bar), the controller blocks the start-up sequence. If there appears to be no flame after 10 seconds of ignition, the start-up is stopped. If the pilot flame is properly ignited, the flare proceeds in the flare-on mode.

During flare-on mode the amount of primary air is directly controlled by product gas flow transmitter via a multiplication value (set to 1). The amount of secondary, tertiary and quaternary air is controlled by the thermocouple readings and the cooling zone settings. Once the temperatures in the zones reach their maximum set values of 900 and 500°C respectively, the proportional valves are opened to keep the temperature constant at its set maximum value.

If, for any reason, the flame in the flare extinguishes, the spark ignition tries to re-ignite it for 10 seconds. If the flame re-ignites, the flare continues in flare-on mode. Otherwise, an emergency shut-down is triggered which shuts the methane feed and opens the air feeds to their maximum to flush the flare. The flare is continuously flushed until a manual reset is given. If, during flare-on mode, the pressure in the feed lines becomes too low, or an emergency button is pressed, the controller also triggers an emergency shut-down.

The normal shut-down mode basically follows the same procedures as an emergency shut-down, but it will only flush for 10 minutes after which the flare goes into a resting situation until it is started up again.

By using the touch-screen, the control of the flare can be adjusted. Values that can be set are the minimum pressures in the feed lines, the maximum temperatures in the cooling zones, the pilot flame power, the methane-air multiplication factor, the product gas-air multiplication factor, the amount of air to flush with, and the PID-control of the proportional valves.

4.4 Experimental gasifier setup operation

The setup as described above has been tested several times after it was finished. The tests showed that the gasifier and the flare basically work well, although some operational parameters have to differ considerably from their design parameters. Both the gasifier and the flare showed some problems during the tests performed, but no major adjustments to the setup are necessary. The problems found for the gasifier and flare are discussed below.

4.4.1 Gasifier

Ignition of the gasifier showed harder than expected. The premixed methane-air Bunsen-flame is hard to keep lit during the first stage of gasifier ignition. This is probably caused by the combustion gases that gather in the ash container, which create hard circumstances for the Bunsen-flame to burn. Opening the overpressure line, with the goal to drive away all combustion gases, did not bring any improvements. However, if after several restarts the temperature level in the ash container rises above 600°C, the Bunsen-flame remains stable.

While the temperature in the ash container strongly rises during ignition, the temperatures measured at the outside of the gasifier hardly rise. The gasifier wall temperatures only start to rise (strongly) when the ignition flame is turned off and gasification is started. As a consequence, it is hard to determine from the gasifier outside-temperature, when the gasifier can be considered 'on'. For this reason it is better to base the assumption 'gasifier on', on the time the ignition flame has burned stable (e.g. 10-15 minutes), instead of on the gasifier temperature.

Once the gasifier is ignited it runs very stable, although the temperatures in- and outside the gasifier are lower than expected. Maximum gasifier temperatures measured are just over 800°C, while the product gas temperature during gasification slowly increases from $\pm$ 50°C to $\pm$ 150°C.

During burnout, at the end of a 7.0 kW gasifier run, the temperature of the product gas remains below 270°C. Although it is expected that the maximum product gas temperature will rise if the gasifier power is increased, the product gas temperature does not seem to form any problems for the downstream equipment.

Product gas quality

The product gas quality as produced by the gasifier has been measured during two runs at gasification powers of 18.5 kW and 7.0 kW respectively. The product gas quality is determined by GC-TCD (Gas Chromatography by a Thermal Conductivity Detector).

The measured gas compositions during the first hour after start-up of the 18.5 kW gasification process are shown in figure 4.13. It shows that the product gas composition is relatively constant although its CO content gradually rises, while its CO_2 and N_2 content slowly decrease. After the first hour of gasification the product gas composition seems to have stabilized to the values shown in table 4.6. The trace amounts of oxygen measured in the product gas might have passed the gasification process, but might also be present due to small leaks in the GC sample line. The summed amount of measured product gas approximately equals 90 vol.%, although it should ideally measure 100 vol.%. This difference is probably caused by unmeasurable components (such as water vapor and heavy hydrocarbons) and by

GC calibration errors. The lower heating value of the product gas rises from 4.1 MJ/Nm^3 at start-up to approximately 5.3 MJ/Nm^3 after an hour in operation.

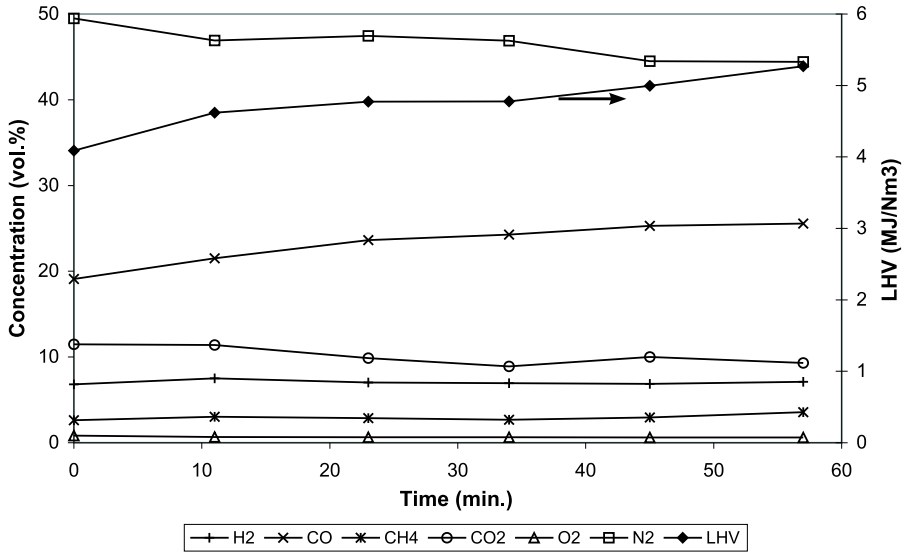

Figure 4.13 : Measured product gas composition after start-up of a 18.5 kW gasification process. Measurement error $< 3\%$ of measured concentration.

During the gas composition measurements at 7.0 kW, the components nitrogen and methane could not be distinguished on the chromatograms due to calibrations errors. Therefore, only the approximate sum of both concentrations is known, and not their single concentrations respectively. Nevertheless, the concentrations of H_2, CO, CO_2, and O_2 are measured as shown in table 4.6. The values for CH_4 and N_2 shown in the table are based on an estimation for the CH_4 concentration. Since the concentrations of both combustible components H_2 and CO have decreased to a fraction of approximately 0.57 compared to their concentrations at 18.5 kW, it is reasonable to expect that the concentration of the combustible CH_4 has decreased just as much. Therefore, the CH_4 concentration is estimated at 1.7 vol.%. Consequently, the N_2 concentration becomes approximately 56 vol.%. Again the total summed concentrations do not add up to 100 vol.% due to unmeasurable components and calibrations errors.

From table 4.6 it shows that the product gas quality is strongly dependent on the gasifier power. At gasifier powers close to the design power of 20 kW, the lower heating value of the product gas is relatively similar to that of the product gas given in table 4.3 for a normal updraft gasifier. Comparing the product gas compositions, shows that the gasifier designed in this chapter produces relatively much CO and relatively few H_2.

At a power of 7.0 kW, the product gas composition changes considerably to the worse. The lower heating value of the gas is decreased considerably by strongly

Table 4.6 : Product gas compositions measured by GC-TCD as a function of the gasification power. The value marked by * is estimated.

Gasifier power	18.5 kW	7.0 kW
H_2 [vol.%]	7	4
CO [vol.%]	25	14
CH_4 [vol.%]	3	1.7*
CO_2 [vol.%]	10	14
O_2 [vol.%]	1	1
N_2 [vol.%]	45	56
LHV [MJ/Nm^3]	5.0	2.8

decreased combustibles concentrations. This low fuel quality at low gasifier power, is probably caused by heat losses becoming relatively high compared to the heat generation. Larger heat losses result in lower process temperatures, due to which the reduction and pyrolysis processes produce less combustibles.

Relatively high heat losses are probably also the reason for the relatively low H_2 concentrations in the 18.5 kW product gas compared to the gas in table 4.3. As discussed above, the temperatures in- and outside the gasifier remained lower than expected. Apparently, the heat losses of the gasifier are still relatively high compared to the heat generation at 18.5 kW. According to [45], the hydrogen concentrations in a product gas rise with increasing process temperature. Therefore, the low H_2 concentrations are attributed to the gasifier heat losses. As low H_2 concentrations could negatively influence any tar cracking by partial combustion (following chapters 2 and 3, and figure 1.4), it might be worth reducing the heat losses or increasing the gasifier power. The heat losses might for instance be reduced, by adding electrical heating to the outside of the gasifier. However, it would probably be best to increase the gasifier diameter.

Next to the product gas quality, also the produced amount of tars during the 7.0 kW gasification run is measured by the SPA method described in section 4.2.5. Analysis of the sample gave the chromatogram as shown in figure 4.14. The kind of species and their respective concentrations are analyzed by Flame Ionization Detection, which yields species concentrations in mVolts. The horizontal axes shows the aromaticity of the detected species by their retention times, a higher retention time meaning a higher aromaticity. During the analysis not all species could be identified, since they were not all calibrated for. Nevertheless, it shows that a wide variety of small aromatics, i.e. 1-ring and 2-ring species, were present in the product gas. Naphthalene is a measured specie with an approximately average aromaticity, which indicates that its use as a model tar component by Houben [40] is justified.

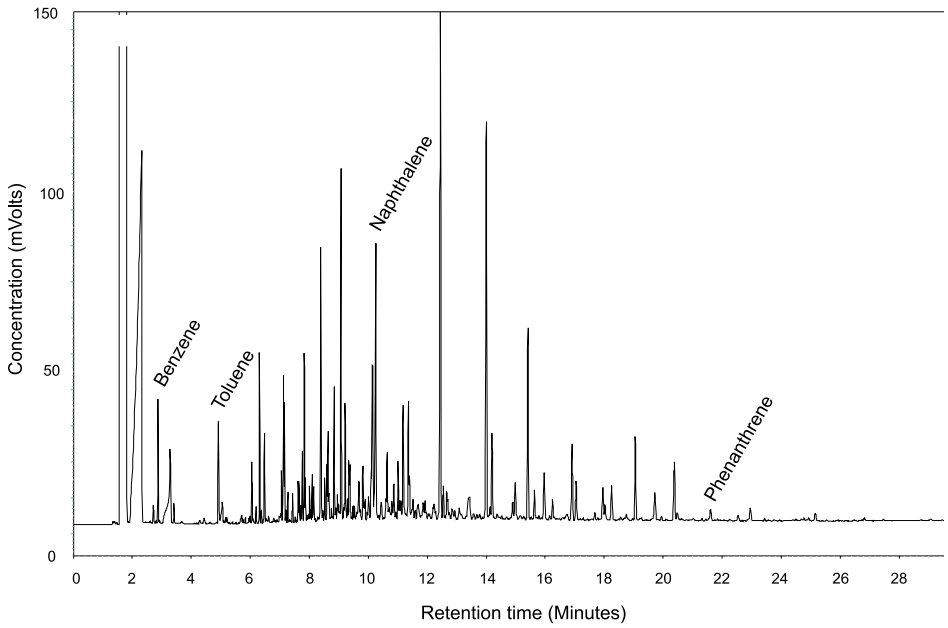

Figure 4.14 : Chromatogram of tar components sampled according to the method of [9] during a 7.0 kW gasification run. The main identifiable components are named in the graph.

4.4.2 Flare

The combustion in the flare is very stable, as can be deduced from the measured temperature profiles (not shown). However, still continuity problems appeared during operation. The flame detection of the flare is a main cause of the flare continuity problems. Variations in the pilot flame position lead to a failing ionization flame detection due to a fixed position of the detecting electrode. Addition of the product gas injection nipple already greatly improved the flame ionization detection because of a better pilot flame stability. Visual inspection of the pilot flame showed that the pilot flame is predominantly positioned near the flame tube wall. This position could have been expected since the swirl motion drives most pilot flame gases outwards. Introduction of an ionization detecting electrode that particularly detects in the region near the flame tube wall solved most of the detection problems.

The IR flame detection showed to work worse than expected. During normal flare operation the detector only now and then detects enough radiation to activate. Only at very high temperatures and much secondary air injection, the IR flame detector worked continuously. Probably the sensor of the IR flame detector is not sensitive enough to detect the flame during normal flare operation. This problem could be solved by bringing the detection probe closer to the flame position, however, this is not possible due to the maximum IR-probe temperature of 600°C. Although the IR flame detection does not work very well, it does improve the flare operability by working in parallel with the ionization flame detection.

The addition of secondary, tertiary, and quaternary air can lead to flame stability problems if their control is prone to oscillations. Therefore, the respective proportional valves are given a nearly overshoot-free PID-control (P = -0.2, I = 8.0, and D = 5.0). Furthermore, when the product gas feed is low, the addition of secondary and tertiary air becomes problematic when their flows rise above 15 l/min. Probably, the injection of air creates flow patterns which influence the flame stability or the flame position. Fortunately, only very few cooling air is necessary at low product gas flows. If the product gas feed is near its maximum, the introduction of secondary and tertiary air does not cause any problems.

The product gas flowmeter showed some peculiar behaviour. The amount of flow measured during a run at constant fuel power varied over a range of 100 to 300 l/min, and could change instantly by several tens of liters a minute. These variations are probably caused by flowmeter fouling, because the flowmeter had to be cleaned thoroughly after each gasifier run due to strong tar condensation. To solve the problem, the flowmeter is removed from the system and the amount of produced product gas is estimated from the amount of air fed to the gasifier. The gasifier air to primary air multiplication factor is determined from the average product gas composition shown in figure 4.13.

4.5 Conclusions

A gasifier and a flare have been designed in order to be able to test partial combustion on real product gas. Goal was to design and construct a simple gasifier which produces product gas containing a lot of tar, and a flare which can combust all the product gas. The gasifier designed is a 20 kW batch-operated updraft gasifier, based on a proven gasifier concept. The flare is based on a tubular combustion chambers used in gas turbines. Although both designs are based on existing work, they both are fully unique in their existence.

Both the gasifier and the flare can be controlled fully automated. However, the automation of the gasifier does not work properly since stabilization of the Bunsen-flame used for ignition shows hard. Further, the temperature levels (which are control-parameters) show hard to interpret for control purposes. The automation of the flare works well, although flame detection remains problematic because of which the 'shut-down' mode is sometimes unnecessarily triggered. The stability of the flare and its flame detection can probably be improved by strongly increasing the pilot flame power. However, this would necessitate hardware changes to the flare, as it is not designed for increased pilot flame powers.

The quality of the product gas produced strongly depends on the operational power of the gasifier. However, at fixed power, the product gas is of approximately constant quality with respect to time. At full power the product gas has a LHV of $\pm$ 5 MJ/Nm^3, mainly formed by its high CO content. The hydrogen content of the product gas is relatively low, probably due to gasifier heat losses. Decreasing the operational power strongly decreases the amount of combustibles in the product gas, leading to very low LHV. Since hydrogen seems a necessary precondition for tar cracking by partial combustion, it becomes questionable whether tar cracking by partial combustion of this product gas can be achieved.

The tar contained by the product gas consists mainly of 1- and 2-ring aromatics. This is advantageous for testing partial combustion, since these components are both prone for cracking as for polymerization. Furthermore, they can be measured relatively easy by gas chromatography. This tar composition further justifies the use of naphthalene as a model tar component in the experiments described in chapter 1.

Chapter 5

Swirl-burner measurements

As in the previous chapter a gasifier test-setup has been constructed, partial combustion can now be tested on real product gas. However, first the limits and necessary conditions for partial combustion are determined by determining the working area of partial combustion in the existing micro-scale swirl-burner. The experimental setup that is used for the working area tests is described in section 5.1. The test results, which give the partial combustion stability in the original swirl-burner design as a function of the fuel power, the product gas composition, and the product gas lower heating value, are given in section 5.2. Furthermore, in section 5.3 the influence of some geometric properties of the swirl-burner on the process stability are discussed.

Based on the determined working area for the micro-scale swirl-burner, a scale-up of the swirl-burner is constructed to fit the test-setup. Part of the scale-up is the design of a spark-ignition system, to ignite the partial combustion process. The scale-up and the design of the spark-ignition system are discussed in sections 5.4 and 5.5 respectively. Once the scale-up swirl-burner is installed, it is tested for its working area and process stability using a synthetic gas, which is described in section 5.6. Subsequently the scale-up is tested on real product gas, as is discussed section 5.7. Finally, in section 5.8, the behaviour of the scale-up swirl-burner during the product gas experiments is discussed.

5.1 Micro-scale experimental setup

A reason for working area tests on the micro-scale swirl-burner is that the process stability shows to be limited. During tests described in previous work [37], the working points as defined by Houben [40] could not be reached due to limited flame stability. For an unknown reason, the circumstances in the experimental setup have changed, due to which partial combustion of product gas is less stable. The working area has to be determined to scan the potential of the present swirl-burner design.

To scan the working area of the partial combustion process, flame stability tests are done in a new setup. The setup is based on the setup used by Houben [39]. It basically consists of a swirl-burner that is fed by product gas and air under controlled circumstances, as is schematically shown in figure 5.1. A methane/hydrogen/nitro-

gen-mixture is used as product gas, because of which the gas composition and its combustion properties can be controlled. Real product gas also contains carbon monoxide as a combustible component. However, this component is considered too poisonous to add to the synthetic product gas in the present setup. The methane and hydrogen level will be adjusted such that the lower heating value of the gas-mixture is similar to that of real product gas.

The methane, hydrogen and nitrogen flows are controlled by three mass flow controllers. The gases are mixed in the gas feed line, which feeds the gas mixture to a preheater. In the preheater the synthetic product gas is preheated to approximately 200°C, which is equal to the gas temperature used by Houben [39]. The preheated gases leave the preheater and are fed to the swirl-burner through a electrical heated feed line.

The air is fed directly to a cavity around the central tube of the swirl-burner. From the cavity the air is directed into the fuel through injection holes, as shown in figure 1.1. The flow of air is controlled by a mass flow controller. To control the amount of oxygen in the partial combustion process, the swirl-burner is positioned underneath a glass bell. The glass bell is flushed by an inert gas to (1) prevent gas recirculations at the swirl-burner top, and (2) to minimize dangerous built up of partial combustion products underneath the glass bell. A mass-flow controlled nitrogen stream of 1 l/min is used as the inert flush. At its top, the glass bell is connected to a vented exhaust.

The temperatures of the synthetic product gas and the partial combustion products are measured using K and N-type thermocouples. The temperature in the preheater is controlled by a hot air blower.

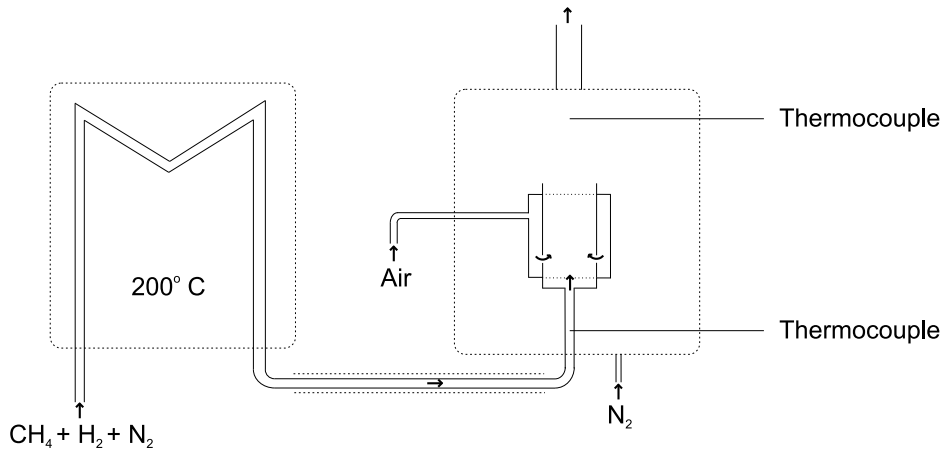

Figure 5.1 : Scheme of small-scale experimental partial combustion setup.

5.2 Partial combustion stability

The swirl-burner used is a new, slightly adapted, version of the swirl-burner by Houben. The basic dimensions, the amount of air injection holes, and the swirl and tilt angles are the same as for the original design. The major difference is that the diverging cone at the top of the swirl-burner is omitted. This omission should not have any significant effect on the partial combustion, since the combustion process seems to take place inside the swirl-burner near the air injection holes, as shown by figure 1.2. The geometry and dimensions of the swirl-burner used are shown in figures 5.2(a) and 5.2(b).

All possible methane/hydrogen/nitrogen-mixtures can be drawn in a single triangular diagram, as shown in figure 5.3. The sum of mole percentages for the three species shown, always equals 100%. In the diagram, isolines can be drawn for all gas compositions with equal LHV or equal hydrogen/methane volume-ratio, as shown in figure 5.4.

The flame stability is first tested at a fuel power of 500 W, because at this low fuel power the stability is best. The partial combustion limits for various mixtures on the triangular diagram are determined by starting at stoichiometry and gradually lowering the air-excess ratio. The air-excess ratio at which the combustion process extinguishes is considered the partial combustion limit. It shows that partial combustion is possible down to an air-excess ratio of practically nil for most gas-mixtures, except for two gas-mixture regions indicated in figure 5.5.

Region I in figure 5.5 is formed by gas with very low LHV. The partial combustion process can probably not be maintained due to large quantities of nitrogen, which cool down the reactions and decrease the possible fuel-oxidizer contact. This is supported by calculation of the flammability limits according to the method described in appendix A. Flammability limits refer to the limit amount of combustible gas capable of bringing flammability on a gas/air-mixture. Mixtures within these limits liberate enough energy on combustion to ignite the neighbouring layer of unburned mixture, and therefore are capable of self-propagation of flame. From appendix A it follows that a premixed methane/nitrogen mixture is never flammable for methane contents lower than 14.3 vol.%, which coincides with a LHV of 5.1 MJ/Nm^3. Similar, a premixed hydrogen/nitrogen mixture is never flammable for hydrogen content lower than 5.7 vol.%, which coincides with a LHV of 0.6 MJ/Nm^3. Both flammability limits approximately coincide with the experimentally determined limits of region I.

From the limiting air-excess ratios for stable partial combustion it can be concluded that not only the flammability limits determine the partial combustion limits. The stability limits namely show to be smaller than the lower λ-limits of flam-

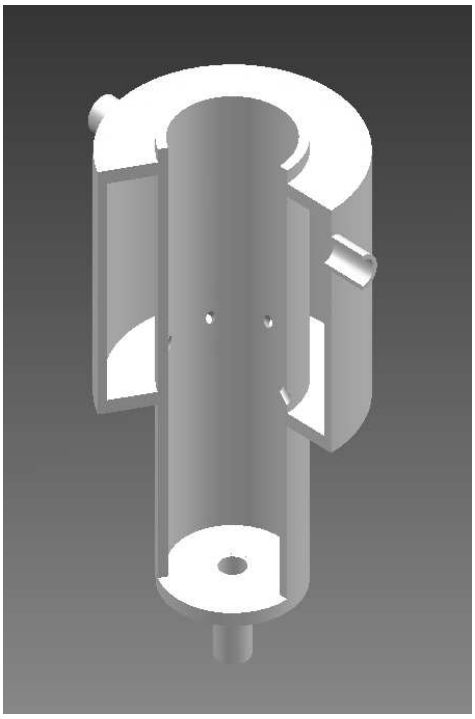

(a) 3D-view

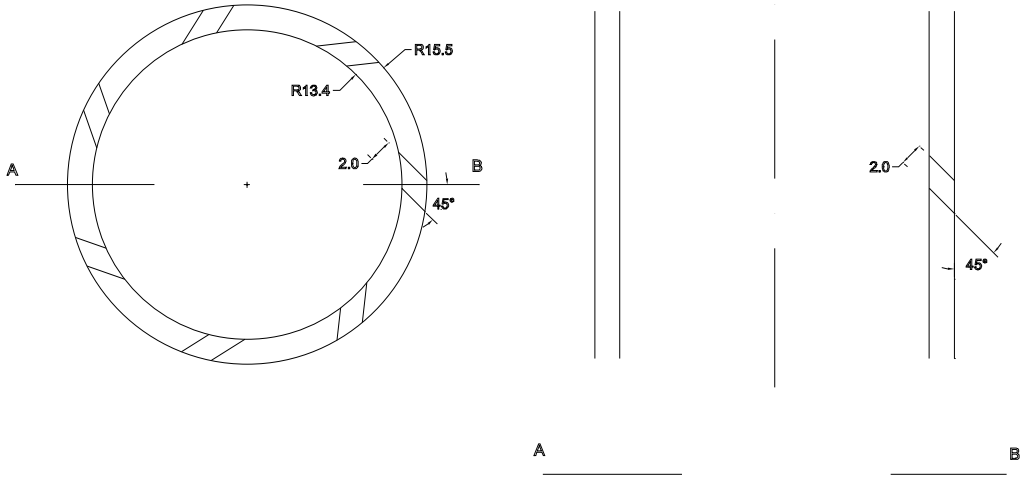

(b) Dimensions of the central tube at the height of the air injection holes in mm

Figure 5.2 : Micro-scale swirl-burner.

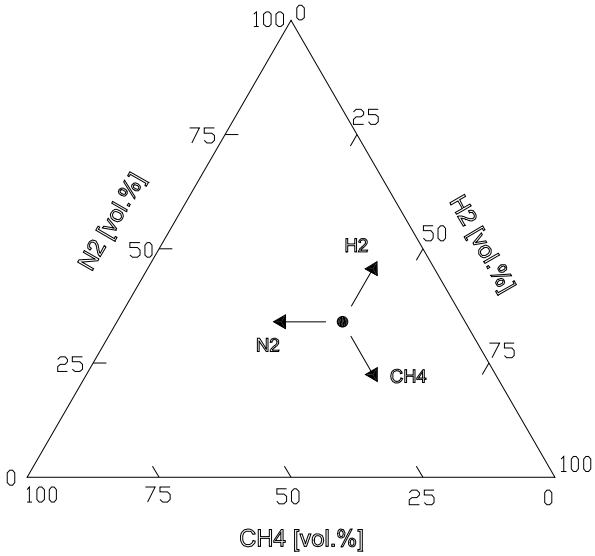

Figure 5.3 : Gas composition triangle. Arrows indicate directions for reading single species concentrations.

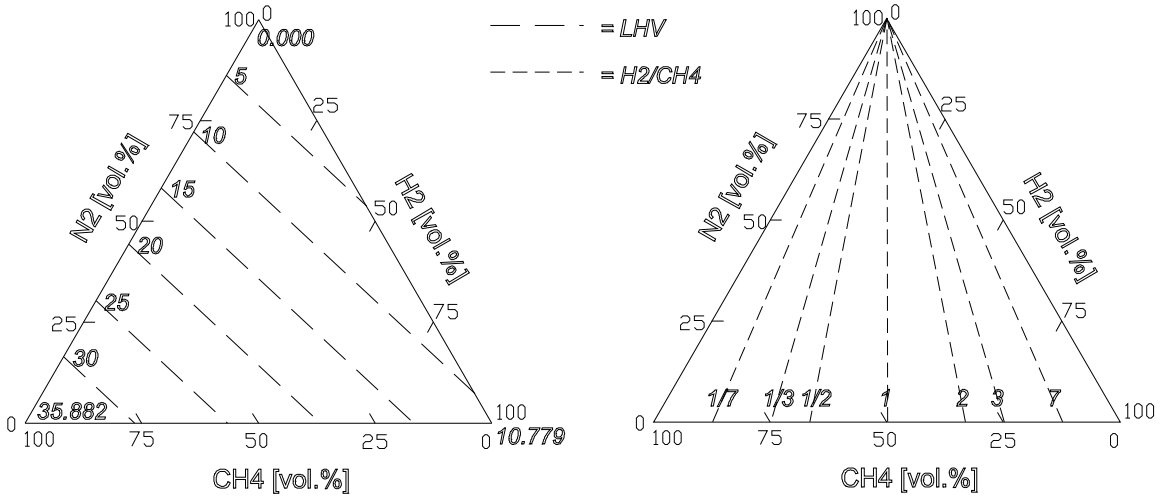

Figure 5.4 : Gas composition triangles, on the left with isolines for LHV in MJ/Nm^3, and on the right with isolines for H_2/CH_4.

mability calculated in appendix A. Apparently the partial combustion process can remain stable while the average fuel/oxidizer mixture is not flammable. This indicates that next to the flammability limits, also the mixing process plays an important role in determining the partial combustion limits. During mixing, local zones with low mixture fraction are formed at the air injection holes, as illustrated in figure 3.1. Just in front of the air injection hole only air is present, which is gradually mixed with the product gas by diffusion or turbulence. Since a mixture gradient is created, there will always be a position where the fuel/oxidizer mixture is flammable. This probably causes the functioning of the swirl-burner at low air-excess ratios. Further, as shows from appendix C, the flame propagation velocities are also likely to play a role in determining the limits of partial combustion. If the flow velocities rise above the flame propagation velocity, the flame is blown off. However, since the jet in cross-flow interaction creates complex 3D flow patterns, this limiting factor cannot be readily compared to the flow velocities.

Region II in figure 5.5 is formed by gas with a high LHV and a low hydrogen/methane volume-ratio. The extinction behaviour in this region is not a consequence of limiting chemical reactivity, but of flow instabilities. This is concluded from the fact that combustion at low air-excess ratio in this region stays stable, if instead of lowering the air-excess ratio at fixed gas composition, the gas composition is changed from high to low hydrogen/methane volume-ratio at fixed air-excess ratio. This shows that the flow profiles have a huge influence on the partial combustion stability for product gas containing a lot of methane. However, this should not be a problem, since product gas formed by gasification often has a high hydrogen/methane volume-ratio.

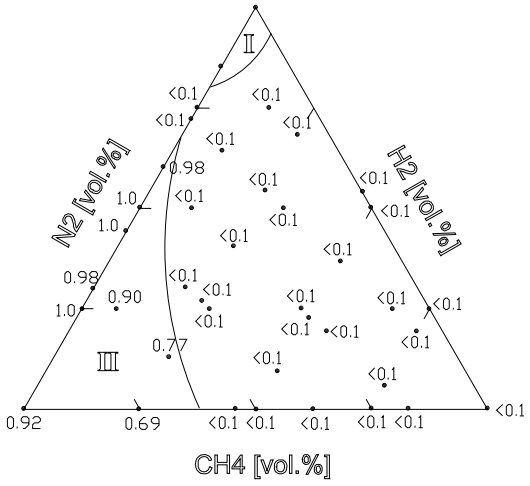

Figure 5.5 : Partial-combustion lower air-excess ratio limits for standard swirl-burner geometry, determined by lowering the air-excess ratio at a fuel power of 500 W. Each dot is a measurement.

The flame stability is further tested by varying the LHV, the hydrogen/methane volume-ratio, and the fuel power around a standard gas setting. The standard setting has a Lower Heating Value of 5 MJ/Nm^3, a fuel hydrogen content of 25 vol.%, an air-excess ratio of 0.2, and a fuel power of 500 W. This setting is chosen because: (1) product gas from a biomass gasifier often has a LHV of approximately 5 MJ/Nm^3, (2) an FHC of 25 vol.% gives a good flame stability according to figure 5.5, (3) according to Houben [39] an air-excess ratio of 0.2 gives the best tar reduction, and (4) because a fuel power of 500 W also gives a good flame stability.

The flame stability results for a fixed hydrogen/methane volume-ratio of 3.9 are shown in figure 5.6 as a function of the LHV and the fuel power. It shows that for a fuel power of 500 W the partial combustion process can be considered stable down to a LHV of 3.5 MJ/Nm^3. For $3.5 < LHV < 4.9$ MJ/Nm^3 and for $8.3 < LHV < 9.3$ MJ/Nm^3, the flames show minor instabilities. However, these instabilities are so small that they do not influence the continuity of the partial combustion process. For $LHV < 3.5$ MJ/Nm^3, the instabilities in the flames become so large that the continuity of the partial combustion process cannot be guaranteed, because of which the process is considered unstable. The minimum LHV at which partial combustion is considered stable, increases with increasing fuel power. For a fuel power of 2800 W, the LHV can only be lowered to 11.8 MJ/Nm^3 before flame instabilities become too large for stable partial combustion. Further, for fuel powers above 500 W, small flame instabilities will always be present during partial combustion.

The flame stability results for a fixed LHV of 5.0 MJ/Nm^3 are shown in figure 5.7 as a function of the fuel hydrogen content and the fuel power. It shows that for a fuel power of 500 W, the partial combustion process stays stable down to a FHC of 10 vol.%, although below 20 vol.% small instabilities become visible. At a FHC of 0 vol.%, partial combustion at an air-excess ratio of 0.2 is not possible. At a certain FHC between 0 and 10 vol.% the flame stability is lost either by blow-off or by flame extinction. The exact lower FHC-limit could not be determined due to flame visibility problems. The minimum fuel hydrogen content at which partial combustion is considered stable increases with the fuel power. An increasing fuel power at fixed FHC leads to a decreased flame stability, and eventually to a no-flame situation.

It shows that stable partial combustion in the micro-scale swirl-burner is limited by the fuel hydrogen content, the lower heating value, and the fuel power, although the real limiting factors are more likely the flow velocities, the flammability limits, and the burning velocities. To obtain flame stability in the process, the FHC and/or the LHV have to increase with increasing fuel power. Shortly, the higher the lower heating value and the fuel hydrogen content, the better the flame stability.

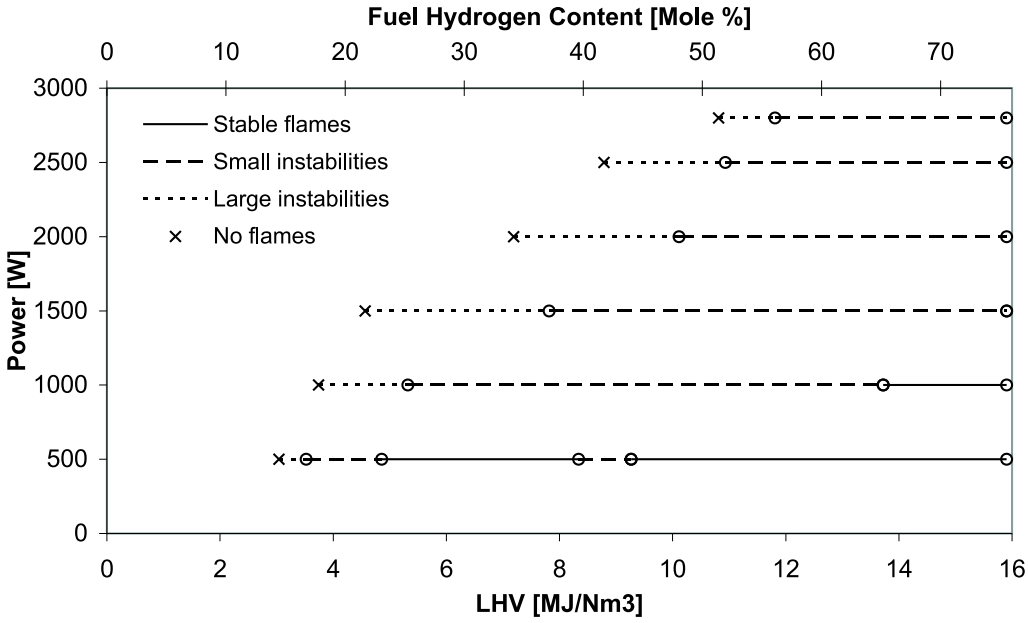

Figure 5.6 : Flame stability as a function of gas LHV and fuel power, for $\lambda = 0.2$ and a fixed hydrogen/methane volume-ratio of 3.9.

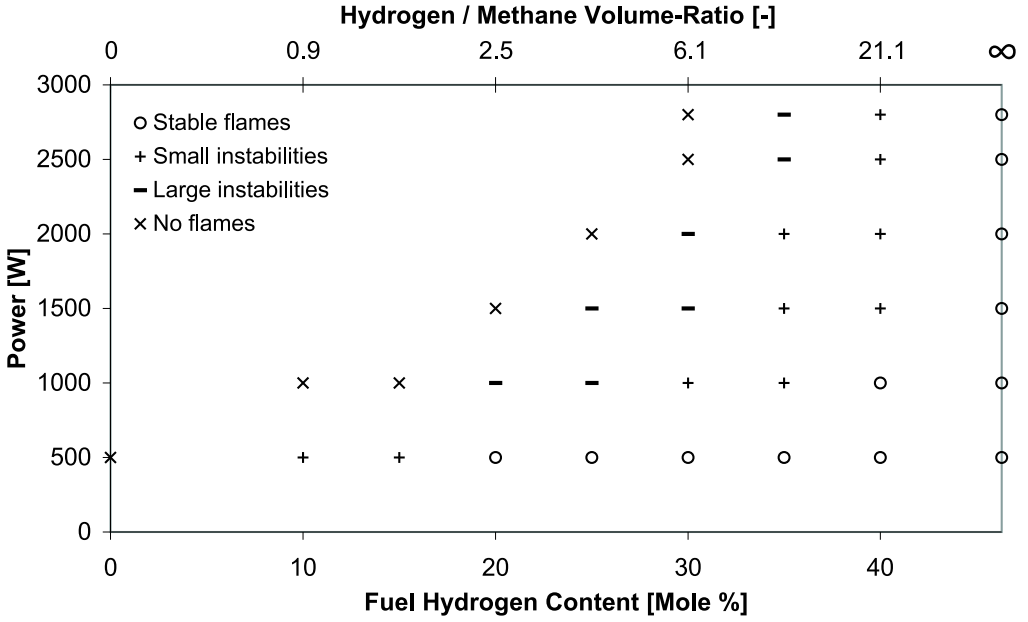

Figure 5.7 : Flame stability as a function of fuel hydrogen content and fuel power, for $\lambda = 0.2$ and a fixed LHV of 5 MJ/Nm^3.

5.3 Swirl-burner influence on process stability

To further study the influence of flow patterns on partial combustion stability, the working area is determined for various burner geometries. In total five geometries are used which all have the same basic dimensions as given in figure 5.2(b). The various burners vary in their swirl and tilt angles, their number of air injection holes, and in the presence of a diverging top. The varying geometric parameters are listed in table 5.1. The burner used in the previous section is referred to as geometry A. In geometry B the swirl angle θ is set to 0° to test the swirl angle influence. In geometry C the tilt angle α is set, next to the swirl angle, to 0° to test the influence of tilt. Geometry D is similar to geometry A, except for the number of air injection holes n. In geometry D the number of air injection holes is increased to 16 while keeping the total air injection area equal to that for geometry A by decreasing their hole size D_h to 1.6 mm. Geometry E is similar to geometry B, except for the diverging cone at its top. Geometry E is used to determine the effect of the diverging cone omission on the flame stabilities in geometry A.

Table 5.1 : Tested burner geometries, α is the air injection hole swirl angle, θ is the air injection hole tilt angle, n is the amount of air injection holes, and D_h is the air injection hole diameter.

Geometry	Cone	θ [°]	α [°]	n [-]	D_h [mm]
A	no	45	45	7	2.0
B	no	0	45	7	2.0
C	no	0	0	7	2.0
D	no	45	45	11	1.6
E	yes	0	45	7	2.0

Figure 5.8 shows the partial combustion limits for geometries A, B, C, and D as a function of the fuel hydrogen content for a fixed LHV. These data are obtained in the same way as the data from figure 5.7. The lines drawn show the limiting value above which or left of which the partial combustion is considered unstable.

The results can be divided into three FHC regimes: a low FHC regime for 0.0 $< FHC <$ 20.0 vol.%, a medium FHC regime for 20.0 $< FHC <$ 32.5 vol.%, and a high FHC regime for 32.5 $< FHC <$ 46.3 vol.%. In the high FHC regime, the power limits for stable partial combustion are highest for geometries A and D. Removing the swirl angle shifts the stability limit down towards lower fuel powers. Removing the tilt angle decreases the stability limit even further.

In the medium FHC regime, the stability limit of geometry D shows highest. The limit of geometry A has decreased compared to geometry D, and at some point even decreases below the limit of geometry B. The stability limit of geometry C stays worst.

In the low FHC regime the stability limits of geometries A, B and D are equal, although the stability limit stretches to lower fuel hydrogen contents for geometry A. Geometry C cannot be operated in the low FHC regime for the powers and LHV tested.

In general it shows that the stability limits of each geometry shift to lower fuel powers for decreasing fuel hydrogen content. The results for geometry C show that a tilt angle in the air injection holes is beneficial for the flame stability. Geometry B shows that at high fuel hydrogen contents it is beneficial to have a swirl angle in the air injection holes, while this benefit does not show in the low and medium FHC regimes. The benefit of either small or large air injection holes depends on the FHC regime. At low FHC fewer large injection holes shows best, while at medium FHC smaller injection holes show better for flame stability. At high FHC the size and amount of air injection holes does not seem to influence the stability limits.

Comparing the results between geometries B and E should give information on the influence of the diverging top. The results in figure 5.9 shows that the stability limit of geometry B is better than that of geometry E over the FHC range of 20.0 to 46.3 vol.%. At lower FHC no differences in flame stability appear.

The results indicate that a diverging cone on top of a burner has a negative influence on the flame stability. Although this result justifies the omission of the diverging cone on geometry A, it cannot be explained. The diverging cone should have no influence on the flame stability since the combustion reactions take place inside the burner. Especially in the high FHC regime where the differences in flame stability are seen, the high burning velocity of the gas mixture [42] should reduce the influence of a diverging cone. Thus, it becomes likely that the differences in stability limit are caused by small differences in the burner geometry, instead of by the diverging cone. Besides, it should be noted that the results are not exactly quantifiable and slightly liable to subjectiveness, since the flame instabilities are visually determined.

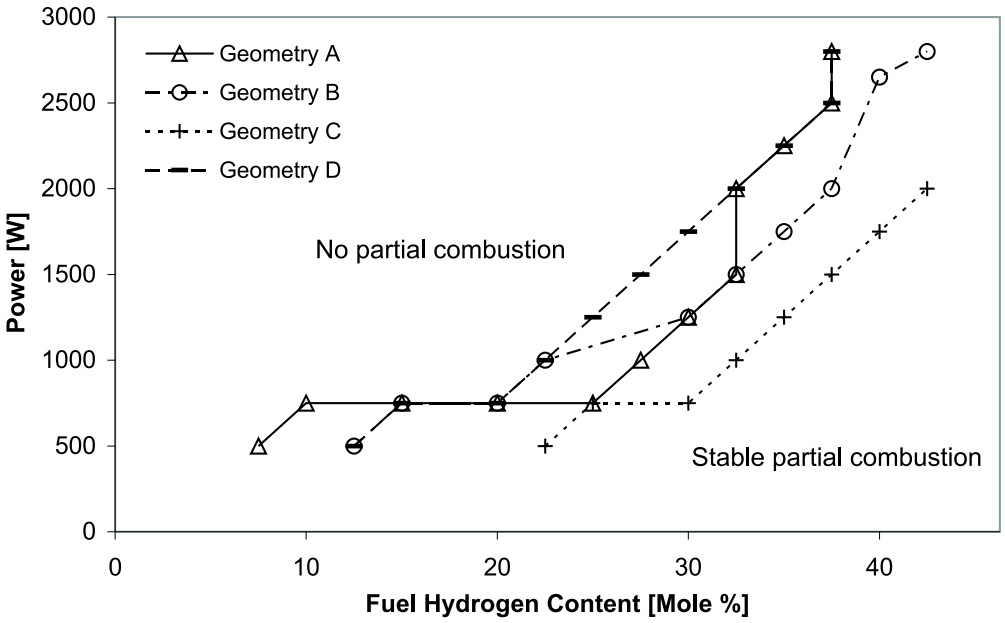

Figure 5.8 : Flame stability boundary for different geometries for $\lambda = 0.2$ and a fixed LHV of 5 MJ/Nm^3.

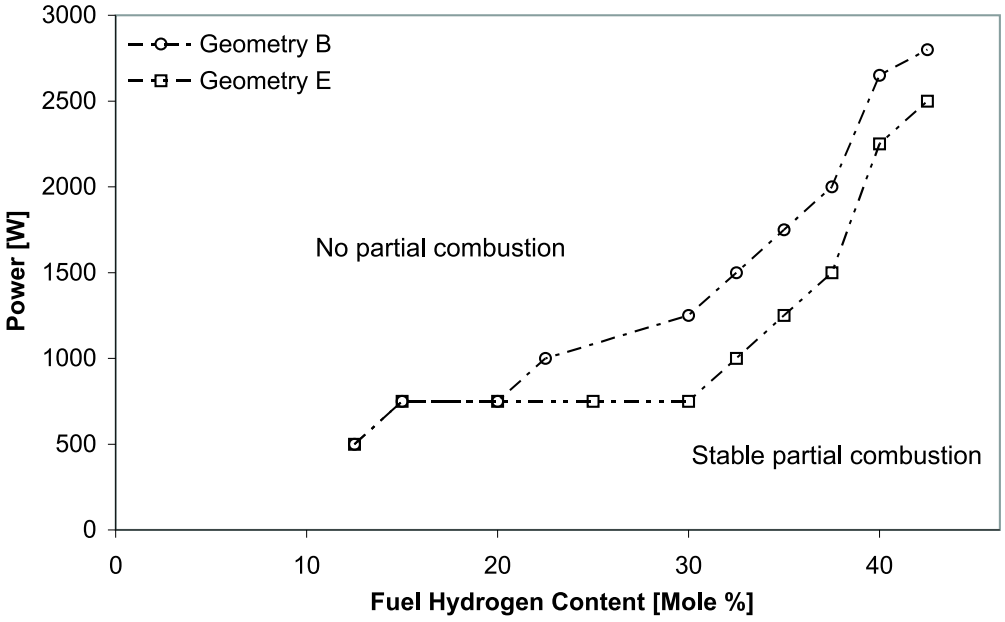

Figure 5.9 : Flame stability boundary for different geometries for $\lambda = 0.2$ and a fixed LHV of 5 MJ/Nm^3.

5.4 Design of up-scaled swirl-burner

For testing partial combustion in the gasifier test-setup described in chapter 4, it is chosen to scale-up swirl-burner geometry A. This burner geometry shows a relatively wide working area, and its design is similar to the original micro-scale swirl-burner by Houben [39]. Originally, burner A was designed for a fuel power of 2.8 kW. The scale-up swirl-burner is designed for a fuel power of 20 kW, which is equal to the designed maximum power of the gasifier test-setup.

The entire scale-up process is based on a constant velocity ratio between the product gas flow and the air injection. This ratio is chosen constant because it gives a fixed flow-area ratio between the main burner diameter and the air injection holes, at least, if the burner is again designed for a product gas lower heating value of 4.2 MJ/Nm^3 and an air-excess ratio of 0.2. By choosing the main up-scaled swirl-burner-diameter, the flow area of the air injection and the absolute flow velocities are determined.

The main internal diameter of the swirl-burner is chosen equal to the internal diameter of the product line (44.3 mm), in order to prevent stepwise diameter variations in the test-setup. Consequential, since the fuel power per flow area rises, the absolute velocities of the product gas and the air injection rise approximately a factor 2.6 compared to the original swirl-burner. Using a flow area ratio $A_{\text{product-gas}}/A_{\text{air}}$ of 25.5 (similar to burner A), and 8 air injection holes (explained later), the air injection holes become 3.1 mm in diameter.

To equalize pressure on the air injection holes, and for construction advantages, an air-chamber is used around the air injection holes. Air is fed to the chamber by two feed-lines to obtain a reasonable air distribution over the chamber. Both feed-lines are fed by the same MFC and are equipped with a no-return valve to prevent back flow of product gas.

Since the partial combustion process is enclosed in a pipe, spark plugs are used to ignite it. The spark plugs are fired continuously to help stabilize the partial combustion process. Since the spark-plugs should spark at the fuel-oxidizer boundary layer, they are each placed just behind an air-injection hole. Due to dimensional limitations the amount of spark plugs is restricted to four.

It is chosen to drill 8 air injection holes due to symmetry in the spark-plug positions. The holes are placed equidistant around the circumference of the product-line under both a swirl and a tilt angle of 45°.

To check whether the partial combustion process is ignited, the temperatures before and after the air injection holes are measured by thermocouples. If partial combustion takes place, the temperature at the second thermocouple should be con-

siderably higher than at the first thermocouple.

Further, the burner is flanged for connecting it to the test-setup. In figure 5.10 and 5.11 a design drawing and the finished up-scaled swirl-burner are shown respectively.

5.5 Spark-ignition system

To activate the spark ignition, the spark plugs have to be fed by an intermittent high voltage charge. Therefore, an ignition system has been designed according to the scheme shown in figure 5.12. The system is based on transistor ignition systems used in the automobile industry. It is chosen to use a transistor ignition because it is fully electronically controlled, and can be set according to desire. The average spark-duration for a transistor ignition system is of the order of 1 milliseconds. Transistor ignition uses a special ignition coil that can give a spark over two spark-plugs almost simultaneously. Since 4 spark plugs are used in the setup, two ignition coils are necessary which each are separately controlled by a transistor. Both transistors are fed by a 12 V power source, and a combined filter/voltage-regulator. A filter and voltage regulator are used to protect the electronic equipment by preventing disturbances in the direct current delivered by the power source. Per transistor one pulse-generator is used to time the creation of sparks.

Each pulse generator consists of an asynchronous multi-vibrator and an inverter. The asynchronous multi-vibrator is used for production of block-type pulses with a duty-cycle of 80%. The inverter is subsequently used to invert the pulse into a duty-cycle of 20%. It is chosen to use a duty-cycle of 20% to obtain long life-times for the ignition coils.

Two Insulated Gate Bipolar Transistors (IGBT) are used for the spark ignition. Each IGBT has one connection with its pulse generator, one connection with the negative pole of the power source, and one connection with the positive pole of the power source through an ignition coil. If a pulse generated by the pulse generator reaches the IGBT, the negative and positive poles of the power source are short-circuited through the ignition coil. During the short-circuitry the ignition coil is charged with an electric current. If the pulse of the pulse generator falls away, the short-circuitry is switched off. As a result, the magnetic field in the ignition coil falls away, which induces a high potential difference (up to 30 kV) over the spark-plugs. When the potential difference over the spark-plug electrodes becomes equal to the dielectric strength of the gas, sparks are created between the spark-plug electrodes. An in-depth explanation of the spark-ignition system including technical electric schemes showing all components is given by Den Dekker [16, 17].

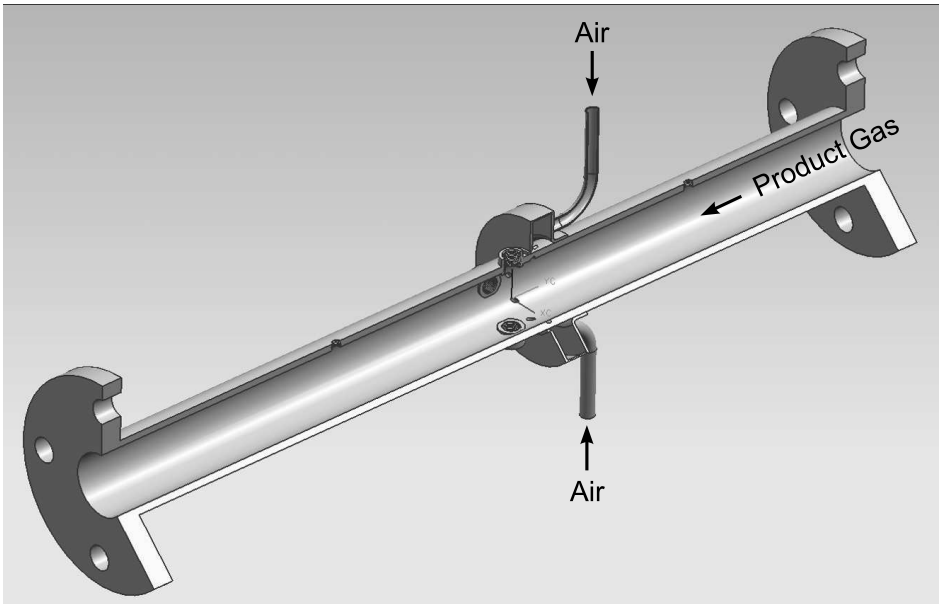

Figure 5.10 : Design drawing of up-scaled swirl-burner, spark plugs and thermocouples not shown.

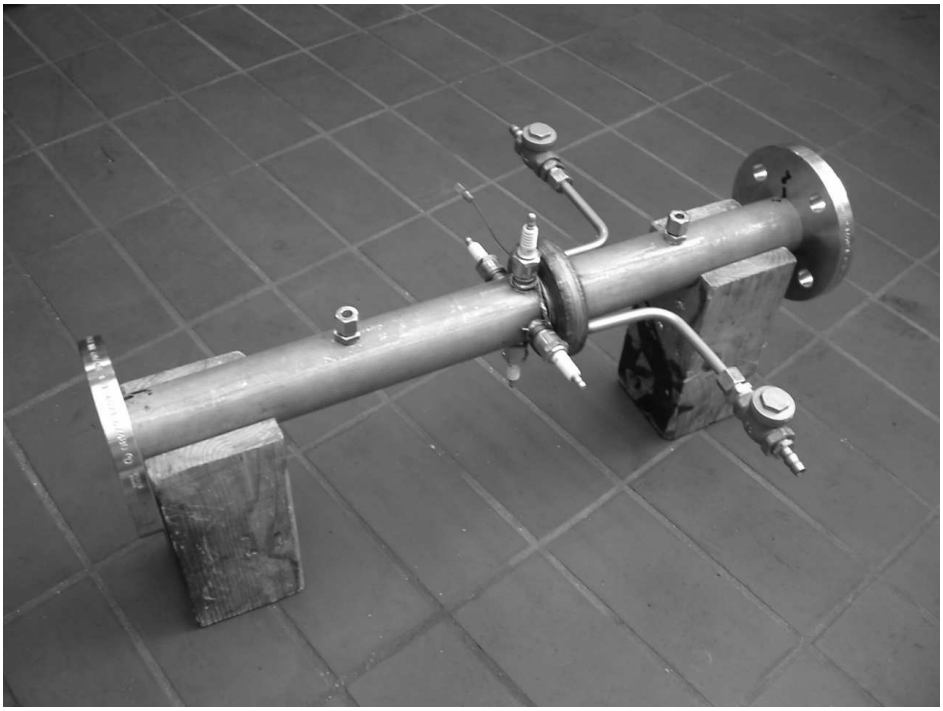

Figure 5.11 : Photo of the finished up-scaled swirl-burner, thermocouples not installed.

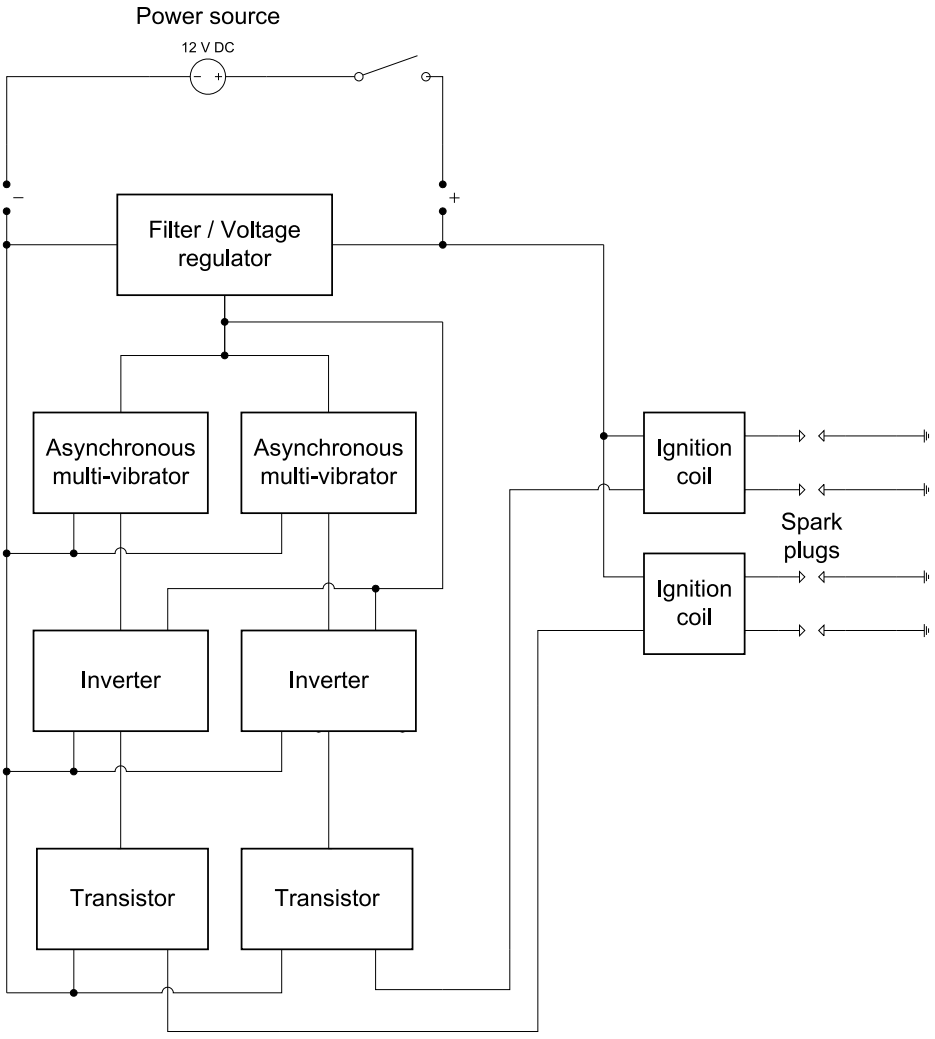

Figure 5.12 : Scheme of the spark-ignition system.

5.6 Functioning on synthetic gas mixture

Before testing the up-scaled swirl-burner on real product gas, it is tested on a synthetic gas mixture of methane, hydrogen and nitrogen. Goal of this test is to verify the working area of the up-scaled version without the introduction of carbon monoxide. Furthermore, the stability results can then be directly compared to the stability results of the small-scale version obtained in section 5.2, which might show whether the working area is a scalable property.

The composition of the synthetic gas-mixture used is deduced from the 18.5 kW product gas measurements given at the end of chapter 4. The LHV and methane/hydrogen ratio for the gas-mixture are chosen similar to the measured product gas: 5 MJ/Nm^3 and 0.5 respectively. The heating value of the CO present in the product gas is replaced by increasing both the amount of methane and hydrogen, while keeping the methane/hydrogen ratio constant. This leads to a hydrogen and methane level of 17.5 and 8.7 vol.% respectively. Although this hydrogen level is high compared to that of the product gas, it is questionable whether the gas will show a large working area as its FHC is just above the lower limits of partial combustion stability in figure 5.7. At a fuel hydrogen content of 17.5 vol.%, burner geometry A only gives stable partial combustion at an air-excess ratio of 0.2 for a fuel power of approximately 500 W. Originally burner A was designed for a power of 2800 W. If the burner working area is fully scalable with the design power, it can be expected that the (20 kW) up-scaled burner becomes unstable at fuel powers above 3.6 kW.

For the stability tests, the up-scaled swirl-burner is mounted in the test-setup between the gasifier and the flare. The synthetic gas-mixture is introduced into the gasifier by use of mass-flow controllers. A continuous flow of gas leaves the gasifier to pass the swirl-burner. Next, the spark ignition is turned on and air is introduced into the swirl-burner. The spark-ignition is turned on before introducing air to the swirl-burner, to prevent creation of a premixed (explosive) mixture. The status of the partial combustion process is determined from temperature measurement by the second thermocouple.

Ignition and extinction of the partial combustion process could be clearly determined, since they are respectively followed by a sharp temperature rise or drop. However, due to inertia of the flow settings, the air-excess ratio at ignition or extinction is expected to contain errors up to a value equal to $\lambda = 0.05$.

The swirl-burner is tested for the minimum air-excess ratio at which partial combustion remains stable at several fuel powers. This is done by igniting the process, and then gradually lowering the air-excess ratio until the partial combustion process extinguishes. At each fuel power tested, the air-excess ratio had to be increased to approximately 0.7 before the process could be ignited, which coincides with the

lower λ-limit of flammability determined in appendix A. This seemingly indicates that ignition of a mixture can be predicted by calculating its flammability limits. However, this may not be concluded, since the process depends on the local mixture fractions, as explained in section 5.2. Ignition at an average λ of 0.7 only indicates that the local mixture fraction at the spark plug positions just reached flammability.

The lower λ-limits of process stability as a function of the fuel power are shown in figure 5.13. It shows that the working area is restricted to low fuel powers. Air-excess ratios of 0.2 could not be reached over the entire power-band. The minimum air-excess ratio that could be reached was 0.3 at fuel powers lower than 3.5 kW. Above that fuel power the minimum air-excess ratio at which partial combustion is still stable increases strongly, probably due to increasing flow velocities (as indicated by the Reynolds number on the upper horizontal axis).

The maximum fuel power at which partial combustion at the minimum air-excess ratio can be maintained is 3.5 kW. This maximum power coincides with the maximum fuel power predicted above. This shows similarity in the stability of the original burner and its up-scaled version. However, an air-excess ratio of 0.2 could not be reached for the scale-up, due to which the results are not fully scalable. The difference might be caused by several reasons, for example: (1) the absolute velocity increase of a factor of about 2.6, (2) the increased number of air injection holes, (3) the larger air injection holes, or (4) the flow disturbances due to the presence of the spark-plugs. These can all have influence on the partial combustion stability, as the results in section 5.3 showed that small disturbances in the burner geometry can have a significant impact on the process' stability limits.

5.7 Functioning on product gas

The functioning of the up-scaled swirl-burner is now tested on product gas produced by the gasifier. Since the working area of the up-scaled swirl-burner is limited, the gasifier is operated at a fuel power of 3.5 kW. This fuel power is chosen because it is the maximum fuel power at which the up-scaled swirl-burner showed stability at the minimum possible air-excess ratio of 0.3. As shown by Houben [39], partial combustion at an air-excess ratio of 0.3 should strongly decrease any tar content, although the share of cracking and polymerization products will be approximately equal.

However, during the test no ignition of the partial combustion process could be established, i.e. the temperature at the second thermocouple decreased instead of increased when air was introduced. Even at an air-excess ratio of 1.0 the process could not be ignited. Varying the gasifier power between 2.5 kW and 7.0 kW did not bring any improvements.

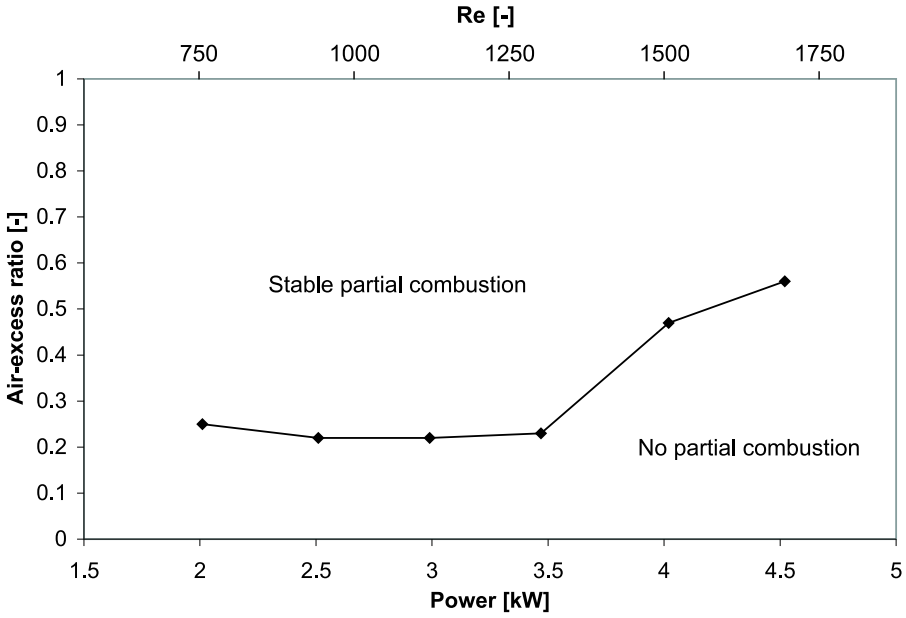

Figure 5.13 : Partial combustion process stability in the up-scaled swirl-burner as a function of fuel power and air-excess ratio for $LHV = 5\,\mathrm{MJ/Nm^3}$ and $FHC = 17.5$ vol.%. Upper horizontal axis shows the Reynolds number in the up-scaled partial combustion burner based on the product gas volume flow with density and dynamic viscosity assumed equal to air at room temperature.

To verify that indeed no partial combustion process took place, the tar content of the product gas before and after the swirl-burner is determined by the Solid Phase Adsorption (SPA) method described in chapter 4. Two tar samples were collected, one at the inlet and one at the outlet of the swirl-burner for a gasifier power of 7.0 kW and a partial combustion at $\lambda = 0.3$. The chromatograms obtained during analysis of the samples are shown in figure 5.14. It shows that the tar species found in the outlet are exactly the same as those found in the inlet. The relative concentrations of species within each sample is similar. The absolute concentrations of the measured species differs for the inlet and outlet sample, which is probably a consequence of dilution of the tar concentration by air addition in the swirl-burner. Since both chromatograms show the same species in the same relative concentrations, it can be concluded that indeed no partial combustion took place.

5.8 Consideration ignition failure

Contrary to the synthetic gas mixture, real product gas could not be ignited in the up-scaled swirl-burner. The ignition failure during the test on product gas could either be caused by the fuel-oxidizer mixture, or by the ignition source. If a spark plug creates a spark in an oxidative environment, combustion reactions can proceed if the mixture fraction is within the flammability limits. The flammability limits thus give

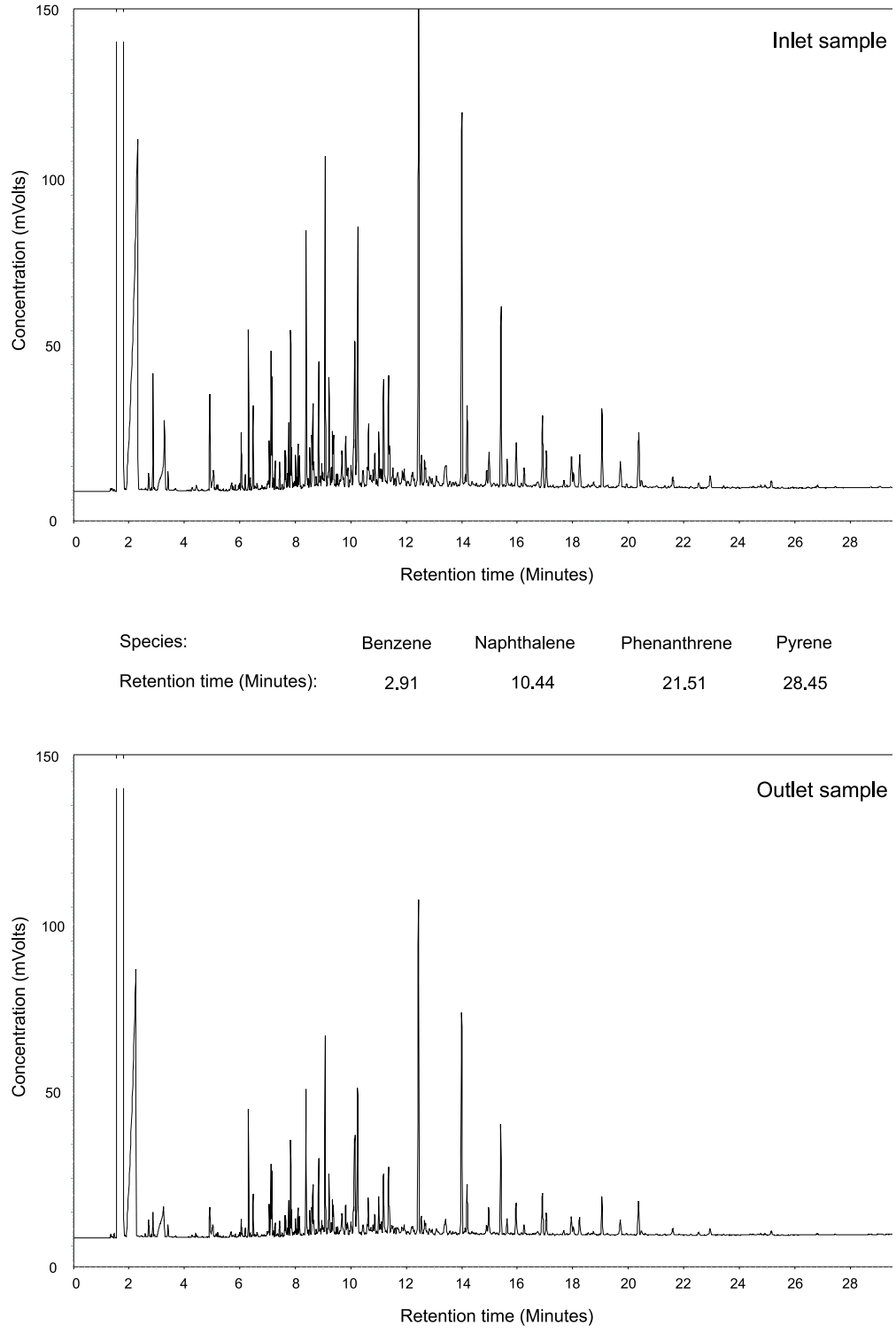

Figure 5.14 : Chromatograms obtained by FID-analysis of tar samples taken at the swirl-burner inlet and outlet. Each peak shows the concentration of certain species defined by their respective retention time. Retention times of the smallest 1-ring (Benzene), 2-ring (Naphthalene), 3-ring (Phenanthrene), and 4-ring (Pyrene) species are given. The first massive peak shown represents the solvent used to dissolve tar from the s.p.a. columns.

an idea of the tendency of a mixture to be ignited by a spark plasma. Sometimes the ignitability limits are mentioned to be narrower than the flammability limits. However, the ignitability limits are determined by the source of ignition while the flammability limits are determined by the mixture [14].

Appendix A indeed shows that the flammability of the product gas is more restricted than that of the synthetic gas mixture. However, since the product gas had a temperature of approximately 200 °C, its flammability limits were actually wider than the calculated ones. This means that either the mixture fraction at the spark-plugs did not get within the flammability limits during the product gas test, or the ignition system did not work properly. Studying the ignition system should help in determining the cause of ignition failure.

Ignition system

Observation of the spark plugs after the product gas test showed that the electrode-tips were still relatively clean compared to the rest of the spark-plugs, as shown in figure 5.15. This indicates that plasma formation occurred during the test, that kept the spark plug electrodes clean from tar. However, this does not mean that the plasma created by the spark plug is strong enough to cause fuel ignition.

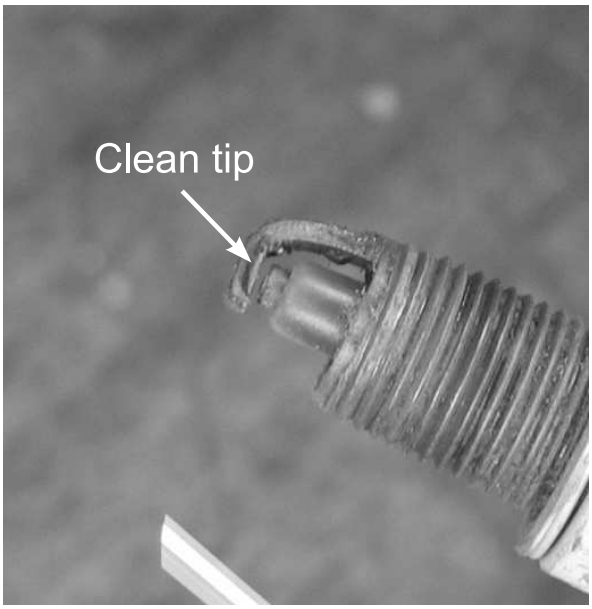

Figure 5.15 : Spark-plug from up-scaled swirl-burner after product gas test.

A plasma between spark plug electrodes is created due to the loss of the dielectric properties of a gaseous insulator as a result of application of an electric field greater than a certain critical magnitude. The critical magnitude of electric field at which the breakdown of a material takes place is called the dielectric strength of the material (or breakdown voltage). The dielectric strength in a certain application

depends on a lot of factors, such as the specimen thickness, the electrode shape, the rate of the applied voltage increase, the shape of the voltage versus time curve, surface condition, gas pressure, etc [7]. However, for electrode gaps $> 10^{-2}$ cm at atmospheric pressure and room temperature [3], typical dielectric strength of most gases are known as a fraction of the dielectric strength of nitrogen, as shown in table 5.2.

Table 5.2 : Dielectric strengths of gases as a fraction of the dielectric strength of nitrogen.

Gas	N_2	O_2	Air	H_2	CH_4	CO	CO_2
Dielectric strength [7]	1.00	0.92	0.97	0.50	1.00 - 1.13	1.02 - 1.05	0.82 - 0.88

Because the dielectric strength of air is almost equal to the dielectric strength of nitrogen and oxygen times their respective volume fraction, it is assumed that the dielectric strength of a gas-mixture can be determined by multiplying the dielectric strengths of its components by their volume fractions. The dielectric strengths of the synthetic and product gas-mixtures can then be determined to be approximately 0.92 and 0.97 respectively. This means that a plasma is created by the spark plugs a little earlier in the synthetic gas-mixture than in the product gas, but the differences are very minute. Further, the dielectric strength only indicates at which electric field strength the plasma can be created, but does not give any information on the temperature or the electron energy in the plasma itself. These plasma data are hard to determine since they depend on the kind of plasma, the kind of gas, the current, the plasma energy dissipation, the temperature of the electrons, etc.

Although the plasma strength in the used gas-mixtures cannot be determined, the dielectric strength of the mixtures indicate that both mixtures are equally prone to plasma creation by the spark plugs. Since the spark duration is of the order of milliseconds, it can be assumed that in both gases thermal plasmas are created [68], which should generate a temperature high enough to ignite any flammable mixture. The ignition failure is thus probably not a consequence of a failing ignition system.

Discussion ignition failure

It shows that the flammability limits of the product gas are relatively narrow. Therefore, the creation of a flammable mixture at the spark plugs becomes less likely, due to which the mixture is more prone for ignition failure. Ignition of product gas in the up-scaled swirl-burner can probably be improved by widening its flammability range. For example, the product gas produced at 18.5 kW is already flammable above $\lambda = 0.6$, as shows from appendix A. The lower λ-limit of a proper product gas is thus even lower than that of the synthetic gas mixture, because of which ignition should be less problematic (if the spark plugs are positioned correctly).

Considering the results for partial combustion of the synthetic gas mixture, it becomes likely that if the product gas would have been ignited, the partial combustion

process would probably also have been stable at lower air-excess ratios than the one at ignition. This, due to the formation of local flammable mixture fractions near the air injection holes.

5.9 Conclusions

Experiments show that the working area of partial combustion in the micro-scale swirl-burner is restricted by the fuel power, the fuel lower heating value and the fuel hydrogen content. Increasing the fuel power, decreasing LHV, and decreasing FHC, irrevocably leads to flame instabilities and eventually to flame and process extinction. Partial combustion of a 5 MJ/Nm^3 gas in the original swirl-burner design (without its diverging top), only gives stable flames for a fuel power of 500 W and a FHC larger than 20 vol.%. At higher fuel powers, the flames only stay stable if the FHC increases to its maximum value. By increasing the air-excess ratio, process stability can probably be maintained at lower FHC.

The process stability shows hardly influenced by the swirl-burner geometry, although swirl and tilt angles and small air injection holes slightly improve the stability. The working area of partial combustion with the present swirl-burner design is thus limited to low fuel powers and high fuel hydrogen contents. Since the fuel power has such a profound effect on the process stability, it becomes likely that the stability limits are partly determined by the physical flow velocity and patterns.

Testing an up-scaled version of the original micro-scale swirl-burner on a synthetic gas mixture, showed that stable partial combustion again only occurred at low fuel power or high air-excess ratio. Testing the same burner on product gas did not show any partial combustion at all due to an ignition failure. The product gas did probably not ignite because the local mixture fraction at the spark plugs did not reach flammability. This lack of flammability at the spark plugs is probably caused by both the low lower heating value of the product gas and the mixing patterns in the burner.

Increasing the lower heating value of the product gas would stimulate ignition. However, in the present test-setup this would not be a solution, since the fuel power needs to be increased to increase the product gas lower heating value. As shown in the tests, an increasing fuel power leads to worse process stability in the swirl-burner.

Concluding, there are two basic problems that prevent partial combustion of product gas in the up-scaled swirl-burner: (1) ignition of the product gas, and (2) partial combustion stability. The first problem seems to be very dependent on the gas composition and on the local mixture fractions at the ignition source. The second problem shows to be dependent on the fuel power and the air-excess ratio, and

probably also on the mixture fractions. Both problems are thus dependent on the velocity of flow and on the flow patterns in the burner. Therefore, the up-scaled swirl-burner is sensitive to its main flow settings and its geometric properties. In the next chapter an attempt to improve its design, using these findings, will be made.

Chapter 6

Redesign of partial combustion burner

The swirl-burners used in the previous chapter showed weak process stability as a consequence of their design. To improve the working area of partial combustion, a new partial combustion burner is designed. The design process of the new burner is described in sections 6.1 and 6.2. A micro-scale partial combustion burner is constructed and tested to study whether its process stability has improved compared to the swirl-burner design, which is described in sections 6.3 and 6.4. The stability and working area of the new burner are analyzed and discussed in section 6.5. Based on this stability analysis, an up-scaled partial combustion burner is designed to fit in the gasifier test-setup, which is described in section 6.6.

6.1 Fundamental burner design

The process stability of the swirl-burner design is relatively low, as already shown in chapter 5. The low process stability is thought to be caused by a combination of effects such as cooling and dilution of the combustion process, gas combustion properties, and complex flow and mixing patterns. A new partial combustion burner is designed to overcome some of the listed problems.

The new burner design is based on the two-step partial combustion mechanism as hypothesized in chapter 3. The hypothesis states that tar cracking by partial combustion occurs by the influence of free radicals and high temperatures caused by combustion of part of a product gas stream at a relatively high air-excess ratio. This implies that, ideally, the new burner should combust part of the product gas at a relatively high air-excess ratio, after which the reaction products are mixed with the rest product gas to start conversion reactions. Therefore, the new burner design should ideally contain a combustion and a conversion zone as schematically shown in figure 6.1.

To avoid complex 3D flow behaviour, the new burner is designed to have a central axi-symmetric combustion zone. Process stability is stimulated by physically separating the combustion zone from the rest product gas. By using a well-defined combustion zone, negative effects by dilution of the combustion zone are prevented.

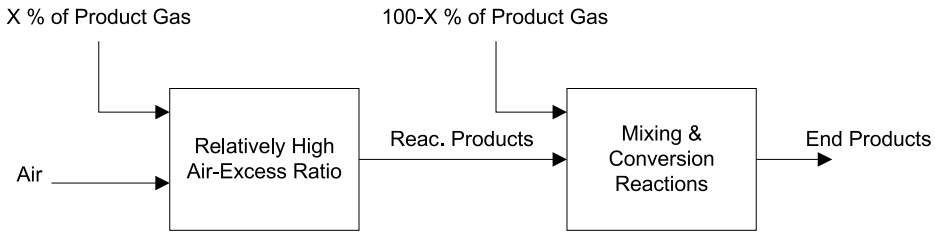

Figure 6.1 : Scheme of hypothetically ideal partial combustion process

Further, the local mixture fractions can as such be better controlled, which should lead to a better understanding of the tar conversion process. Based on these design criteria, and on practical experience gained using the previous burner design, the design demands for the new burner become:

- Axi-symmetry in the combustion zone
- Combustion zone separated from mixing zone
- Efficient mixing zone
- Simple design
- Easy construction
- Low flow obstruction
- No sensitivity to fouling

A relatively simple burner design that satisfies all these demands is shown in figure 6.2. Product gas that flows into the burner is divided into two streams, a combustion zone stream and a bypass stream. The combustion zone is physically separated from the bypass by placement of a separation wall in the form of a tube. Air is fed to the combustion zone by a central air feed pipe. Since the gases are non-premixed and fed axi-symmetrically, a stable jet diffusion flame is likely created. The reaction products of the combustion zone are mixed with the bypass stream in the mixing zone, which starts once the separation tube ends. To create an effective mixing of the rest-product gas and the reaction products of the combustion zone, swirl-inducers are placed at the end of the bypass. Because the total pipe flow area is only minimally decreased by the inserted air feed pipe and combustion zone separation tube, the flow obstruction is minimal. This minimal blockage should help in minimizing burner fouling. Since this burner design complies with the design demands, it is chosen as the new burner geometry.

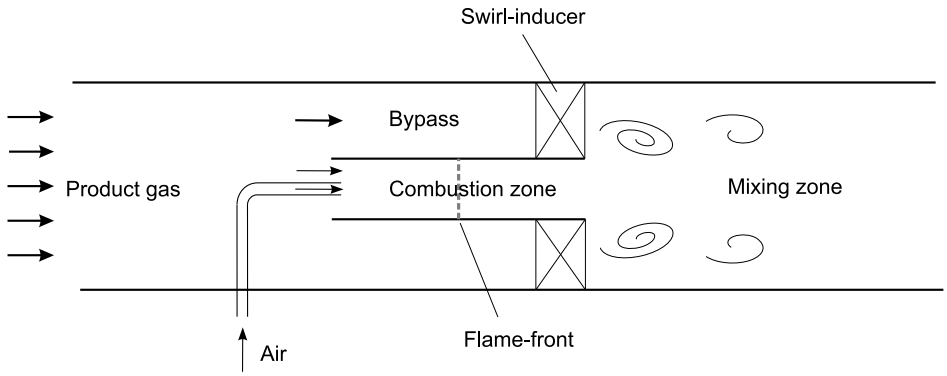

Figure 6.2 : 2D axi-symmetric design of new partial combustion burner. The indicated flame-front is only a schematic representation.

6.2 Burner dimensioning

To dimension the new burner design, the necessary flow area ratio of the combustion zone and the bypass needs to be determined. For that, the mass-flux ratio of the combustion zone stream $\dot{m}_{\mathrm{comb-in}}$ and the bypass stream $\dot{m}_{\mathrm{bypass}}$ is determined using the design air-excess ratios over the combustion zone and the total burner. Based on the experimental results shown in figure 1.3, the air-excess ratio over the total burner is chosen to be 0.2. According to Houben [40] this air-excess ratio should give best tar reduction, although this result is not supported by the computations in chapter 3. For process stability it is chosen to operate the combustion zone at stoichiometry ($\lambda = 1.0$). These air-excess ratios are obtained if $1/5$ of the total product gas flow passes the combustion zone, which gives a mass-flux ratio of:

$$\frac{\dot{m}_{\mathrm{comb-in}}}{\dot{m}_{\mathrm{bypass}}} = \frac{1}{4}. \tag{6.1}$$

The necessary amount of air in the combustion zone is fixed by the fuel composition. As design fuel, the product gas composition measured in chapter 4 at 18.5 kW is chosen (7 vol.% H_2, 3 vol.% CH_4, 25 vol.% CO, 10 vol.% CO_2, 10 vol.% H_2O and 45 vol.% N_2, assuming all unmeasurables are water vapor). Stoichiometric combustion of one mole of this product gas necessitates 0.22 mole O_2. This molar ratio leads to a mass-flux ratio of oxygen over product gas of approximately 0.27. Since the mass fraction of oxygen in air approximates 0.23, the necessary mass-flux of air $\dot{m}_{\mathrm{air}}$ becomes:

$$\dot{m}_{\mathrm{air}} = 1.2 \cdot \dot{m}_{\mathrm{comb-in}}. \tag{6.2}$$

The product gas flows over the combustion zone and the bypass come from a single product gas stream, and combine in the mixing zone to again form a single stream. Therefore, the pressure drops over the combustion zone Δp_{comb} and the bypass $\Delta p_{\mathrm{bypass}}$ should be equal:

$$\Delta p_{\mathrm{bypass}} = \Delta p_{\mathrm{comb}}. \tag{6.3}$$

Based on equations 6.1, 6.2, and 6.3, and using equations for the pressure drops over the bypass and the combustion zone, the necessary flow area ratio $\frac{A_{\text{comb-in}}}{A_{\text{bypass}}}$ is determined to be 0.8. A detailed description of the calculation is given in appendix B.

6.3 Experimental burner construction

Based on the flow area ratio of 0.8, a new-design micro-scale partial combustion burner has been constructed. This partial combustion burner is used to test the partial combustion process stability and the working area of the new burner design. The tests are again performed in the experimental setup described in section 5.1.

The new micro-scale burner is basically constructed of three tubes, as shown in figure 6.3: (1) an outer tube to define the outer burner diameter, (2) an inner tube which forms the separation wall between the bypass and the combustion zone, and (3) an air feed tube. To the outside of the inner tube, four 45° swirl-vanes are attached, which radially fix the inner tube in the center of the outer tube. The inner tube is fixed longitudinally in the outer tube by resting it on two small pins protruding the outer tube-wall. The air feed tube penetrates the outer tube longitudinally from a position upstream, to release its air at the center of the inner tube bottom.

The outer tube and the air feed tube are longitudinally and radially positioned by a 'burner base'. The burner base is also used to close the burner at the bottom, and to provide synthetic product gas to the burner. Two product gas feed lines protrude the burner base opposite of each other to obtain a reasonable homogeneous product gas flow in the outer tube. All burner base connections are made leak-free by using copper-paste.

Choosing the dimensions of the three main tubes finishes the micro-scale burner design. Due to limitations in the experimental setup, the air feed pipe outer diameter is restricted to 8 mm. It is chosen to combine this outer diameter with a standard wall thickness of 1 mm. The diameters of the inner and outer tube are subsequently chosen to approximate the necessary $\frac{A_{\text{comb-in}}}{A_{\text{bypass}}}$-ratio of 0.8. The choice for equal product gas and air velocity made in appendix B,has been relaxed in favor of availability of materials to obtain the correct $\frac{A_{\text{comb-in}}}{A_{\text{bypass}}}$-ratio. The outer diameter and wall thickness of the outer tube have been chosen 28 mm and 2 mm respectively. The outer diameter and wall thickness of the inner tube have been chosen 18 mm and 1.15 mm respectively. Assuming the combustion zone inlet area equal to the separation tube inner area minus the air feed pipe outer area, gives a $\frac{A_{\text{comb-in}}}{A_{\text{bypass}}}$-ratio of 0.72. Using the volumetric flows calculated in appendix B, the inlet flow areas, and assuming the air and product gas densities equal, the air injection velocity u_{air} becomes approximately 6.1 times the product gas velocity $u_{\text{comb-in}}$ at the combustion zone inlet.

The length of the outer tube could maximally be 200 mm due to setup limitations. The length of the inner tube is subsequently chosen 60 mm, which should be long enough for stable combustion, but short enough to lead free radicals into the mixing zone. The top of the inner tube is positioned 40 mm below the top of the outer tube.

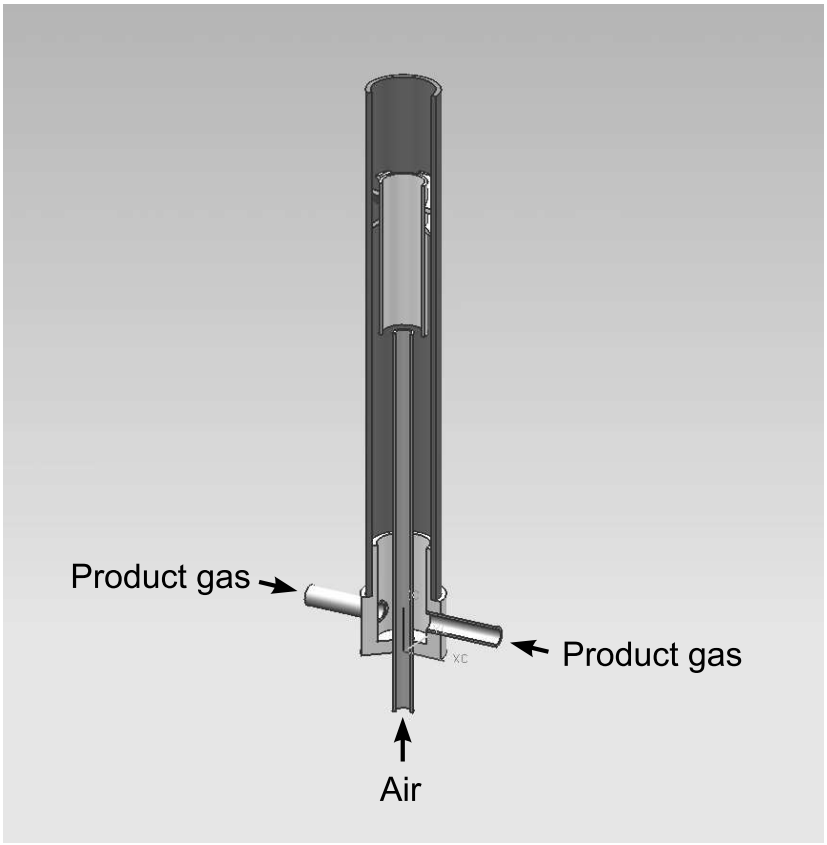

Figure 6.3 : 3D representation of the new partial combustion burner for the micro-scale setup. Pins protruding outer pipe to support the separation (inner) tube are not shown.

6.4 Partial combustion stability

The working area tests as a function of the fuel hydrogen content and fuel power for fixed lower heating value as described in section 5.2, are repeated for the new-design micro-scale partial combustion burner. The limiting fuel power for stable partial combustion at $\lambda = 0.2$ is determined as a function of the fuel hydrogen content, over a fuel power range of 500 to 2800 W. The fuel again consists of a $CH_4/H_2/N_2$-mixture with a LHV of 5.0 MJ/Nm^3. The combustion process is initiated at low fuel power and high air-excess ratio, after which the fuel and oxidizer settings are slowly altered to the desired working point. The stability results are shown in figure 6.4.

It shows that partial combustion at high FHC gives a good process stability over the entire fuel power range. The stability remains good while lowering the FHC until at a certain moment a critical FHC (FHC_{crit}) is reached, at which the partial combustion process immediately extinguishes. FHC_{crit} shows to depend on the fuel power, as it is equal to 22 vol.% H_2 for a fuel power of 2800 W, but stretches to 15 vol.% H_2 for a fuel power of 500 W. The critical FHC shows to increase non-linearly with the fuel power to a seemingly maximum of FHC = 22 vol.%.

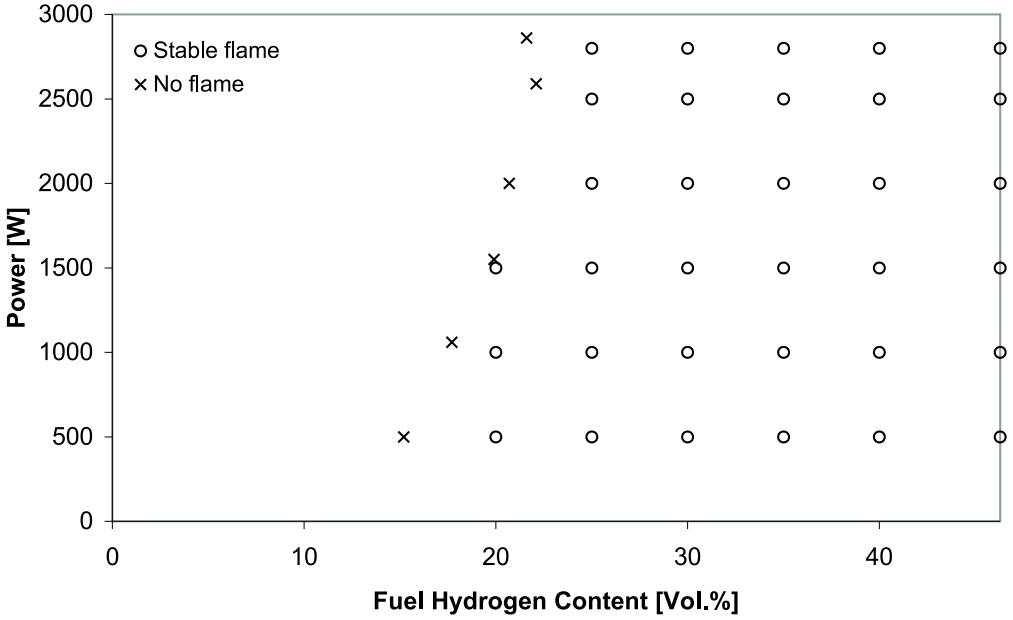

Figure 6.4 : Flame stability of the new burner geometry as a function of fuel hydrogen content and fuel power for λ = 0.2 and LHV = 5 MJ/Nm^3.

Compared to the results for the micro-scale swirl-burner (see figure 5.7), the stability of the new partial combustion burner has improved. Stable partial combustion can be attained over a larger working area. There is especially an increased stability at high fuel powers for medium to high fuel hydrogen contents. However, the stability at low fuel hydrogen content has slightly decreased. In the next section a consideration is given on the gas combustion properties and the burner design, to explain the trend of FHC_{crit} as a function of the fuel power.

6.5 Consideration of flame extinction

Flame extinction at the critical fuel hydrogen content occurs rapidly without any signalling. FHC_{crit} increases slightly with increasing fuel power, which indicates two things. First, the stability limit seems to be mainly determined by the fuel composition and thus by the fuel combustion properties. Second, because FHC_{crit} slightly increases with fuel power, FHC_{crit} is probably influenced by changing flow charac-

teristics inside the burner, such as increasing flow velocities. To verify these two indications, the extinction behaviour of jet flames and the fuel combustion properties of the synthetic product gas are studied.

6.5.1 Jet flames

The situation as designed in the partial combustion burner, is similar to nonpremixed jet flames. In literature nonpremixed jet flames are extensively discussed, often describing a central fuel jet with or without an annular air flow. The situation in the combustion zone is equal to a central air jet with an annular fuel flow. These two situations can probably be directly compared, since the reaction mechanisms, diffusion, and flow patterns are similar. Possibly, the position of the flame-front differs. To study whether the FHC-limits can be improved by geometry optimization, the stabilization mechanisms and blow off criteria for double concentric burners with, (1) a central tube with small wall thickness, and (2) a central tube surrounded by a bluff-body, are studied in appendix C.

From the appendix it shows that above thin-walled concentric burners triple flames are probably formed. The most important characteristic of a triple flame is the triple point. The triple point is formed on the premixed contour of stoichiometry, where the heat release of combustion balances the heat losses (to for example the burner base). Since the fuel and oxidizer are diffusively premixed between the burner base and the triple point, both on the rich and on the lean side of the triple point wings are formed that extend to their respective flammability limits. Together with the triple point, the two wings form a curved flame front. Downstream of the triple point, a diffusion flame is formed along the contour of stoichiometry.

The triple point propagates against the premixed fuel/oxidizer flow with a flame propagation velocity U_f. Because the triple flame can deflect the flow upstream due to its heat release, the flame propagation velocity can be higher than the mixture laminar burning velocity S_L. The U_f/S_L ratios noted in literature vary between almost 1 to the order of 3, depending on the flame curvature. If the flow velocity at the triple point rises above U_f, the flame is blown off.

The triple flame stability, and thus the partial combustion burner stability, seem to depend on the air and product gas velocities and on the flame propagation velocity. Appendix C shows that the influence of the co-flow velocity on the flame characteristics is much larger than that of the jet velocity, since the co-flow determines the entire velocity field surrounding the flame, while the jet just determines the fuel/oxidizer mixing. However, in the partial combustion burner the central jet velocity is approximately 6.1 times higher than the co-flow velocity, due to which the above stated argument might become dubious. The average flow velocities in the partial combustion burner can be readily calculated from the experimental settings

and the burner dimensions, as has been partly done in appendix B. To determine whether the critical FHC are formed due to the flow velocities rising above the flame propagation velocities, the flame propagation velocities still have to be estimated.

6.5.2 Laminar burning velocity

As shows from the previous section, the propagation velocity of a double concentric diffusion flame rises above the laminar burning velocity of a mixture. However, the maximum flame velocity ratio U_f/S_L seems to be limited at 3. The flame propagation velocity can thus be estimated by calculating the laminar burning velocity S_L. Therefore, the laminar burning velocity of the fuel used in the experiments has been calculated as a function of the fuel hydrogen content.

The program Chem1D has been used to calculate the laminar burning velocities of the gas-mixtures used in the experiments. Chem1D is a highly flexible program developed for simulating the combustion of a fuel/oxidizer mixture [77]. The laminar burning velocity S_L has been calculated for an adiabatic flat flame at atmospheric pressure and a temperature of 293 K. The DRM-19 model is used as the reaction mechanism, which is a reduced version of the GRI-Mech 1.2 and contains 21 chemical species and 84 reversible reactions [47]. Although DRM-19 is a reduced reaction mechanism, it is suitable for calculation of laminar burning velocities. The transport model used is the mixture averaged diffusive transport model, in which the diffusion coefficients of single species are based on their diffusion in the average mixture. In the transport mechanism, the heat transport caused by concentration and pressure gradients, and the species diffusion caused by temperature and pressure gradients are neglected. These assumptions are allowed because of the large nitrogen concentrations in the mixture [65].

The calculated laminar burning velocities for premixed $CH_4/H_2/N_2$-mixtures at a LHV of 5.0 MJ/Nm^3 as a function of the fuel hydrogen content are shown in figure 6.5 for air-excess ratios of 1.0 and 0.6. It shows that the laminar burning velocity strongly decreases as FHC decreases. At $\lambda = 1.0$, the velocity decreases from 120 cm/s at pure hydrogen/nitrogen to approximately 8 cm/s at pure methane/nitrogen. The large amount of nitrogen in the gas clearly has a decreasing effect on the laminar burning velocity compared to pure methane or pure hydrogen situations with a S_L of approximately 36 cm/s and 215 cm/s respectively [57]. The decreasing effect on the burning velocity becomes even stronger for combustion at low air-excess ratio, as shown by the results for $\lambda = 0.6$.

Since S_L, and thus U_f, strongly decrease with decreasing FHC, the presence of a critical FHC might be caused by the flow velocities rising above U_f (assuming that a triple flame is formed in the combustion zone).

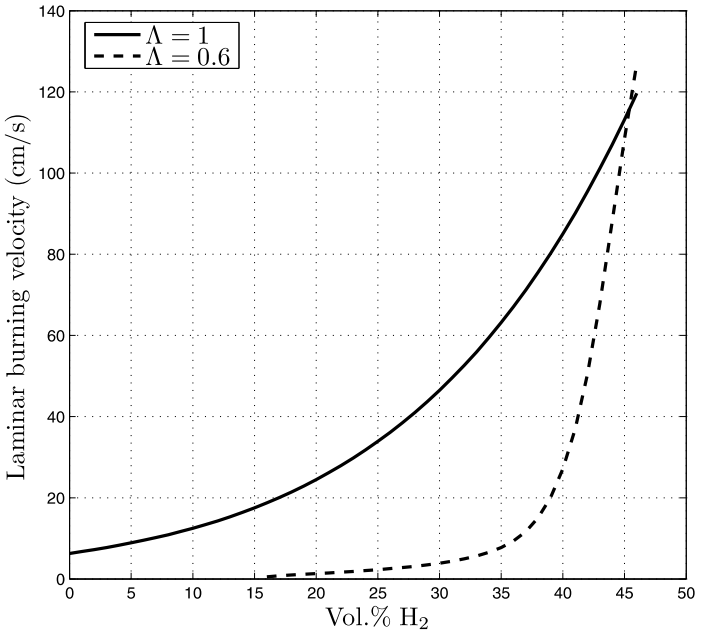

Figure 6.5 : The laminar burning velocity for a $CH_4/H_2/N_2$-mixture at 5.0 MJ/Nm^3 as a function of the fuel hydrogen content as calculated by Chem1D.

To estimate the values of U_f/S_L in the experimental setup, the laminar burning velocity and flow velocities as a function of the fuel power or *FHC* have to be related. The laminar burning velocities at each critical *FHC* can be found in figure 6.5, and are shown in table 6.1. The air and product gas velocities at the combustion zone inlet u_{air} and $u_{comb-in}$ can be calculated using the volumetric flow data in appendix B and the flow areas (that can be derived from the experimental burner dimensions). If it is shortly assumed that the flow velocity at the triple point is equal to half the sum of u_{air} and $u_{comb-in}$, the ratio of the assumed triple point velocity u_f over the laminar burning velocity, u_f/S_L, can be determined (as shown in table 6.1).

Table 6.1 : The laminar burning velocity S_L, and the flow velocities $u_{comb-in}$ of product gas at the combustion zone inlet, u_{air} of air at its injection point, u_f of the product gas / air mixture at the assumed triple point position, and the u_f/S_L ratio as a function of the fuel power and its matching critical fuel hydrogen content FHC_{crit}.

Fuel power [W]	500	1000	1500	2000	2500	2800
FHC_{crit} [vol.%]	15	18	20	21	22	22
S_L [m/s]	0.18	0.21	0.25	0.26	0.28	0.28
$u_{comb-in}$ [m/s]	0.14	0.28	0.42	0.56	0.70	0.78
u_{air} [m/s]	0.85	1.70	2.54	3.39	4.24	4.75
u_f [m/s]	0.50	0.99	1.48	1.98	2.47	2.77
u_f/S_L [-]	2.8	4.7	5.9	7.6	8.8	9.9

The u_f/S_L ratios shown in table 6.1 are relatively high compared to the maximum U_f/S_L ratio of 3 stated in literature [25]. However, this maximum is found for diluted methane flows at stoichiometry with an equal jet and co-flow velocity. It is argued that other fuels have other maxima due to a changing inertia of the upstream mixture. As the inertia of the fuel mixture decreases with increasing FHC, the maximum U_f/S_L ratio would become higher. Further, as shows from table 6.1, the air jet velocity is considerably higher than the fuel annular velocity. Consequently, a nonuniform velocity profile is created, which undoubtedly influences the maximum U_f/S_L ratio. Further, if u_f had been assumed different, the calculated ratio could have significantly changed for the better.

The calculations at least show that u_f/S_L is of the same order of magnitude as the maximum U_f/S_L. Therefore, it becomes likely that the burning velocities and the flow velocities indeed strongly influence the critical FHC.

6.5.3 Discussion flame extinction

The existence of the critical FHC found in the experiments is explained by the flame formation, the gas combustion properties, and the flow velocities. Since the combustion zone of the new partial combustion burner can be compared to a thin-walled co-annular tube combustion, it is likely that triple flames are formed. These flames can be blown off if the flow velocities become higher than the flame propagation velocities. The flame propagation velocity is a mixture and a flow/mixing property, and thus depends on FHC and the fuel power. It has been shown that the flow velocities and the flame front propagation velocity are of the same order of magnitude, which supports the theory of flame extinction due to the flow velocities exceeding U_f.

The working area of partial combustion in the new burner can probably be improved by decreasing the local flow velocity at the triple point, and by increasing the fuel's laminar burning velocity. The local flow velocity can be decreased by increasing the flow areas in the burner, or by decreasing the fuel power. The laminar burning velocity can be increased by choosing a fuel with a low methane content and a high hydrogen content. Replacing the methane by carbon monoxide probably already brings a considerable improvement in the working area, because of a higher laminar burning velocity, as shown in figure 6.6.

Further, as described in appendix C, flame stability in the partial combustion burner can probably be increased by creation of a recirculation zone at the central tube top. The recirculation zone can form a continuous ignition source for the jet flame, which delays blow-off. A recirculation zone can be created by increasing the tube wall thickness, or by adding a bluff-body at the central tube top.

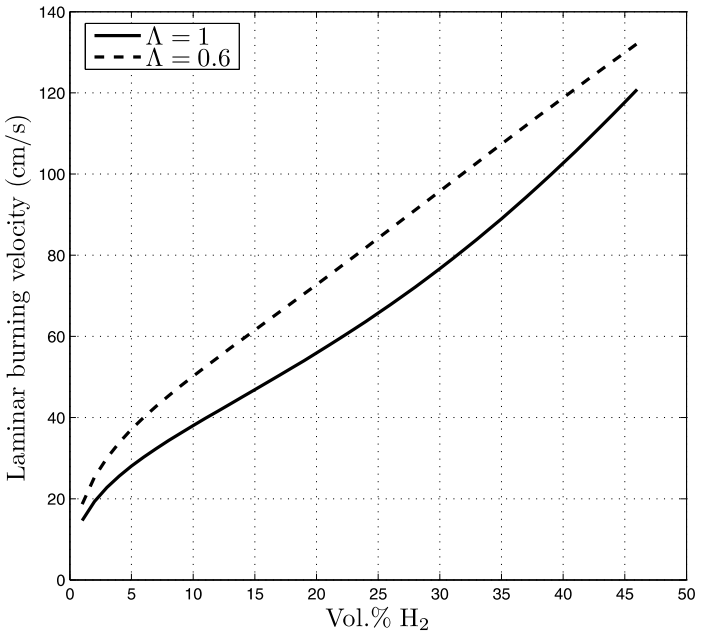

Figure 6.6 : The laminar burning velocity for a $CO/H_2/N_2$-mixture at 5.0 MJ/Nm^3 as a function of the fuel hydrogen content as calculated by Chem1D.

6.6 Scale-up of new partial combustion burner

The micro-scale new-design partial combustion burner shows such a working area improvement compared to the micro-scale swirl-burner, that it is also scaled up to fit the experimental gasifier setup. Compared to the micro-scale partial combustion burner, the up-scaled burner is designed to have lower average flow velocities and a higher central tube wall thickness. These measures, based on the conclusions from the previous section, should improve partial combustion stability past that of the micro-scale version.

The lowest laminar burning velocity of any 5 MJ/Nm^3 methane/hydrogen/nitrogen-mixture at stoichiometry is approximately 8 cm/s, as shown in figure 6.5. Since U_f/S_L seems limited at 3 for stability, the up-scaled burner is designed for an average product gas flow velocity of 24 cm/s. For process stability the air velocity is chosen equal to that of the product gas.

A 20 kW product gas flow with a LHV of 5 MJ/Nm^3, gives a volume flow of $4.0{\cdot}10^{-3}$ Nm^3/s. Assuming the product gas density equal to that of air at standard conditions, the total volume flow of air becomes $9.6{\cdot}10^{-4}$ Nm^3/s, using equations 6.1, 6.2 and $\dot{m} = \rho u A$.

The total air flow area A_{air} then has to become equal to $9.6{\cdot}10^{-4}$ / 0.24 = $4.0{\cdot}10^{-3}$ m^2, which necessitates an inner air feed pipe diameter of 71.4 mm. It is chosen to use a pipe with an outer diameter of 80 mm and a wall thickness of 4 mm.

Under the assumption that $\rho_{air}=\rho_{product-gas}$ and $u_{air}=u_{product-gas}$, equation 6.2 leads to a combustion zone inlet area $A_{comb-in}$ of $3.3{\cdot}10^{-3}$ m^2. Adding this area to the area taken by the central tube, the necessary inner diameter of the separation tube becomes 103.1 mm. Based on availability, it is chosen to use a pipe with an outer diameter of 108 mm and a wall thickness of 2 mm.

Using the necessary flow area ratio $\frac{A_{comb-in}}{A_{bypass}}$ of 0.8, the bypass area A_{bypass} becomes equal to $4.2{\cdot}10^{-3}$. This flow area leads to an inner diameter of the bypass pipe of 130.2 mm. Based on DIN-standardization, a NW125 pipe is chosen with an outer diameter of 139.7 mm and a wall thickness of 2 mm.

For construction and operation purposes, it is chosen to construct the burner of three separate parts, as shown in figure 6.7: (1) an inlet part containing the air feed pipe, (2) a middle part containing the separation tube and the swirl vanes, and (3) an outlet part. The three parts are bolted together by NW125 flanges, one on each part. Advantage of the three-part construction is that the burner can be constructed relatively easy, and that each part can be easily removed, changed or cleaned. Disadvantage of this construction is that the three NW125 flanges dissipate a lot of heat, by which heating the burner becomes harder.

The bypass pipe has a large diameter compared to the product line of the experimental setup. Therefore, reducers are necessary on the inlet and the outlet part. To simplify the burner construction, the inlet and outlet parts are designed to have an equal geometry. Both parts subsequently consist of a NW40 flange, a reducer, a Ø139.7 mm pipe with length 240 mm, and a NW125 flange, all welded together. The only difference between both parts is that the inlet part also houses the air feed pipe. The air feed pipe is constructed of two equal parts, one axially releasing the air into the burner, and the other perpendicularly penetrating the reducer wall as shown in figure 6.8.

The middle part is fixed between the inlet and outlet parts. In this part the swirl vanes are used to position the separation tube, by having them welded on one side to the NW125 flange, and on their other side to the separation tube. To induce a swirling motion on the gases at the bypass exit, the swirl vanes are positioned under an angle of 45° to the main stream. 20 swirl vanes are used to cover the entire bypass area. The separation tube starts at the same burner cross-section as the air feed pipe ends, and extends to the downstream edge of the middle NW125 flange. The length of the separation tube becomes 120 mm. The present separation tube length and average flow velocity, give a residence time of air and product gas in the separation tube of approximately 0.5 seconds.

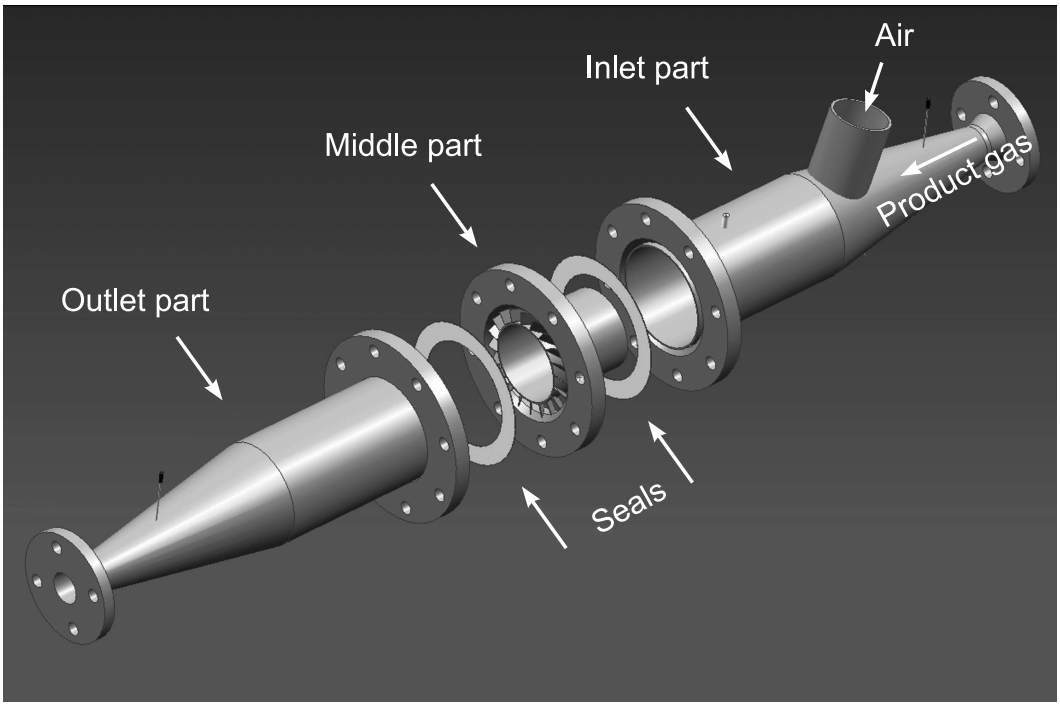

Figure 6.7 : Explosion of up-scaled partial combustion burner.

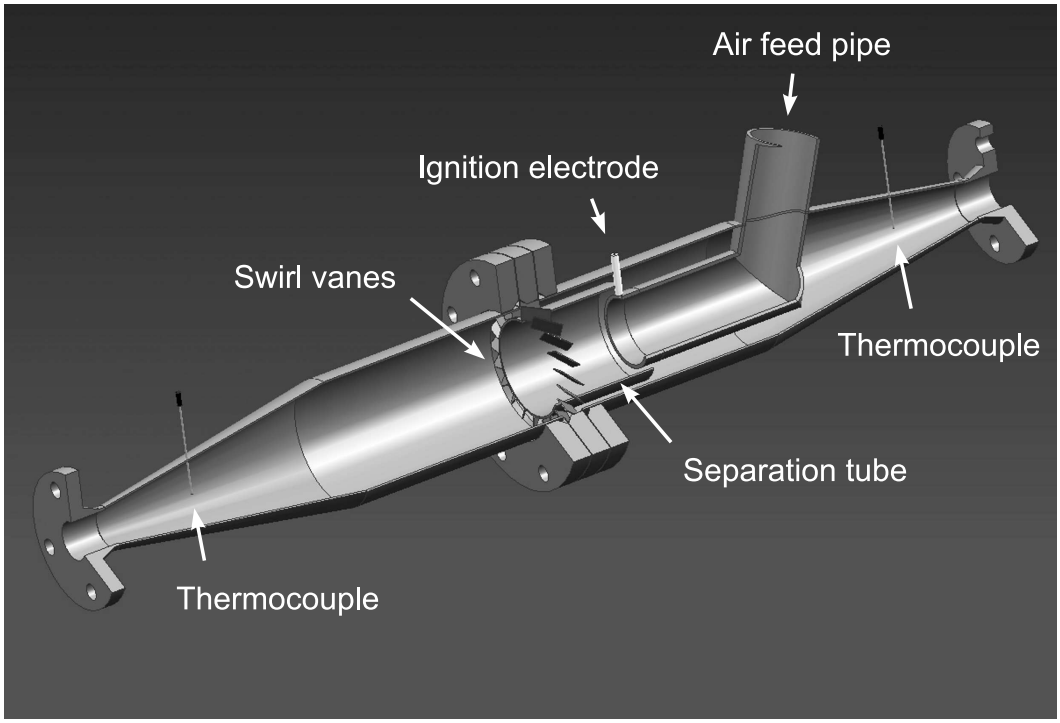

Figure 6.8 : Cut-open of up-scaled partial combustion burner.

A single electrode is used to ignite the partial combustion process. The electrode is positioned in the fuel/air mixing region just downstream of the air feed pipe wall. Sparks are created in the fuel/oxidizer mixing zone by plasma formation between the electrode and the air feed pipe. Due to the burner design, the creation of a flammable mixture near the ignition-electrode is relatively independent of the flow settings. To determine ignition of the partial combustion process, two thermocouples are used to measure the product gas temperature upstream and downstream of the air addition, just as used in the up-scaled swirl-burner.

6.7 Conclusions

It shows that by constructing a new design partial combustion burner the working area of partial combustion can be considerably stretched compared to the original micro-scale swirl-burner design. Partial combustion above a critical fuel hydrogen content is very stable over a large fuel power range. The stretch is probably a consequence of the newly designed separated combustion zone. In this combustion zone part of the product gas can combust at stoichiometry without the possibility of dilution by the rest fuel. Further, the combustion process has been stabilized by creating a co-annular jet diffusion flame. The critical fuel hydrogen content is probably caused by the decreasing laminar burning velocity with decreasing FHC, which eventually leads to flame blow-off. The critical FHC can probably be shifted to lower FHC by lowering the average flow velocities, adding a bluff-body at the central tube top, and by combusting a fuel with a higher laminar burning velocity. The results are incorporated into the design of an up-scaled new design partial combustion burner.

Chapter 7

Conclusions

7.1 Conclusions

Partial combustion of a tar containing gas mixture in a micro-scale swirl-burner has previously been shown to reduce the tar content of the gas mixture. Tar reduction took place either by cracking or polymerization, depending on the fuel composition and the level of oxidation. Both a high fuel hydrogen content and a low air-excess ratio showed to be beneficial for tar cracking [39]. In this thesis the partial combustion process is studied in detail. In general it is found that next to the chemical tar cracking processes, also the transport processes play a major role in tar cracking by partial combustion, and that the design of a well functioning partial combustor is not trivial.

A literature study of the chemical processes shows that tar cracking takes place under the influence of free radicals, while polymerization takes place by tar accumulation. Tar cracking can be stimulated by increased free radical production. In the swirl-burner, free radicals are likely locally produced during local combustion of part of the fuel at high air-excess ratio. After production, the free radicals are mixed with the uncombusted fuel to cause tar cracking. This means that tar cracking by partial combustion is a two-step process, in which a combustion zone produces free radicals that cause tar cracking in a conversion zone. This two-step chemical behaviour is indeed confirmed by a one-step homogeneous reactor model. Another two-step reactor model, shows that both the production of free radicals as their maximum residence time, can be increased by increasing the fuel hydrogen content and/or the air-excess ratio of combustion. Both an increasing fuel hydrogen content and air-excess ratio thus probably lead to increased contact between free radicals and tar, due to which they should both lead to increased tar cracking.

In earlier experiments it was indeed found that an increasing fuel hydrogen content lead to increased tar cracking. However, they also showed that an increasing air-excess ratio lead to tar polymerization instead of tar cracking. This result does not correspond with the conclusions on the chemical processes. It is concluded that this discrepancy is probably a result of physical transport processes in the partial combustion process. If transport processes like diffusion and turbulent mixing are

taken into account, the fuel/oxidizer mixture fraction is far from homogeneous. Since the mixture fraction has a profound effect on the chemical processes, the transport processes probably partly determine the tar conversion.

In fact, the chemical and transport processes probably both have to be considered simultaneously. In a two-step combustion/conversion process, free radicals produced in the combustion process have to be mixed with the uncombusted fuel before their numbers are decreased. Therefore, the physical mixing time-scales should be of the order of the chemical time-scales of radical production. Ideally, the combustion process produces free radicals without any interference by physical transport, after which the free radicals are instantaneously mixed with the uncombusted fuel. It is likely there exists an optimum balance between the chemical and transport process time-scales.

In partial combustion stability experiments it is found that flame stability is a limiting factor for partial fuel combustion. Literature showed that process stability is likely lost when the physical flow velocity at the flame-front exceeds the maximum flame-front propagation velocity. The flame front propagation velocity depends on the local mixture gradient determined by transport processes, and on the laminar burning velocity determined by the fuel composition. Partial combustion stability should therefore, and is indeed experimentally found to, increase with decreasing flow velocities and increasing fuel laminar burning velocity. Calculation of fuel laminar burning velocities shows they are strongly increased by increasing fuel hydrogen content. Therefore, a high fuel hydrogen content again shows beneficial for partial combustion.

Shortly, this thesis shows that (1) the chemical processes and the transport processes cannot be decoupled in describing the tar cracking process by partial combustion, (2) a rising fuel hydrogen content is always beneficial for increased tar cracking, by increased reaction rates, increased free radical production, and increased radical residence times, and (3) to obtain tar cracking, the local air-excess ratio should be carefully controlled.

To obtain best tar cracking by partial product gas combustion, the product gas should have a high fuel hydrogen content. The gasifier test-setup designed and used in this thesis for partial combustion experiments on real product gas, however, produced product gas with a low hydrogen content. This is concluded to be caused by the heat losses being relatively high compared to the heat release. Due to the low fuel hydrogen contents of the product gas produced, it has become questionable whether tar cracking by partial combustion can be achieved at all in the present gasifier test-setup.

Designwise, the original swirl burner shows inferior. Experiments show that the partial combustion stability is limited to low fuel powers and high fuel hydrogen contents. Further, ignition of the partial combustion process shows to depend on the formation of local mixture fractions, and thus on the process settings. A newly designed partial combustion burner, based on the two-step combustion/conversion principle, shows increased stability as a consequence of a clearly defined combustion zone. Advantage of the new burner is that the combustion and conversion processes are clearly separated, because of which its functioning can be better studied or predicted. However, it has not yet been shown whether the new burner is capable of converting tar.

If tar reduction by partial product gas combustion is to become a success, the product gas should contain a lot of hydrogen, and the partial combustion burner should have a clear combustion zone with controlled air-excess ratio. The product gas hydrogen content is dependent on the gasification process, which should be controlled towards hydrogen production. The controlled combustion zone is dependent on the partial combustion burner design.

7.2 Recommendations

During the study towards understanding the behaviour of partial fuel combustion for tar reduction, a lack of several kinds of information was experienced. Based on this experience, recommendations are given.

It appears that the combustion properties of the fuel to partially combust, can be quite relevant with respect to flame stability. Up to now, mainly methane/hydrogen/nitrogen-mixtures have been studied, of which the laminar burning velocity, the free radical production, the residence time of free radicals, and the flammability limits showed important properties. For a better understanding of partial product gas combustion, the same properties should be known for the product gas. Therefore, these properties should be studied in more detail for varying gas compositions, including real product gases.

Further, it showed disadvantageous to don't know the physical flow patterns in the partial combustion burners. Since the transport processes seem equally important to tar cracking as the chemical processes, it is recommended to study the flow patterns inside the partial combustion burner in detail. Especially, the time-scales of the fuel/oxidizer mixing processes with respect to the chemical time-scales seem to be important for tar conversion. It is most interesting to relate changing flow patterns to their effect on tar conversion. In studying the flow patterns, it is probably necessary to take the combustion effects such as flow deflection and density changes

into account.

Further, there is yet too little information about tar cracking under varying circumstances. The fuel power, fuel lower heating value, fuel composition, air-excess ratio, partial combustion burner design, tar content, and tar concentrations are probably all of importance for the tar conversion process. Therefore, their influence should be studied in more detail. This seems to be a precondition for better understanding of tar cracking by partial combustion.

Last, the constructed gasifier probably produces too little hydrogen for tar cracking by partial product gas combustion. Therefore, the gasifier should be adapted to produce more hydrogen. Partial combustion can then be tested for tar conversion in the upscale new-design partial combustion burner. The new burner design makes it especially attractive to test the dependence of tar cracking on the chemical time-scales and transport time-scales by altering the combustion zone length.

Appendix A

Flammability limits

Flammability limits refer to the limit amount of combustible gas capable of bringing flammability on a gas/air-mixture. Mixtures within these limits liberate enough energy on combustion to ignite the neighboring layer of unburned mixture, and therefore are capable of self-propagation of flame. It can be understood that as the mixture temperature is higher, the limits should be stretched because less heat is necessary for heating up the mixture. Next to the temperature, in practice the flammability limits of a particular gas mixture are affected by the pressure, direction of flame propagation, and surroundings [83]. When a source of heat of sufficient size and intensity is introduced into a mixture outside the flammability limits, still some combustion occurs. However, this combustion is extinguished as the influence of the source of ignition is lost [14].

The flammability limits of any $H_2/CO/CH_4/CO_2/N_2$-mixture can be calculated using a method described by Coward [14]. The method pairs of the flammable gases with the inert gases to give a series of dissected mixtures. The limits of each dissected mixture are read from figure A.1. The limits L of the total mixture are then calculated using

$$L = \frac{100}{\sum_{i=1}^{n} \frac{p_i}{N_i}}, \tag{A.1}$$

where i is a dissected mixture, n is the number of dissected mixtures, p the proportion of dissected mixture i in percentages, and N the respective upper or lower limit of the dissected mixture. The method is stated to be accurate within 2 to 3 percent.

Cowards method has been used to determine the flammability limits of three synthetic gas mixtures at a LHV of 5.0 MJ/Nm^3, among which a mixture with FHC = 0 vol.%, a mixture with FHC = 46.3 vol.%, and the mixture used in section 5.6 with FHC = 17.5 vol.%. Further, the flammability limits of the product gases obtained in chapter 4 are determined. In determining the flammability limits of the product gases, the concentrations of all unmeasurable components and all O_2 measured are assumed to be N_2, otherwise Cowards method cannot be used. The calculated flammability limits are listed in table A.1 in volume percentages L, and in the corresponding air-excess ratios λ.

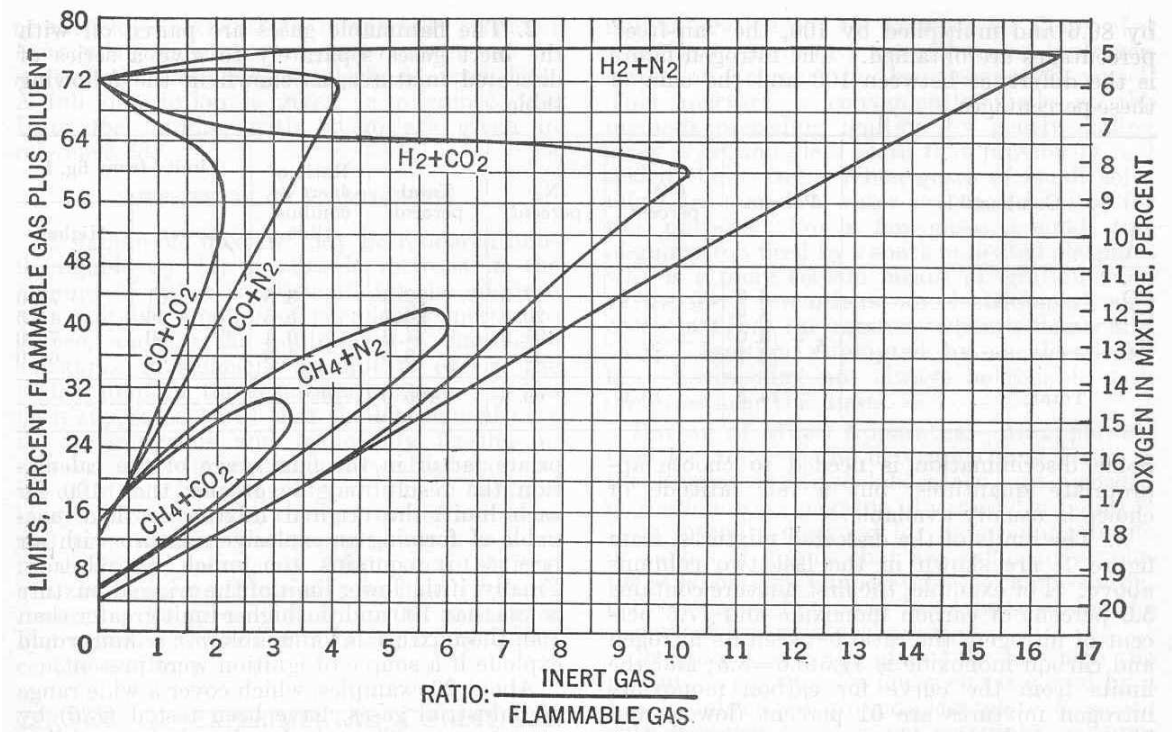

Figure A.1 : Limits of flammability of hydrogen, carbon monoxide, and methane containing various amounts of carbon dioxide and nitrogen [14].

Table A.1 : Flammability limits of several gas mixtures used throughout the thesis.

Gas composition						Flammability limits			
H_2 [vol.%]	CH_4 [vol.%]	CO [vol.%]	CO_2 [vol.%]	N_2 [vol.%]	LHV [MJ/Nm^3]	L_{upper} [vol.%]	L_{lower} [vol.%]	λ_{lower} [-]	λ_{upper} [-]
0.0	13.9	0.0	0.0	86.1	5.0	not flammable			
17.5	8.7	0.0	0.0	73.8	5.0	54	17	0.7	3.9
25.0	6.4	0.0	0.0	68.6	5.0	57	14	0.6	5.1
46.3	0.0	0.0	0.0	53.7	5.0	74	9	0.3	9.2
4.0	1.7	14.0	14.0	66.3	2.8	66	46	0.9	2.0
7.0	3.0	25.0	10.0	55.0	5.0	62	24	0.6	3.0

Appendix B

Partial combustion burner dimensioning

In figure 6.3 a new partial combustion burner design is given, which is redrawn schematized in figure B.1. In the burner a product gas stream is divided over a combustion zone and a bypass. In the combustion zone an amount of air is introduced, which is used to combust the product gas present in the combustion zone. In this appendix, the necessary ratio of the combustion zone inlet area $A_{\text{comb-in}}$ and the bypass inlet area A_{bypass} is determined based on design demands.

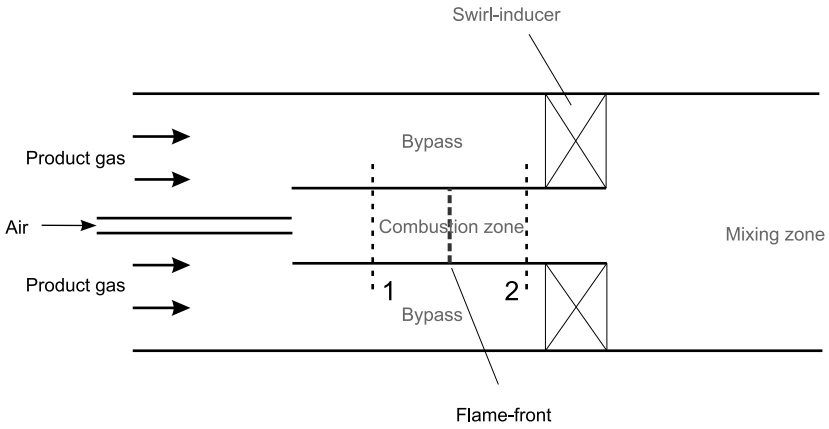

Figure B.1 : Schematic representation of the new design partial combustion burner.

A design demand formulated in chapter 6 is that the ratio of the mass-fluxes over the combustion zone $\dot{m}_{\text{comb-in}}$ and the bypass $\dot{m}_{\text{bypass}}$ is fixed at:

$$\frac{\dot{m}_{\text{comb-in}}}{\dot{m}_{\text{bypass}}} = \frac{1}{4}. \tag{B.1}$$

Another design demand is that the mass-flux of air $\dot{m}_{\text{air}}$ is related to the mass-flux over the combustion zone $\dot{m}_{\text{comb-in}}$ according to:

$$\dot{m}_{\text{air}} = 1.2 \cdot \dot{m}_{\text{comb-in}}. \tag{B.2}$$

Further, it is given that the pressure drops over the combustion zone Δp_{comb} and over the bypass Δp_{bypass} are equal:

$$\Delta p_{\text{bypass}} = \Delta p_{\text{comb}}. \tag{B.3}$$

The flow area ratio $\frac{A_{\text{comb-in}}}{A_{\text{bypass}}}$ can now be calculated by determining the pressure drops over the combustion zone and the bypass. In determining these pressure drops, the wall friction effect is disregarded for several reasons. First, the combustion zone and the bypass are approximately of the same length, and the gas properties and flow velocities in both paths are similar (up to the flame front at least). Therefore, the pressure drop by wall friction in the combustion zone and the bypass will probably be of the same order of magnitude. Second, taking the pressure drop by wall friction into account strongly complicates the pressure drop calculations due to its dependency on the Reynolds number. Finally, the dimensioning process is at best only a rough approximation of reality.

Neglecting any wall friction effects, the pressure drop over the bypass Δp_{bypass} is formed by the pressure loss over the swirl-vanes. This pressure loss can be described using a single loss factor K_{bypass} according

$$\Delta p_{\text{bypass}} = \tfrac{1}{2} K_{\text{bypass}} \cdot \left(\rho u^2\right)_{\text{bypass}}, \tag{B.4}$$

in which ρ is the product gas density, and u the local flow velocity.

Neglecting any wall friction effects, the pressure loss over the combustion zone Δp_{comb} becomes equal to the sum of the pressure losses over the combustion zone entrance, over the flame-front, and over the combustion zone exit. The pressure losses over the combustion zone entrance $\Delta p_{\text{comb-in}}$ and exit $\Delta p_{\text{comb-out}}$ can again be determined using single loss factors K according

$$\Delta p_{\text{comb-in,comb-out}} = \tfrac{1}{2} K_{\text{comb-in,comb-out}} \cdot \left(\rho u^2\right)_{\text{comb-in,comb-out}}. \tag{B.5}$$

The pressure loss over the flame-front is a consequence of the temperature rise, which implies a decrease in density and an increase in velocity and momentum of the stream. According to Cohen et al. [13] this leads to a pressure loss. For one-dimensional incompressible frictionless flow in a duct of constant cross-sectional area A, the momentum equation becomes

$$A \cdot (p_2 - p_1) + \dot{m} \cdot (u_2 - u_1) = 0, \tag{B.6}$$

in which p is the local pressure, $\dot{m}$ is the local mass-flux, u is the local velocity, and where subscripts 1 and 2 denote the positions before and after the flame-front as indicated in figure B.1. The local mass-flux is equal to $(\rho u)_{\text{comb}}$ times the flow area A. Since $(\rho u)_{\text{comb}} = (\rho u)_{\text{comb-in}} + (\rho u)_{\text{air}} = (\rho u)_{\text{comb-out}}$, the pressure loss over the flame-front Δp_{ff} becomes

$$\Delta p_{\text{ff}} = (\rho u)_{\text{comb-out}} \cdot (u_{\text{comb-out}} - u_{\text{comb-in}}), \tag{B.7}$$

assuming that the air entrance velocity is equal to the product gas velocity in the combustion zone entrance, because of which the average flow velocity before the flame front is equal to the product gas entrance velocity $u_{\text{comb-in}}$.

The velocity difference over the flame-front is determined by the density change of the product gas. According to [29], for incompressible flows the density variation of a gas with temperature is equal to:

$$\frac{\rho_1}{\rho_2} = \frac{p_1}{p_2} \cdot \frac{T_2}{T_1}. \tag{B.8}$$

If it is shortly assumed that the flame-front is positioned transverse on the combustion zone wall and the pressure before and after the flame-front is equal, the density ratio becomes purely dependent on the gas temperatures. Stoichiometric combustion of the design product gas (defined in section 6.2) with an initial temperature of 473 K, leads to an approximate adiabatic combustion temperature of 2000 K according to PSR1 of the two-step PSR-model described in chapter 3. The temperature rise thus leads to a density ratio $\frac{\rho_{\mathrm{comb-in}}}{\rho_{\mathrm{comb-out}}}$ of 4.2. Consequently the velocity ratio becomes:

$$\frac{u_{\mathrm{comb-out}}}{u_{\mathrm{comb-in}}} = 4.2. \tag{B.9}$$

The total pressure loss over the combustion zone thus becomes:

$$\begin{aligned} \Delta p_{\mathrm{comb}} = & \\ & \tfrac{1}{2} K_{\mathrm{comb-in}} \cdot \left(\rho u^2\right)_{\mathrm{comb-in}} + \\ & \tfrac{1}{2} K_{\mathrm{comb-out}} \cdot \left(\rho u^2\right)_{\mathrm{comb-out}} + \\ & (\rho u)_{\mathrm{comb-out}} \cdot (u_{\mathrm{comb-out}} - u_{\mathrm{comb-in}}) \,. \end{aligned} \tag{B.10}$$

Combining equations B.3, B.4, and B.10, and multiplying every entry by the total flow area A_{tot} gives:

$$\begin{aligned} & \tfrac{1}{2} K_{\mathrm{bypass}} \cdot \left(\rho u^2\right)_{\mathrm{bypass}} \cdot A_{\mathrm{bypass}} \cdot \frac{A_{\mathrm{tot}}}{A_{\mathrm{bypass}}} = \\ & \quad \tfrac{1}{2} K_{\mathrm{comb-in}} \cdot \left(\rho u^2\right)_{\mathrm{comb-in}} \cdot A_{\mathrm{comb-in}} \cdot \frac{A_{\mathrm{tot}}}{A_{\mathrm{comb-in}}} + \\ & \quad \tfrac{1}{2} K_{\mathrm{comb-out}} \cdot \left(\rho u^2\right)_{\mathrm{comb-out}} \cdot A_{\mathrm{comb-out}} \cdot \frac{A_{\mathrm{tot}}}{A_{\mathrm{comb-out}}} + \\ & \quad (\rho u)_{\mathrm{comb-out}} \cdot (u_{\mathrm{comb-out}} - u_{\mathrm{comb-in}}) \cdot A_{\mathrm{comb-out}} \cdot \frac{A_{\mathrm{tot}}}{A_{\mathrm{comb-out}}}. \end{aligned} \tag{B.11}$$

Since $\dot{m} = \rho u A$, equation B.11 can be written as:

$$\begin{aligned}\tfrac{1}{2}K_{\text{bypass}} \cdot \dot{m}_{\text{bypass}} \cdot \frac{u_{\text{bypass}}}{u_{\text{comb-in}}} \cdot \frac{A_{\text{tot}}}{A_{\text{bypass}}} = \\ \tfrac{1}{2}K_{\text{comb-in}} \cdot \dot{m}_{\text{comb-in}} \cdot \frac{A_{\text{tot}}}{A_{\text{comb-in}}} + \\ \tfrac{1}{2}K_{\text{comb-out}} \cdot \dot{m}_{\text{comb-out}} \cdot \frac{u_{\text{comb-out}}}{u_{\text{comb-in}}} \cdot \frac{A_{\text{tot}}}{A_{\text{comb-out}}} + \\ \dot{m}_{\text{comb-out}} \cdot \left(\frac{u_{\text{comb-out}}}{u_{\text{comb-in}}} - 1 \right) \cdot \frac{A_{\text{tot}}}{A_{\text{comb-out}}}.\end{aligned} \tag{B.12}$$

Since $A_{\text{comb-in}}$ is equal to $A_{\text{comb-out}}$, dividing every entry in equation B.12 by $\dot{m}_{\text{comb-in}} \cdot \frac{A_{\text{tot}}}{A_{\text{comb-in}}}$ leads to:

$$\begin{aligned}\tfrac{1}{2}K_{\text{bypass}} \cdot \frac{\dot{m}_{\text{bypass}}}{\dot{m}_{\text{comb-in}}} \cdot \frac{u_{\text{bypass}}}{u_{\text{comb-in}}} \cdot \frac{A_{\text{comb-in}}}{A_{\text{bypass}}} = \\ \tfrac{1}{2}K_{\text{comb-in}} + \\ \tfrac{1}{2}K_{\text{comb-out}} \cdot \frac{\dot{m}_{\text{comb-out}}}{\dot{m}_{\text{comb-in}}} \cdot \frac{u_{\text{comb-out}}}{u_{\text{comb-in}}} + \\ \frac{\dot{m}_{\text{comb-out}}}{\dot{m}_{\text{comb-in}}} \cdot \left(\frac{u_{\text{comb-out}}}{u_{\text{comb-in}}} - 1 \right).\end{aligned} \tag{B.13}$$

As $\dot{m}_{\text{comb-out}}$ is equal to the sum of $\dot{m}_{\text{comb-in}}$ and $\dot{m}_{\text{air}}$, combining equations B.1, B.9, and B.13 leads to:

$$\begin{aligned}\tfrac{1}{2}K_{\text{bypass}} \cdot 4 \cdot \frac{u_{\text{bypass}}}{u_{\text{comb-in}}} \cdot \frac{A_{\text{comb-in}}}{A_{\text{bypass}}} = \\ \tfrac{1}{2}K_{\text{comb-in}} + \\ \tfrac{1}{2}K_{\text{comb-out}} \cdot \left(1 + \frac{\dot{m}_{\text{air}}}{\dot{m}_{\text{comb-in}}} \right) \cdot 4.2 + \\ \left(1 + \frac{\dot{m}_{\text{air}}}{\dot{m}_{\text{comb-in}}} \right) \cdot 3.2.\end{aligned} \tag{B.14}$$

As given before, $\dot{m} = \rho u A$. Since the product gas density at the bypass and the combustion zone entrance are equal, equation B.1 leads to:

$$\frac{u_{\text{bypass}}}{u_{\text{comb-in}}} = 4 \cdot \frac{A_{\text{comb-in}}}{A_{\text{bypass}}}. \tag{B.15}$$

Combining equations B.2, B.14, and B.15, leads to:

$$\tfrac{1}{2}K_{\text{bypass}} \cdot 16.0 \cdot \frac{A^2_{\text{comb-in}}}{A^2_{\text{bypass}}} = \tfrac{1}{2}K_{\text{comb-in}} + \tfrac{1}{2}K_{comb-out} \cdot 9.2 + 7.0, \tag{B.16}$$

and subsequently to:

$$\frac{A^2_{\text{comb}-\text{in}}}{A^2_{\text{bypass}}} = \frac{\frac{1}{2}K_{\text{comb}-\text{in}}+4.6\cdot K_{\text{comb}-\text{out}}+7.0}{8.0\cdot K_{\text{bypass}}}. \tag{B.17}$$

The loss factors of the combustion zone entrance $K_{\text{comb}-\text{in}}$ and the combustion zone outlet $K_{\text{comb}-\text{out}}$ are estimated to be equal to 1, based on the standard indicative loss factors for a re-entrant inlet and an exit in open space [43]. According to [80], the loss factor over the bypass K_{bypass} is equal to

$$K_{\text{bypass}} = \frac{k_w}{2\cos^2\theta}, \tag{B.18}$$

in which k_w is a constant depending on the swirl-vane form, and θ the angle of the swirl-vanes. Straight swirl-vanes (k_w = 1.3), and a swirl-vane angle of 45° lead to a loss factor K_{bypass} of 2.6.

The necessary flow-area ratio $\frac{A_{\text{comb}-\text{in}}}{A_{\text{bypass}}}$ thus becomes 0.8.

Validation of omission wall friction effects

In determining the flow area ratio, it is assumed that the wall friction effects do not considerably contribute to the pressure drops over the combustion zone and the bypass. The validity of this assumption is estimated here using the partial combustion burner dimensions defined in section 6.3. Both for the bypass as the combustion zone successively their volumetric flow rates $\dot{V}$, flow areas A, average flow velocities $\overline{u}$, Reynolds numbers Re, and friction loss factors K_f are determined. Below the method of calculation is described, and all calculated values can be found in table B.1. In the calculation the influence of the swirl-inducers and the flame front are disregarded.

For a gas with a heating value of 5 MJ/Nm^3, the total volumetric product gas flow $\dot{V}_{\text{productgas}}$ can be directly derived from the fuel power. If it is assumed that $\dot{V}_{\text{productgas}}$ is divided over the bypass and the combustion zone according to equation B.1, the product gas volume flow over the bypass $\dot{V}_{\text{bypass}}$ and the combustion zone $\dot{V}_{\text{comb}-\text{in}}$ can be derived. Following equation B.2, the total volume flow of air $\dot{V}_{\text{air}}$ is now known, because of which the total summed volume flow over the combustion zone $\dot{V}_{\text{comb}}$ is known.

The average flow velocities can be calculated by dividing $\dot{V}$ by the flow areas A. Using the dimensions given in section 6.3, the bypass flow area A_{bypass} can be determined to be $1.98\cdot10^{-4}$ m^2, and the combustion zone flow area A_{comb} to be $1.94\cdot10^{-4}$ m^2. The calculated average flow velocities $\overline{u}$ are given in table B.1.

The average Reynolds numbers can be determined according:

$$\mathrm{Re} = \frac{\rho \cdot u_{\mathrm{comb-in}} \cdot D_h}{\mu}, \tag{B.19}$$

in which ρ is the gas density, μ is the gas dynamic viscosity, and D_h is the hydraulic diameter of the flow passage. It is assumed that the product gas properties are equal to that of air at room temperature (density ρ = 1.188 kg/m^3, and dynamic viscosity μ = 18.24·10^{-6} Pa·s). The hydraulic diameter of the combustion zone is equal to its inner diameter (0.0157 m). The hydraulic diameter of the bypass can be calculated to be 0.006 m, since it is equal to 4 times the flow area divided by the wetted perimeter. The calculated Reynolds numbers are also shown in table B.1.

It shows that all flow is laminar (Re $<$ 2300), due to which the loss factor K_f become equal to $\frac{64}{\mathrm{Re}} \cdot \frac{L}{D_h}$, in which L is the length of the combustion zone. Since L is known to be 0.060 m, the loss factors can be determined, as shown in table B.1.

Table B.1 : The volumetric product gas flow $\dot{V}_{\mathrm{product_gas}}$, the flow velocity $u_{\mathrm{comb-in}}$ at the combustion zone inlet, the Reynolds number Re, and the loss factor due to wall friction K_f as a function of the fuel power for the new design partial combustion burner defined in section 6.3.

Fuel power [W]	500	1000	1500	2000	2500	2800
$\dot{V}_{\mathrm{product_gas}}$ [m^3/s]	1.0·10^{-4}	2.0·10^{-4}	3.0·10^{-4}	4.0·10^{-4}	5.0·10^{-4}	5.6·10^{-4}
$\dot{V}_{\mathrm{bypass}}$ [m^3/s]	8.0·10^{-5}	1.6·10^{-4}	2.4·10^{-4}	3.2·10^{-4}	4.0·10^{-4}	4.48·10^{-4}
$\dot{V}_{\mathrm{comb-in}}$ [m^3/s]	2.0·10^{-5}	4.0·10^{-5}	6.0·10^{-5}	8.0·10^{-5}	1.0·10^{-4}	1.12·10^{-4}
$\dot{V}_{\mathrm{air}}$ [m^3/s]	2.4·10^{-5}	4.8·10^{-5}	7.2·10^{-5}	9.6·10^{-5}	1.2·10^{-4}	1.344·10^{-4}
$\dot{V}_{\mathrm{comb}}$ [m^3/s]	4.4·10^{-5}	8.8·10^{-5}	1.32·10^{-4}	1.76·10^{-4}	2.2·10^{-4}	2.464·10^{-4}
$\overline{u}_{\mathrm{bypass}}$ [m/s]	0.40	0.81	1.21	1.62	2.02	2.83
$\overline{u}_{\mathrm{comb}}$ [m/s]	0.23	0.45	0.68	0.91	1.13	1.27
$\mathrm{Re}_{\mathrm{bypass}}$ [-]	158	316	474	632	789	884
$\mathrm{Re}_{\mathrm{comb}}$ [-]	232	464	696	928	1161	1300
$K_{\mathrm{f,bypass}}$ [-]	4.1	2.0	1.4	1.0	0.8	0.7
$K_{\mathrm{f,comb}}$ [-]	1.1	0.5	0.4	0.3	0.2	0.2

It shows that the flow in the new partial combustion burner is laminar, due to which the loss factor due to wall friction decreases with increasing fuel power. Compared to the other loss factor determined above, the calculated loss factors due to wall friction are of the same order of magnitude at low fuel power, and an order of magnitude lower at high fuel power. This means that at low fuel power the omission of the wall friction effect affects the flow area ratio calculation considerably, while at high fuel power the omission does not significantly influence the flow area ratio result. The wall friction effect should thus have better be taken into account

for a more precise flow area ratio calculation. However, that would lead to a flow area ratio that is dependent on the Reynolds number, which would complicate any burner design. Since the only goal was to get a rough estimate of the necessary flow area ratio, the omission of the wall friction effect is assumed valid.

Appendix C

Jet flames

The flame situation in the partial combustion burner as designed in chapter 6, is similar to non-premixed jet flames. These flames are extensively discussed in literature. The situations discussed, often describe a central fuel jet with or without an annular air flow. In this appendix, the stabilization mechanisms and blow off criteria are studied for double concentric burners with 1) a central tube with small wall thickness, and 2) a central tube surrounded by a bluff-body.

Tube combustion

From literature [8, 66] it shows that for low central-jet velocities in a thin-walled concentric burner, the flame is attached to the burner and becomes a stable diffusion flame. However, when the central mass flow exceeds a critical value, the base of the diffusion flame lifts off from the burner rim to form a lifted flame. If the central jet flow rises too high, the lifted flame is blown off.

For lifted flames three stabilization mechanisms are observed as indicated in figure C.1: edge flame extinction, triple flame propagation, and flame front propagation [10]. All three mechanisms are basically a consequence of the same process: reactants mixing before the flame-front. Near the burner surface, the increasing heat losses to the surroundings decrease the temperature and the reaction rates [67]. Because near the burner surface the chemical reaction rates are low, and the mixing rates are high due to large concentration gradients of the primary reactants, a small partially premixed region is developed. As the mixture rises, it is increasingly heated by the flame that develops, where the heat release rate balances the heat losses [67].

According to Chen [10], all three stabilization mechanism are basically triple flames, each having different limits. The triple flame front propagation mechanism applies when the centerline mixture fraction is higher than the rich extinction limit. This means that both on the rich and on the lean side of the triple point a premixed flame wing is formed. The wings extend until their respective flammability limit is reached. From the triple point also an upwards diffusion flame develops along the mixture layer of stoichiometry.

Edge flame extinction occurs at minimum lift-off height, where the stoichiometric mixture fraction gradient reaches the extinction limit calculated for stretched diffusion flames in a counterflow geometry. This means that the two wings cannot be developed, and only the diffusion flame is present.

For flame front propagation stabilization, the rich premixed wings of the lifted triple flames merge at jet centerline. A continuous partially premixed flame front is then formed between the two lean flammability limit locations on opposite sides of the jet centerline, with the centerline mixture fraction below the rich flammability limit.

The flame blow-out limit is reached when the triple flame structure breaks down, when the centerline mixture fraction is less than the stoichiometric value.

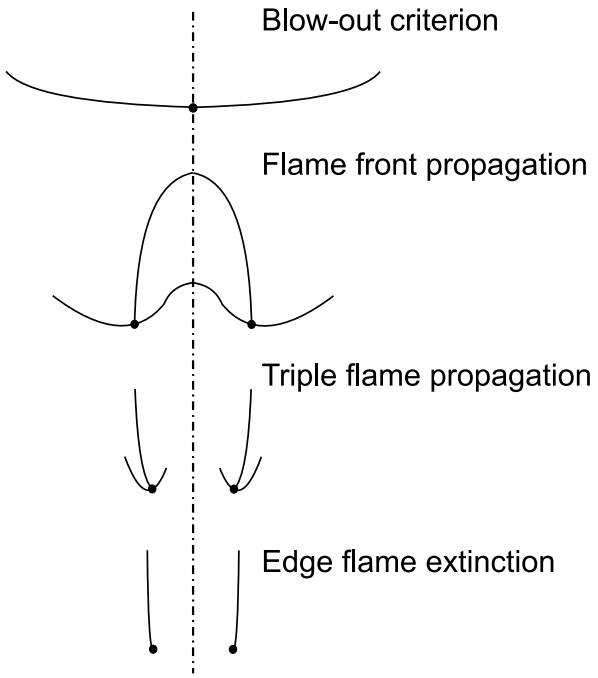

Figure C.1 : Schematic diagram of flame contours and conditions for flame stability and blow-out criteria of a lifted laminar flame in an axisymmetric geometry. A necessary condition for these criteria is the balance between U_f (flame propagation velocity) and U_{st} (the local stoichiometric axial flow velocity) at the stoichiometric triple points, which are indicated by solid circles. [10]

The lifted flame-front structure is that of a curved premixed flame, with a radius of curvature large compared to the flame-front thickness. The curved flame-front propagates against the incoming flow as a quasi-planar premixed flame with a velocity U_f [25]. The magnitude of U_f depends mainly on the curvature of the partially premixed front and the amount of heat released by combustion [8]. The effect of the heat release is the deflection of the flow upstream of the curved front, which has the net result of making the triple-flame propagate faster than S_L, the propagation speed of a fully premixed and planar stoichiometric flame [8]. The curvature, determined

by the rate of strain and the gradient of mixture fraction imposed on it, influences the heat loss and as such also the flame propagation speed [8, 31]. The velocity of the overall triple flame structure is thus greater than the premixed burning velocity. The U_f/S_L ratios noted in literature vary between almost 1 to the order of 3 [8, 25].

The stabilization of a leading edge flame is attributed to the balance between flow divergence effects and heat loss effects. The flame is stabilized in the mixing flow at a location where its effective flame speed matches the flow speed [67]. Consequence is that triple flame stabilization is more related to the fluid dynamic effects of triple flame propagation rather than flame extinction [10]. Thus, the jet initial conditions, such as the jet velocity, the nozzle diameter, the fuel mass fraction at the nozzle exit, and the annular flow velocity, affect flame stability only via the modification of local flow/mixing field [10]. The influence of the jet flow velocity on the flame characteristics is much smaller than the co-flow velocity, since the jet flow velocity influences the mixing between oxidizer and fuel, whereas the co-flow velocity determines the entire velocity field surrounding the flame [66].

Bluff-body combustion

According to Chen [11], the situation for bluff-body burners differs from the lifted flame situation described above. Bluff-body burners have a wide circular disc around a negligibly sized central pipe, with a diameter at least equal to 0.2 times the diameter of the annular pipe: $D_{\text{bluff-body}}/D_{\text{annulus}} \geq 0.2$. Vortex creation at the disc rim is known to play a role for jet flames on a bluff body. The annular flow can entrain part of the central jet into a low-speed recirculation zone region in the wake of the bluff body to form a well-stirred combustible mixture. A stable pilot flame can then be created near the burner exit that can serve as a continual ignition source.

Depending on the annular and jet flow velocities, three characteristic stable modes can be found for bluff body burners: recirculation zone flames, central jet dominated flames, and jet-like flames, as shown in figure C.2. When the central jet momentum is too weak to overcome that of the reverse flows in the recirculation bubble, formation of a stable jet flame is impossible and all the jet mass will be retained behind the bluff body to form a recirculation zone flame (Regime I). When the central jet has a much higher momentum than that of the recirculating flows, the jet vortex may no longer exist behind the bluff body and part of the annular stream can even be entrained downstream into the jet stream. The characteristic mean flow field behind the bluff body is then dominated by the annular vortex, where insufficient jet mass can be captured to reach the flammability limit. Thus, the flame appears jet-like (Regime III). When the jet and annular stream momenta are comparable, a central jet dominated flame (Regime II) can be developed. Combustion occurs both in the recirculation zone and further downstream along the axial axis.

Both the central-jet dominated flames and the jet-like flames become unsteady when the fuel jet velocity exceeds a certain limit. The jet-like flames (Regime III) can be lifted suddenly to a much higher axial position downstream of the recirculation bubble (Regime V), or even blown out directly with a smaller bluff body. This sudden jump is also observed for an attached jet flame lifted from a straight tube of large lip thickness. For the central-jet dominated flames (Regime II), the blue neck flame between the downstream jet and the recirculation zone flames begins to be partially quenched (Regime IV). Both the lifted and the partially quenched flames would be blown out if the jet velocity were to increase further.

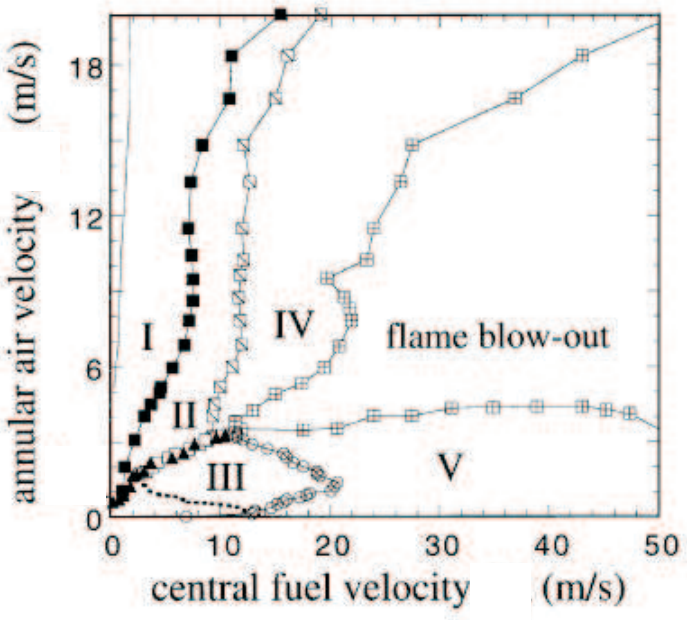

Figure C.2 : Combustion diagram for bluff-body burner with $D_{\text{bluff-body}}/D_{\text{annulus}} = 0.667$. Regime I: recirculation zone flame. Regime II: central-jet dominated flame. Regime III: jet-like flame. Regime IV: partially quenched flame. Regime V: lifted flame. Dashed line and open squares represent reattachment and blow-out limits of lifted flames in hysteresis region. [11]

The limit for conversion from recirculation zone flames to jet dominated flames decreases very quickly with decrease in the bluff body diameter, because the size of the recirculation bubble scales with the bluff-body diameter. A smaller recirculation zone flame becomes more easy to penetrate for the central jet flame. The limit for conversion from jet dominated flames to jet-like flames increases slightly as the bluff body diameter increases [11].

A high temperature region can be maintained at the downstream end of the recirculation bubble that is responsible for keeping the jet-dominated flames stable. Flame blow-out occurs when the recirculation zone flame itself is extinguished [11].

It is thus clear that the hot recirculation bubble provides a continual ignition source to delay the occurrence of local flame extinction at a higher jet velocity. Similar behavior also has been reported for a burner of very small $D_{\text{bluff}-\text{body}}/D_{\text{annulus}}$-ratio, however, a combusting recirculation bubble is better achieved with a larger value of $D_{\text{bluff}-\text{body}}$ [11].

According to Chen [10], an edge-flame with a well-defined propagation velocity appears to be an appropriate description of the leading-edge structures of lifted jet flames stabilized on straight tubes. On the other hand, isolated flame fronts with an arrowheaded structure, similar to triple flames, have been observed in lifted non-premixed flames on a bluff-body. Large-scale vortex shedding from the recirculation zone dominates the fuel/air mixing process in these flames and creates a cluster of fragmented flame fronts at the lifted flame base. This provides a favorable condition for development of isolated triple flames propagating in a partially premixed turbulent flow.

Bibliography

[1] T.N.G. Adriaans. Design and realisation of an updraft biomass gasification installation: WET 2004.07. Master's thesis, Eindhoven University of Technology, Eindhoven, The Netherlands, 2004.

[2] B. Albrecht. *Reactor modeling and process analysis for partial oxidation of natural gas*. PhD thesis, University of Twente, Enschede, The Netherlands, 2004.

[3] L.L. Alston. *High Voltage Technology*. Oxord University Press, Oxford, UK, 1968.

[4] C. Barckholtz, T.A. Barckholtz, and C.M. Hadad. A mechanistic study of the reactions of H, $O(^3P)$, and OH with monocyclic aromatic hydrocarbons by density functional theory. *J. Phys. Chem. A*, 105:140–152, 2001.

[5] C. Barckholtz, M.J. Fadden, and C.M. Hadad. Computational study of the mechanisms for the reaction of $O_2(^3\sum_g)$ with aromatic radicals. *J. Phys. Chem. A*, 103:8108–8117, 1999.

[6] A. Beretta, P. Forzatti, and E. Ranzi. Production of olefins via oxidative dehydrogenation of propane in autothermal conditions. *Journal of Catalysis*, 184:469–478, 1999.

[7] L.I. Berger. Dielectric strength of insulating materials. In D.R. Lide, editor, *CRC Handbook of chemistry and physics, Internet version 2006*, chapter 15, pages 42–46. Taylor and Francis, Boca Raton, Florida, 2006.

[8] J. Boulanger, L. Vervisch, J. Reveillon, and S. Ghosal. Effects of heat release in laminar diffusion flames lifted on round jets. *Combustion and Flame*, 134:355–368, 2003.

[9] C. Brage, Q. Yu, G. Chen, and K. Sjöström. Use of amino phase adsorbent for biomass tar sampling and separation. *Fuel*, 76(2):137–142, 1997.

[10] Y-C. Chen and R.W. Bilger. Stabilization mechanisms of lifted laminar flames in axisymmetric jet flows. *Combustion and Flame*, 122:377–399, 2000.

[11] Y-C. Chen, C-C. Chang, K-L. Pan, and J-T. Yang. Flame lift-off and stabilization mechanisms of nonpremixed jet flames on a bluff-body burner. *Combustion and Flame*, 115:51–65, 1998.

[12] J.P. Ciferno and J.J. Marano. Benchmarking biomass gasification technologies for fuels, chemicals and hydrogen production. Technical report, U.S. Department of Energy and the National Energy Technology Laboratory, 2002.

[13] H. Cohen, G.F.C. Rogers, and H.I.H. Saravanamuttoo. *Gas Turbine Theory*. Prentice Hall, Harlow, England, 4th edition, 1996.

[14] H.F. Coward and G.W. Jones. *Bulletin 503: Limits of flammability of gases and vapors*. U.S. Bureau of Mines, Washington, USA, 1952.

[15] R.L. Daugherty and J.B. Franzini. *Fluid Mechanics*. McGraw-Hill book company, New York, USA, 6th edition, 1965.

[16] H.C. den Dekker. De in-line oxidator. Ogo-project report, Eindhoven University of Technology, Eindhoven, The Netherlands, 2006.

[17] H.C. den Dekker. Ontwerpen en construeren van een in-line oxidator. Internship report, Eindhoven University of Technology, Eindhoven, The Netherlands, 2006.

[18] L. Devi, K.J. Ptasinski, and F.J.J.G. Janssen. A review of the primary measures for tar elimination in biomass gasification processes. *Biomass and bioenergy*, 24:125–140, 2003.

[19] M.K. Drayton, A.V. Saveliev, L.A. Kennedy, A.A. Fridman, and Y.D. Li. Syngas production using superadiabatic combustion of ultra-rich methane-air mixtures. *27th symposium (international) on combustion. Pittsburg: The Combustion Institute*, pages 1361–1367, 1998.

[20] H.A. van Essen. Design of a laboratory gas turbine installation. Technical report, Stan Ackermans Institute, Eindhoven University of Technology, Eindhoven, The Netherlands, 1995.

[21] A.V. Evlampiev. *In Press*. PhD thesis, Eindhoven University of Technology, Eindhoven, The Netherlands, 2007.

[22] A.V. Evlampiev, L.M.T. Somers, L.P.H. de Goey, and R.S.G. Baert. Flamelet modelling of heavy hydrocarbons combustion applied to diesel engine. In J. Vandooren, editor, *Proceedings of the European Combustion Meeting 2005*, Louvain-la-Neuve, Belgium, 2005.

[23] M.J. Fadden, C. Barckholtz, and C.M. Hadad. Computational study of the unimolecular decomposition of phenylperoxy radical. *J. Phys. Chem. A*, 104:3004–3011, 2000.

[24] M.J. Fadden and C.M. Hadad. Unimolecular decomposition of the 2-oxipenoxy radical: a key seven-membered ring intermediate in the thermal oxidation of benzene. *J. Phys. Chem. A*, 104:8121–8130, 2000.

[25] E. Fernández-Tarrazo, M. Vera, and A. Liñán. Liftoff and blowoff of a diffusion flame between parallel streams of fuel and air. *Combustion and Flame*, 144:261–276, 2006.

[26] C.G. Fotache, T.G. Kreutz, and C.K. Law. Ignition of hydrogen-enriched methane by heated air. *Combustion and Flame*, 110:429–440, 1997.

[27] M. Frenklach, T. Yuan, and M.K. Ramachandra. Soot formation in binary hydrocarbon mixtures. *Energy & Fuels*, 2:462–480, 1988.

[28] X.A. Garcia and K.J. Hüttinger. Steam gasification of naphthalene as a model reaction of homogeneous gas/gas reaction during coal gasification. *Fuel*, 68:1300–1310, 1989.

[29] T.M. Geerssen, editor. *Physical properties of natural gases*. N.V. Nederlandse Gasunie, Groningen, The Netherlands, 1980.

[30] R.A. Geisbrecht and T.E. Daubert. Hydrocarbon partial oxidation. *Ind. Eng. Chem., Prod. Res. Dev.*, 15(2):115–122, 1976.

[31] S. Ghosal and L. Vervisch. Stability diagram for lift-off and blowout of a round jet laminar diffusion flame. *Combustion and Flame*, 123:646–655, 2001.

[32] P. Glarborg, R.J. Kee, J.F. Grcar, and J.A. Miller. PSR: a fortran program for modeling well-stirred reactors. Technical report SAND86-8209, Sandia National Laboratories, Livermore, USA, 1986.

[33] B. Gøbel, U. Henriksen, J. Ahrenfeldt, T.K. Jensen, C. Hindsgaul, and J.B. Bentzen. Status-2000 hours of operation with the viking gasifier. In W.P.M. van Swaaij, T. Fjällström, P. Helm, and A. Grassi, editors, *Proceedings of the second world biomass conference*, volume II, pages 1284–1287. ETA-Florence and WIP-Munich, 2004.

[34] S. Granata, T. Faravelli, E. Ranzi, N. Olten, and S. Senkan. Kinetic modeling of counterflow diffusion flames of butadiene. *Combustion and Flame*, 131:273–284, 2002.

[35] J.B. Heywood. *Internal Combustion Engine Fundamentals*. McGraw-Hill book company, Singapore, 1988.

[36] T.A. van der Hoeven, H.C. de Lange, and A.A. van Steenhoven. Ex-situ removal on tar of small-scale biomass gasification by partial oxidation. In W.P.M. van Swaaij, T. Fjällström, P. Helm, and A. Grassi, editors, *Proceedings*

of the second world biomass conference, volume I, pages 821–824. ETA-Florence and WIP-Munich, 2004.

[37] T.A. van der Hoeven, H.C. de Lange, and A.A. van Steenhoven. Analysis of influence of fuel power on tar removal by partial oxidation. In L. Sjunnesson, J.E. Carrasco, P. Helm, and A. Grassi, editors, *Proceedings of the 14th European biomass conference*, pages 780–782. ETA-Florence and WIP-Munich, 2005.

[38] T.A. van der Hoeven, H.C. de Lange, and A.A. van Steenhoven. Analysis of hydrogen-influence on tar removal by partial oxidation. *Fuel*, 85:1101–1110, 2006.

[39] M.P. Houben. *Analysis of tar removal in a partial oxidation burner*. PhD thesis, Eindhoven University of Technology, Eindhoven, The Netherlands, 2004.

[40] M.P. Houben, H.C. de Lange, and A.A. van Steenhoven. Tar reduction through partial combustion of fuel gas. *Fuel*, 84:817–824, 2005.

[41] http://webbook.nist.gov/chemistry.

[42] M. Ilbas, A.P. Crayford, I. Yilmaz, P.J. Bowen, and N. Syred. Laminar-burning velocities of hydrogen-air and hydrogen-methane-air mixtures: An experimental study. *International Journal of Hydrogen Energy*, In Press, 2006.

[43] W.S. Janna. *Design of fluid thermal systems*. PWS-Kent, Boston, USA, 1993.

[44] A. Jess. Thermische und katalytische spaltung von kohlenwasserstoffen in wasserstof- und wasserdampfreicher atmosphäre: Eine modelluntersuchung zur erzeugung von reduktionsgas aus koksofenrohgas. Habilitationsschrift, Universität Karlsruhe, Karlsruhe, Germany, 1996.

[45] M. Kaltschmitt and H. Hartmann. *Energie aus biomasse, grundlagen, techniken und verfahren*. Springer-Verlag, Berlin, 2001.

[46] G.A. Karim and A.S. Hanafi. An analytical examination of the partial oxidation of rich mixtures of methane and oxygen. *Fossil Fuel Combustion ASME, PD*, 33:127–133, 1991.

[47] A. Kazakov and M. Frenklach. DRM-19: Reduced reaction sets based on GRI-Mech 1.2. www.me.berkeley.edu/drm/.

[48] A.A. Konnov. Non-catalytic partial oxidation of methane over a wide temperature range. In *Proceedings of the European combustion meeting*, Orléans, France, 2003.

[49] A.H. Lefebvre. *Gas turbine combustion*. McGraw-Hill book company, London, UK, 1983.

[50] A.H. Lefebvre and E.R. Noster. The design of tubular gas turbine combustion chamber. In *Technical advances in gas turbine design: A symposium arranged by the Combustion Engines Group*, Univerity of Warwick, Conventry, UK, 1969.

[51] X. Liu, W. Li, H. Xu, and Y. Chen. A comparative study of non-oxidative pyrolysis and oxidative cracking of cyclohexane to light alkenes. *Fuel Processing Technology*, 86:151–167, 2004.

[52] X. Liu, W. Li, H. Xu, and Y. Chen. Production of light alkenes with low CO_2 emission from gas phase oxidative cracking (GOC) of hexane. *React. Kinet. Catal. Lett.*, 81(2):203–209, 2004.

[53] A.E. Lutz, F.M. Rupley, R.J. Kee, and W.C. Reynolds. Equil: A chemkin implementation of stanjan, for computing chemical equilibria. Technical Report CA 94551, Sandia National Laboratories, Livermore, USA, 1998.

[54] N.M. Marinov, W.J. Pitz, C.K. Westbrook, A.M. Vincitore, M.J. Castaldi, S.M. Senkan, and C.F. Melius. Aromatic and polycyclic aromatic hydrocarbon formation in a laminar premixed n-butane flame. *Combustion and Flame*, 114:192–213, 1998.

[55] C.S. McEnally, L.D. Pfefferle, B. Atakan, and K. Kohse-Höinghaus. Studies of aromatic hydrocarbon formation mechanisms in flames: Progress towards closing the fuel gap. *Progress in Energy and Combustion Science*, 32:247–294, 2006.

[56] A.D. McNaught and A. Wilkinson. *IUPAC Compendium of Chemical Terminology, online version*. Blackwell Science, 2nd edition, 1997.

[57] B.E. Milton and J.C. Keck. Laminar burning velocities in stoichiometric hydrogen and hydrogen-hydrocarbon gas mixtures. *Combustion and Flame*, 58:13–22, 1984.

[58] K. Miura, M. Kawase, H. Nakagawa, R. Ashida, T. Nakai, and T. Ishikawa. Conversion of tar in hot coke oven gas by pyrolysis and steam reforming. *Journal of Chemical Engineering of Japan*, 36(7):735–741, 2003.

[59] P.O. Morf. *Secondary reactions of tar during thermochemical biomass conversion*. PhD thesis, Swiss Federal Institute of Technology Zurich, Zurich, Switzerland, 2001.

[60] L.K. Mudge and C.A. Rorhmann. *Gasification of solid waste fuels in a fixed-bed gasifier*. Washington, USA, 1978.

[61] H.S. Mukunda. *Technologies for biomass utilisation*. Solar Agni Systems, Pondicherry, France, 1999.

[62] R. Mungen and M.B. Kratzer. Partial combustion of methane with oxygen. *Industrial and Engineering Chemistry*, 43(12):2782–2787, 1951.

[63] J.P.A. Neeft. Teren uit pyrolyse en vergassing van biomassa en reststromen. Report ECN-C–99-102, ECN-Biomassa, Petten, The Netherlands, 1999.

[64] J.P.A. Neeft, H.A.M. Knoef, and P. Onaji. Behaviour of tar in biomass gasification systems. Technical report, BTG and ECN, 1999.

[65] J.A. van Oijen. *Flamelet-Generated Manifolds: Development and application to premixed laminar flames*. PhD thesis, Eindhoven University of Technology, Eindhoven, The Netherlands, 2002.

[66] T. Plessing, P. Terhoeven, N. Peters, and M.S. Mansour. An experimental and numerical study of a laminar triple flame. *Combustion and Flame*, 115:335–353, 1998.

[67] K. Prasad and E.W. Price. A numerical study of the leading edge of laminar diffusion flames. *Combustion and Flame*, 90:155–173, 1992.

[68] Y.P. Raizer. *Gas Discharge Physics*. Springer, Berlin, Germany, 1991.

[69] E. Ranzi, M. Dente, A. Goldaniga, G. Bozzano, and T. Faravelli. Lumping procedures in detailed kinetic modeling of gasification, pyrolysis, partial oxidation and combustion of hydrocarbon mixtures. *Progress in Energy and Combustion Science*, 27:99–139, 2001.

[70] E. Ranzi, T. Faravelli, A. Goldaniga, F. Ferrari, and M. Lattuada. Pyrolysis and oxidation of unsaturated C_2 and C_3 species. *Experimental Thermal and Fluid Science*, 21:71–78, 2000.

[71] T.B. Reed and A. Das. Handbook of biomass downdraft gasifier engine systems. Technical Report Second Printing of SERI/SP-271-3022; DE 88001135, UC Category: 245, The Biomass Energy Foundation Press, Golden, Colorado, U.S.A.

[72] H. Richter, S. Granata, W.H. Green, and J.B. Howard. Detailed modeling of PAH and soot formation in a laminar premixed benzene/oxygen/argon low-pressure flame. *Proceedings of the Combustion Institute*, 30:1397–1405, 2005.

[73] C.R. Shaddix. *An experimental study of the high temperature oxidation of 1-methylnaphthalene*. PhD thesis, Princeton University, Princeton, New Jersey, USA, 1993.

[74] C.R. Shaddix, K. Brezinsky, and I. Glassman. Analysis of fuel decay routes in the high-temperature oxidation of 1-methylnaphthalene. *Combustion and Flame*, 108:139–157, 1997.

[75] M.S. Skjøth-Rasmussen, P. Glarborg, M. Østberg, J.T. Johannessen, H. Livbjerg, A.D. Jensen, and T.S. Christensen. Formation of polycyclic aromatic hydrocarbons and soot in fuel-rich oxdiation of methane in a laminar flow reactor. *Combustion and Flame*, 136:91–128, 2004.

[76] G.P. Smith, D.M. Golden, M. Frenklach, N.W. Moriarty, B. Eiteneer, M. Goldenberg, et al. GRI-Mech 3.0. Technical report, Gas Research Institute, Chicago, Ilinois, USA.

[77] L.M.T. Somers. *The simulation of flat flames with detailed and reduced chemical models*. PhD thesis, Eindhoven University of Technology, Eindhoven, The Netherlands, 1994.

[78] H. Susanto. *Moving bed gasifier with internal recycle and separate combustion of pyrolysis gas*. PhD thesis, Institut Teknologi Bandung, Indonesia, 1984.

[79] G. Tarales, M.G. Kontominas, and X. Kakatsios. Modeling the thermal destruction of toluene (C_7H_8) as tar-related species for fuel gas cleanup. *Energy & Fuels*, 17:329–337, 2003.

[80] S.J.M. Verhagen. Ontwerp en bouw van de gasturbine-proefopstelling: WOC-WET 94.035. Master's thesis, Eindhoven University of Technology, Eindhoven, The Netherlands, 1994.

[81] A. Violi, A. D'Anna, and A. D'Alessio. Modeling of particulate formation in combustion and pyrolysis. *Chemical Engineering Science*, 54:3433–3442, 1999.

[82] www.gaseq.co.uk.

[83] M.G. Zabetakis. *Bulletin 627: Flammability charactersitics of combustible gases and vapors*. U.S. Bureau of Mines, Washington, USA, 1965.

[84] J.N. Zhu. *A feasibility study of methane reforming by partial oxidation*. PhD thesis, Curtin University of Technology, Australia, 2001.

Dankwoord

Klaar! Voor mij breekt er nu een nieuwe fase aan in mijn leven, maar daar wil ik niet aan beginnen zonder eerst een aantal mensen te bedanken voor hun samenwerking, hulp, advisering, of persoonlijke omgang tijdens mijn promotie-traject.

Ten eerste ben ik mijn 1ste promotor professor Anton van Steenhoven en copromotor Rick de Lange zeer erkentelijk voor hun begeleiding. Rick wist met zijn theoretisch en praktisch inzicht keer op keer richting te geven aan mijn onderzoek. Met zijn relativeringsvermogen en humor wist hij de verschillende tegenslagen in het onderzoek altijd weer positief te benaderen. Verder heb ik ook veel van hem geleerd over analyse van problemen, ontwerpen van apparaten, en het begeleiden van afstudeerders en stagiairs. Anton's overzicht en continue drang naar wetenschappelijke resultaten hebben tot interessante onderzoekspaden geleid. Vooral zijn inzicht dat de beste weg van A naar B niet altijd een rechte lijn is, was nodig om tot resultaten te komen.

Ten tweede ben ik zeer dankbaar voor de vele hulp die ik kreeg van verschillende collega's. Ik denk hierbij aan o.a. mijn 2de promotor professor Philip de Goey, Jeroen van Oijen, Bart Soomers, en Alexei Evlampiev die mij hielpen bij het opzetten van modellen m.b.t. partiële verbrandings processen. Verder denk ik aan alle medewerkers uit de werkplaats en het lab met hun uitstekende werk en goede adviezen. In het bijzonder wil ik Ties de Grouw bedanken voor zijn inzet om gedurende twee jaar al het reilen en zeilen rond het biomassa-lab in orde te krijgen.

Ten derde zou mijn werk nooit zover zijn gekomen zonder hulp van buitenaf. Mensen die mij hebben geholpen zijn o.a. de medewerkers van de GTD-electro, die mij zeer kundig hielpen bij alle elektronische aspecten van de proefopstelling. Zonder hun snelle hulp en inzicht zou de mate van professionaliteit in de proefopstelling niet zo hoog geworden zijn. Maar vooral de prettige en vlotte samenwerking sprak mij bijzonder aan. Verder is daar Peter Lipman van de faculteit Scheikundige Technologie, die mij veelvuldig geholpen heeft problemen m.b.t. de gas-chromatograaf te analyseren. Dankzij hem verkreeg ik in korte tijd de kennis die nodig is om zelf betrouwbare analyses uit te kunnen voeren.

Last, but not least, wil ik een aantal mensen bedanken voor hun gezelschap. Hieronder natuurlijk mijn kamergenotes Svetlana Ljevar en Silvia Nedea, en alle collega's met wie ik serieuze gesprekken en slappe klets mocht delen. Maar in het bijzonder wil ik Frank, Geert-Jan, Gratje, en Linda bedanken voor hun luisterend oor en adviezen bij persoonlijke vraagstukken!

Verder rest mij natuurlijk het thuisfront te bedanken bij wie ik altijd terecht kan/kon voor plezier en raad. Dit zijn onder andere mijn ouders, mijn broer en zus, Kim, en alle vrienden.

Dorus van der Hoeven

Résumé

Theodoor Adriaan (Dorus) van der Hoeven was born in Eersel, The Netherlands, on the 22nd of July 1978. In his third year of life he moved together with his parents to Schijndel, The Netherlands, where he has lived ever since. From 1990 to 1997 he followed secondary education (atheneum) at the Elde College in Schijndel. From 1997 to 2002 he studied Mechanical Engineering at the Eindhoven University of Technology. He specialized in the field of process technology. As part of his studies he did an internship within the Materials & Process Engineering Department of The University of Waikato, Hamilton (New Zealand) from April 2001 to August 2001. The internship concerned an experimental study on the flow and separation behaviour of mini hydrocyclones for the separation of starch and gluten in the food industry.

Dorus performed his graduation project in the Process Technology Group of prof.dr.ir. J.J.H. Brouwers at the Department of Mechanical Engineering at the Eindhoven University of Technology. The graduation project involved the study and testing of an aerosol generator for monodisperse 10 μm particles, necessary for the study of fouling of heat exchangers. He obtained his Master of Science degree in August 2002, exactly five years after starting his study.

In October 2002, Dorus started his research towards a Ph.D. in the Energy Technology Group of prof.dr.ir. A.A. van Steenhoven, again at the Mechanical Engineering department of the Eindhoven University of Technology. The Ph.D. project was financially supported by SenterNovem, and concerned the study of tar reduction from product gas by partial combustion, in order to solve the tar problem generated during biomass gasification. This thesis is a result of the project.